Spring 2020

Multi-Scale Modeling for Transport Study Inside Porous Layers of Polymer Electrolyte Membrane Fuel Cell Using Direct Numerical Simulation

Pongsarun Satjaritanun

MULTI-SCALE MODELING FOR TRANSPORT STUDY INSIDE POROUS LAYERS OF POLYMER ELECTROLYTE MEMBRANE FUEL CELL USING DIRECT NUMERICAL SIMULATION

by

Pongsarun Satjaritanun

Bachelor of Engineering
Chiang Mai University, 2012

Master of Engineering
Chiang Mai University, 2015

Submitted in Partial Fulfillment of the Requirements

For the Degree of Doctor of Philosophy in

Chemical Engineering

College of Engineering and Computing

University of South Carolina

2020

Accepted by:

Sirivatch Shimpalee, Major Professor

John R. Regalbuto, Co-Major Professor

John W. Weidner, Committee Member

Melissa A. Moss, Committee Member

Iryna V. Zenyuk, Committee Member

Cheryl L. Addy, Vice Provost and Dean of the Graduate School

ACKNOWLEDGEMENTS

I express appreciation to my Ph.D. advisor, Professor Sirivatch Shimpalee, Department of Chemical Engineering, University of South Carolina, for his patience, motivation, supervision, guidance, invaluable suggestions, and supporting me during these past four years. I could not have imagined having a better advisor and mentor for my Ph.D. study.

Besides my advisor, I appreciate the support and collaboration provided throughout my Ph.D. career by my mentors Professor John W. Weidner of the University of Cincinnati, Professor John R. Regalbuto of the University of South Carolina, Professor Iryna V. Zenyuk of the University of California Irvine, Professor Yottana Khunatorn of Chiang Mai University, Thailand, and Mr. Shinichi Hirano of Ford Motor Company, for their insightful comments and encouragement, but also for the hard questions which incented me to widen my research from various perspectives.

I thank my fellow lab mates for the stimulating discussions, working together, and for all the fun we have had in the last four years. Also, I thank my friends and staff in the Department of Chemical Engineering, University of South Carolina.

I would like to gratefully acknowledge Ford Motor Company, Perfect Mixing LLC, Greenway Energy LLC, and Department of Energy for providing financial support.

I would like to thank my father, Sin, mother, Kannaphak, and younger brother Pattarapong, for warm support in everything on my Ph.D. study. I also thank my fiancée, Monchupa Kingsak, for her patience and loving support.

ABSTRACT

The direct modeling-based Lattice Boltzmann Agglomeration Method (LBAM) is used to explore the electrochemical kinetics and multi-scalar/multi-physics transport inside the detailed structure of the porous and catalyst layers inside polymer electrolyte membrane fuel cells (PEMFCs). The complete structure of the samples is obtained by both micro- and nano- X-ray computed tomography (CT). LBAM is able to predict the electrochemical kinetics in the nanoscale catalyst layer and investigate the electrochemical variables during cell operation. This work shows success in integrating the lattice elements into an agglomerate structure in the catalyst layer (CL). The predictions using LBAM were compared and validated with a macro-kinetics model, ex-situ, and in-situ flow visualization. The studies include prediction of water evolution, water saturation, breakthrough pressure, heat transfer, species transport, and electrochemical kinetics inside the porous and catalyst layers under different conditions that can occur in fuel cells. The overall predictions reveal that the local saturation of liquid water, distributions of electrochemical variables, and mass fraction across the samples can be controlled by the regulation of operating conditions, especially under conditions that cause transport losses. LBAM is a highly effective method of predicting the partial flooding issue, understanding the transport resistance, and investigating transport inside the porous transport layer that affects the overall cell performance in the PEMFC.

The complex detailed structure of porous and catalyst layers is in the micro- and nano- scale, conventional computational fluid dynamics modeling is not suitable for modeling multi-physics transport due to the limitation of the mesh generation method and more computational time by the discrete approximation of partial differential equations. This work shows the enhancement of direct modeling-based LBAM approach, which incorporates the detailed structure of porous layers from X-ray CT. The Boltzmann transport equation is already in discrete form, which means that the LBAM is clever numerical, parallel, and fast calculator per cell timestep. LBAM can predict and show distributions of electrochemical variables on the detailed structure of the CL, which is beneficial to the fuel cell design community. This method can expedite the development of porous components in PEMFCs in a cost-effective manner. The LBAM simulation can assist the optimization of porous structure design and durability as well as improvement of water management, particularly in the catalyst layer. The LBAM shows ability to model other electrochemical systems as well, especially those with complex micro or nanostructures such as other fuel cells, batteries, or electrolyzers.

TABLE OF CONTENTS

LIST OF TABLES

LIST OF FIGURES

LIST OF SYMBOLS

a_{agg} Effective agglomerate surface area

a_{Pt} Active surface area of platinum

a_{Pt}^{eff} Effective reaction surface area

b Probability distribution functions

c_s Speed of sound in Lattice scale

$C_{H_2}^{ref}$ Reference hydrogen concentration

$C_{O_2}^{ref}$ Reference oxygen concentration

D_{eff} Effective diffusivity of dissolved reactant in Nafion™

$D_{\emptyset}^{eff}$ Effective diffusion coefficient of proton conductivity

D_{H_2} Diffusivity of the dissolved hydrogen in Nafion™

D_{O_2} Diffusivity of the dissolved oxygen in Nafion™

E_{act} Activation energy

E_r Effectiveness factor of the spherical agglomerate

f_j Particle distribution function in the j direction

F Faraday's constant

$\vec{g}$ Gravity

H Henry's constant

i Current per unit volume in the CL

i_{agg} Agglomerate volumetric current density

$i_{o,a}$ Anode exchange current density

$i_{o,c}$ Cathode exchange current density

$i_{o,a}^{ref}$ Reference anode exchange density

$i_{o,c}^{ref}$ Reference cathode exchange density

k_a Reaction rate at the surface of the agglomerate core of anode

k_c Reaction rate at the surface of the agglomerate core of cathode

m_{Pt} Platinum loading

M_{jl} Transformation matrix to macroscopic moment

$\vec{n}$ Unit normal vector at control volume surface

n Number of electrons

P Macroscopic fluid pressures

P_{H_2} Hydrogen pressure

P_{O_2} Oxygen pressure

$P_{H_2}^{ref}$ Reference hydrogen pressure

$P_{O_2}^{ref}$ Reference oxygen pressure

R Ideal gas constant

r_{agg} Agglomerate radius

$\hat{S}_{jl}$ Diagonal relaxation matrix

t Discrete times

t_{CL} Catalyst layer thickness

t_D Dimensionless time

Δt Constant time step

T Local temperature

T_0 Refence temperature

$\vec{u}$ Macroscopic fluid velocity

V Total volume that agglomerate and thin film occupy

V_{agg} Agglomerate volume

$\vec{V}$ Fluid velocity

$\vec{x}$ Lattice node

GREEK SYMBOLS

α_a Anode charge transfer coefficient

α_c Cathode charge transfer coefficient

δ Thickness of the Nafion™ film

ε_{CL} Catalyst layer porosity

η_a Anode overpotential

η_c Cathode overpotential

τ Relaxation parameter

$\emptyset_L$ Thiele's modulus

$\emptyset_m$ Electrolyte potential

ρ_{Pt} Platinum density

μ Molecular viscosity of the fluid

μ_j Raw of the moment

ν Macroscopic kinematic viscosity

Ω_j Collision operator

Ω_j^{MRT} Multiple relaxation time collision operator

LIST OF ABBREVIATIONS

1D ..... 1 Dimensional

2D ..... 2 Dimensional

3D ..... 3 Dimensional

ALS ..... Advanced Light Source

BGK ..... Bhatnagar-Gross-Krook

CFD ..... Computational Fluid Dynamics

CL ..... Catalyst Layer

CT ..... Computed Tomography

GDL ..... Gas Diffusion Layer

HOR ..... Hydrogen Oxidation Reaction

LBAM ..... Lattice Boltzmann Agglomeration Method

LBGK ..... Lattice Bhatnagar-Gross-Krook

LBM ..... Lattice Boltzmann Method

LBNL ..... Lawrence Berkeley National Laboratory

LGCA ..... Lattice Gas Cellular Automata

MEA ..... Membrane Electrode Assembly

MPL ..... Micro Porous Layer

MRT ..... Multiple Relaxation Time

N-S ..... Navier-Stokes

OCV ..... Open Circuit Voltage

ORR ..... Oxygen Reduction Reaction

PDE ..... Partial Differential Equation

PDF..... Probability Density Function

PEMFC ..... Polymer Eelectrolyte Membrane Fuel Cell

PTFE.....Polytetrafluoroethylene

Q-Q..... Quantile-Quantile

SEM..... Scanning Electron Microscope

SRT..... Single Relaxation Time

CHAPTER 1

INTRODUCTION

1.1 BASIC OPERATION PRINCIPLE OF POLYMER ELECTROLYTE MEMBRANE FUEL CELLS

Polymer electrolyte fuel cells are electrochemical devices that efficiently convert chemical energy of the fuel directly into electrical energy. The general concept of fuel cell operation is characterized as gas-mixture transport and transformation of species by electrochemical reactions. The electrochemical reactions in fuel cells happen simultaneously on both sides of the membrane, as shown in Fig. 1.1. The hydrogen from anode flow channel is transported through the gas diffusion layer toward the Membrane Electrode Assembly (MEA) surface. Hydrogen molecules are dissociated to protons and electrons in the catalyst layer. The anode reaction equation was derived considering the partial electrode reaction of hydrogen oxidation as:

$$H_2 \rightarrow 2H^+ + 2e^- \tag{1.1}$$

The water that impregnates the MEA hydrates the protons. Electro-osmosis and diffusion transport the water in the MEA. The air mixture in cathode channel is transported through the diffusion layer toward the MEA where oxygen reacts with protons as:

$$\frac{1}{2}O_2 + 2H^+ + 2e^- \rightarrow H_2O \tag{1.2}$$

The overall reaction is:

$$H_2 + \frac{1}{2}O_2 \rightarrow H_2O \tag{1.3}$$

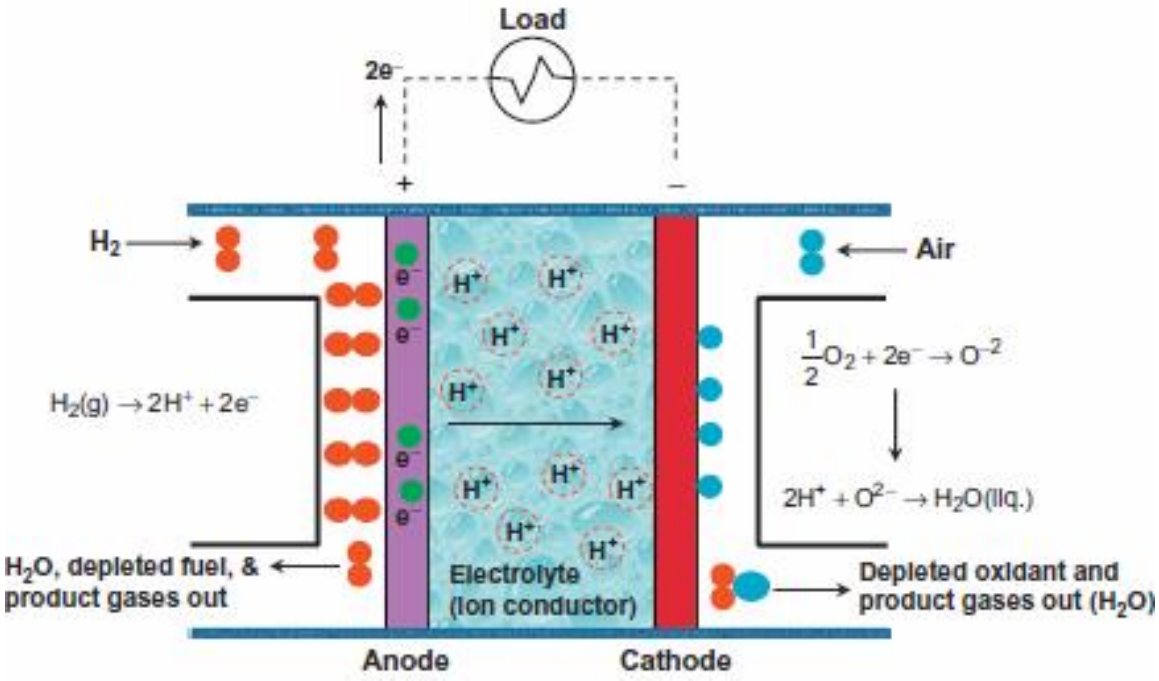

Figure 1.1 Schematic of the hydrogen/oxygen fuel cell (Popov 2015).

1.2 PRELIMINARY

The enhancement of the mass transports and kinetics in porous layers of polymer electrolyte membrane fuel cells (PEMFCs) is essential for developing materials and designing systems to improve the PEMFC performance and durability. The catalyst layer (CL) should be tailored to facilitate the hydrogen oxidation reaction (HOR) and oxygen reduction reaction (ORR). Increasing the area-specific power density is one of the most effective ways to reduce the PEMFC cost, followed by reduction of platinum (Pt) loading in the fuel cell stack. It is imperative to consider, the fuel cell performance must be improved at the high current densities where the mass-transport overpotential is dominant. The oxygen transport resistance is a large fraction of the mass-transport overpotential at the cathode. Condensed water in the flow field, and porous layers reduce oxygen transport to the ORR region. Experimental investigations of locally saturated porous media in the operating cell is difficult. The Computational Fluid Dynamics (CFD) is a mathematical modeling tool, which can be considered the incorporation of theory and experimentation in the field of kinetics, heat, and mass transport for PEMFC. This dissertation proposes the development of direct-modeling-based within the detailed structure of the porous media to understand the kinetics and multi-scalar/multi-physics transports. In fuel cells, the porous media consist of gas diffusion layer (GDL), micro porous layer (MPL), and Catalyst layer (CL).

Figure 1.2 shows the LBAM concept with the detailed structure of GDL/MPL sample (SGL 25BC) and CL sample (Ion Power). The model geometries of porous and catalyst layers provided in this study will be obtained by a 3D, reconstructed microstructure from both micro- and nano- X-ray computed tomography (CT).

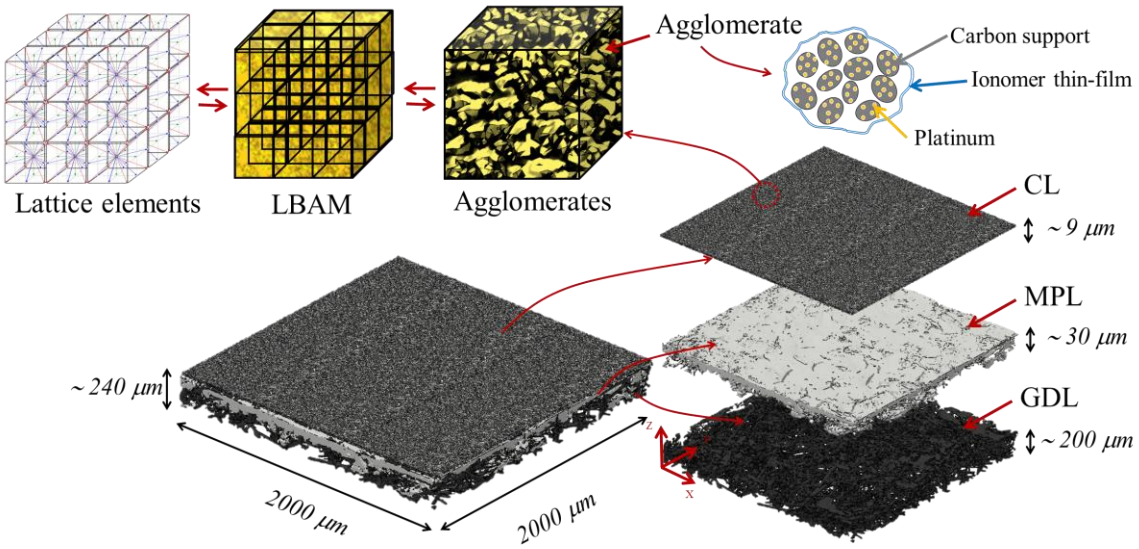

Figure 1.2 LBAM concept with the detailed structure of GDL/MPL sample (SGL 25BC) and CL sample (Ion Power).

The complex detailed structure of the porous layers and the catalyst layer model is in the micro- and nano-scale, conventional CFD based fuel cell model is not suitable for modeling mass transport due to the limitation of the mesh generation method and more computational time by the discrete approximation of partial differential equation (PDE). The Boltzmann transport equation is already in discrete form, which means that the LBM is clever numerical, parallel, and fast calculator per cell timestep. The CFD simulation with the Lattice Boltzmann Method (LBM), particles-based approach, will be used to solve the heat and mass transport in the porous and catalyst layers. The combination of LBM and Agglomerate model, Lattice Boltzmann Agglomeration Method (LBAM), is used to simulate the electrochemical kinetics in the CL. The lattice elements are determined as an agglomerate of carbon support (Cs), Platinum (Pt), and Ionomer, as shown in Fig. 1.2. Through this method, the agglomerates in the CL are able to apply the kinetic expression and solve the electrochemical variables such as overpotential and current density.

This dissertation will show the enhancement of direct-modeling-based LBAM approach, which incorporates the detailed structure of porous and catalyst layers from both micro- and nano- X-ray CT. This approach consists of the kinetic model in the catalyst layer, which will involve coupling electrochemical kinetic to investigate the electrical potentials, electrical current, electron transfer, and exchange current in the catalyst layers. The solutions will be used for the optimization of catalyst layer thickness, durability, and water management improvement, for novel porous materials, particularly in the catalyst layer. Moreover, the predictions from CFD simulations can help to optimize the design of porous layer structures and other components, such as flow fields; thereby improving the PEMFC's overall performance, cost of production, and development time.

1.3 PREVIOUS WORKS AND COMMUNICATION STATEMENTS

Improvement of the kinetics and mass transport in PEMFCs is essential for their wide-spread commercialization (Wang 2004; Kandlikar 2008; Berg et al. 2004); it is a critical subject that has been greatly studied due to its importance in PEMFC performance at high current densities (Weber and Newman 2006; Weber et al. 2014; Ayers et al. 2016; Wang et al. 2006). To achieve maximum removal of liquid-water and increase the area-specific power density, it is important to optimize the porous layers, specifically in the catalyst layer. GDLs for PEMFCs are porous layers between the catalyst layer and the gas flow field, which allow for the transport of product water and heat from the catalyst layer, as well as the transport of reactant gases to the catalyst layer. The GDL is composed of carbon-fiber-based cloths and paper. The hydrophobic characteristics of the GDL can accelerate the removal of liquid-water during PEMFC operation (Ji and Wei 2009). In general, the GDL carbon fiber's wettability depends on a degree of graphitization during pyrolysis process (Bruno and Viva 2014). To create hydrophobicity, GDLs are usually treated with a 5–20 wt% loading of a non-wetting polymer such as polytetrafluoroethylene (PTFE). However, the non-uniformities in the coating and drying process cause the overall structure to have mixed wettability (Kumbur and Mench 2009; Gostick et al. 2010). In addition, a thin MPL, consisting of carbon powder and polymer binders, is used on the GDL side facing the catalyst layer in the membrane electrode assembly (MEA) to further increase cell performance and mechanical stability. The complex structure and chemical heterogeneity of the GDL, MPL, and CL make studying the transport of liquid water and obtaining a solution for mass transport losses substantially more complicated. Furthermore,

enhancing the catalyst kinetics and mass transport activity for ORR is another imperative action to achieve the improvement performance and durability (Kandlikar et al. 2014).

Many researchers have studied the transport of liquid water through the GDL and MPL in order to develop an understanding of the resistance of reactant gas transport due to water accumulation. These included the observation of vapor condensation and liquid breakthrough in a GDL using an environmental scanning electron microscope (SEM) (Nam and Kaviany 2003; Nam et al. 2009). They proposed a treelike transport mechanism in which micro-droplets condensed from vapor agglomerate to form macro-droplets which eventually flow preferentially toward larger pores and breakthrough. Pasaogullari and Wang (2004) also assumed a tree-like water transport behavior in GDLs in their two-phase flow model. Bazylak et al. (2008) observed the dynamic changes in water breakthrough locations and they described that phenomena using a dynamic and interconnected network of water pathways within the GDL. Manke et al. (2007, 2008) and Hartnig et al. (2008) investigated liquid water evolution and transport during fuel cell operation with synchrotron X-ray radiography. They observed an "eruptive transport" mechanism in GDL pores near the channels, which they describe as the quick ejection of droplets from the GDL into the gas channels. Both *ex-situ* and *in-situ* experiments have demonstrated the existence of low resistance water transport channels within a GDL and that water transport and breakthrough are dynamic processes. However, the morphology of transport channels and the dynamics of water transport in these channels need to be further investigated. Lu et al. (2010) reported the liquid water breakthrough across GDLs with and without a MPL. Their *ex-situ* experimental setup closely simulated a real fuel cell configuration and operating conditions. Their results reveal that recurrent breakthroughs indicate the presence

of an intermittent water drainage mechanism in the GDL. They also concluded that the MPL not only limits the number of water entry locations into the GDL but also stabilizes the water paths. Shimpalee et al. (2016) investigated several custom GDLs with two layers of MPL under different fuel cell operating conditions. The two micro layers had different properties and particle size. The pore morphology of those samples including pore size distributions and transport properties such as MacMullin numbers were reported and correlated with their performance data.

Recently, high resolution X-ray computed tomography (CT) was used to generate three-dimensional volume rendering of fuel cell materials. The technique has become a powerful tool to describe morphology and study transport properties inside complex structures like GDLs, MPLs, and catalyst layers. For example, Epting and Litster (2016) used micro X-ray CT to characterize the morphology of the GDL and provide detail analysis of the local oxygen concentration inside the GDL. Hong et al. (2016) combined nanoscale X-ray CT with the data from electrochemical diagnostics to enhance the understanding of materials and electrode designs for fuel cell particular under reversal tolerance anode. Zenyuk et al. (2016) reported liquid water evaporation rates in different types of GDL. The evaporation rates were measured using *in-situ* set-up at synchrotron micro X-ray CT. They also used a simplified 3D mathematical model with liquid water evaporation studies from X-ray CT to determine the transport limitation from water evaporation. This team also used the micro CT to understand the structural properties of GDL under different compression pressure (Zenyuk et al. 2016). Holzer et al. (2017) applied their quantitative relationship to describe the effective properties including gas diffusivity, permeability, and electrical conductivity for a dry GDL. They used

microstructure from 3D X-ray CT to characterize phase volume fractions, geodesic tortuosity, constrictivity and hydraulic radius at different compression levels. The micro-macro-relationships were then established and reported for the in-plane and through-plane directions. Those images also confirm that all pore space inside GDLs is not spherical shape and therefore using only Young-Laplace equation to analyze the water breakthrough pressure and its phenomena will not be sufficient.

Several studies have experimentally investigated liquid-water transport inside the GDLs. These included the measurements of local liquid-water saturation and liquid-water distribution in the GDL under different operating conditions using an *in-situ* experimental setup and X-ray CT, where 3-D images visualized the liquid-water distribution in the GDLs. This technique has become an important tool in characterizing morphology and studying transport properties within the GDL pores. For example, Zenyuk et al. (2016) used micro X-ray CT to investigate GDL geometry and provide a detailed analysis of the effect of land and channel area on the spatial liquid-water distribution under different levels of compression. Similarly, Shum et al. (2017) used synchrotron-based micro X-ray CT to visualize and quantify the water distribution within a GDL subject to a thermal gradient. They plotted liquid-water saturation as a function of through-plane distance to quantitatively show the water redistribution. Eller et al. (2017) investigated the liquid-water saturation and liquid permeability within a GDL, which was treated with a microporous layer (MPL), under different cell operating conditions. They also used X-ray CT to understand the structural properties of GDLs and depict the transport of liquid-water under defined conditions. Shearing et al. (Shearing et al. 2009, 2010, 2010, and 2011) characterized 3-D microstructural evolution processes of electrodes associated with

heating and operation in-situ by using the nano X-ray CT. They concluded that the detailed microstructure derived from this technique can also be used as the geometry for an electrochemical or a numerical simulation. The X-ray CT capabilities are also being used in combination with CFD simulations related to transport in porous media (Raeini et al. 2014 and 2015; Zaretskiy et al. 2010). Although liquid-water transport within GDLs has been studied extensively with experiments, an expedient method for this investigation is still necessary to avoid the cost and time requirement associated with the complexity of experimental methods. Due to the difficulty of experimental investigation during the operation, the numerical modeling approaches become favorable. The results from modeling that rely on experimental data can also determine the correct parameter functionalities, such as contact angle or capillary pressure.

There are several computational fluid dynamics (CFD) techniques that can be used to enhance our understanding of water management and transport inside the porous structure of PEMFCs. CFD is a tool that uses well-established theories to model systems whose geometries render them tedious to solve by hand. Conventional CFD with Navier-Stokes (N-S) equations is commonly used for relatively simple problems, but is inappropriate for modeling the detailed structure of a nonhomogeneous porous medium due to its complexity. So, only simple pore structures or homogeneous porous media have been simulated with the volume average approach. The Lattice Boltzmann Method (LBM) has become an important technique for solving water-transport problems, especially within the complex components of the PEMFC that are difficult to observe directly, such as the gas diffusion layer (GDL) and CL. Several researchers used LBM to simulate the mass transport inside porous layers of PEMFCs, where few works have clarified the mechanism

of water transport through the porous transport layer. Yablecki et al. (2012) studied the effect of residual water on the through-plane and in-plane thermal conductivities by using a two-phase conjugate fluid-solid thermal LBM model. They concluded that the LBM model can handle complex geometry computations and has made it possible to numerically study the effect of liquid water saturation on the predicted values of the thermal conductivities for GDL samples. Garcia-Salaberri et al. (2015 and 2015) also used LBM with the geometries from X-ray CT to study the effective diffusivities of GDLs in dry and water-invaded conditions, which includes the study of capillary pressure and saturation distribution. They also recommended that the quantitative and qualitative discrepancies between simulated and real liquid-water profiles observed in X-ray CT studies are quite substantial. Few researchers used LBM to simulate electrochemical kinetics and mass transport inside porous layers. Zhang et al. (2018) simulated the liquid water transport and oxygen diffusion in the cathode of a PEMFC with an electrochemical reaction model. However, their GDL and CL geometries were not replicas of real samples.

Direct modeling-based technique were used to understand the liquid water transport inside the real detailed structure of a porous transport layer. These detailed structures were from X-ray CT. Cetinbas et al. (2019) used direct pore-scale simulations to simulate the water transport inside the gas diffusion layer (GDL) and micro porous layer (MPL) structure. They focused on reproducing experimental data of the local transport of liquid water using a model. However, the important mechanisms for water transport such as liquid water condensation/evaporation and electrochemical kinetics were not included in their work. Liu et al. (2019) used a 1D up-scaling method to study the impact of reaction on the effective multi-scale properties in the detailed structure CL of PEMFC. Their work used a

small piece of the CL and scale-up to evaluate the diffusivity and catalyst utilization, which may not cover the change of electrochemical kinetics in the CL. Satjaritanun et al. (2017, 2017, and 2018) used the direct simulation-based LBM to model the liquid water transport in the GDL and MPL. The overall predictions show good agreement when compared with the ex-situ and in-situ experimental data. However, the detailed structure of the CL needs to be included in the simulation for studying the electrochemical kinetics and local heat and mass transport in the PEMFC.

Co-simulation approach is the emerging enabling technique that incorporates of coupled simulation techniques with the sharing of findings data to solve or model of its parts. This approach has become a useful method to predict the transport and electrochemical behavior inside the PEMFC. Shimpalee et al. (2019) demonstrated the multi-scale modeling of PEMFCs using the co-simulation technique to predict and understand the overall transport inside the detailed structure of PEMFC. Their co-simulation approach consists of macro-scale model and micro-scale LBM. The numerical results were compared to the experimental data with a good agreement. However, their detailed structure did not include the CL (the CL was treated as a homogeneous porous medium), which is important in the prediction of overall cell performance and the electrochemical kinetics of the fuel cell.

1.4 OBJECTIVES OF DISSERTATION

In this dissertation, direct modeling-based Lattice Boltzmann Agglomeration Method (LBAM) are developed to understand the electrochemical kinetics and multi-scalar/multi-physics transport inside the detailed structure of the porous and catalyst layers inside PEMFCs. The multi-scale modeling performed in this work used co-simulation

approach (Shimpalee et al. 2019) to combine both macro-scale model, micro-scale model, and nano-scale model. This means these three models need to be simultaneously solved within the same server domain and they shared and interchanged solutions between these three models at the interfacial boundary surfaces. The model geometries of porous and CL provided in this study will be obtained by a 3D, reconstructed microstructure from both micro- and nano- X-ray computed tomography (CT), as shown in Fig. 1.2. The predictions from LBAM are compared and validated with a macro-kinetics model, *ex-situ*, and *in-situ* flow visualization. The studies in this dissertation will include a prediction and explanation of water evolution, water saturation, heat transfer, species transport, and electrochemical kinetics inside porous and catalyst layers used in PEMFC.

Lattice Boltzmann Agglomeration Method (LBAM), is used to simulate the electrochemical kinetics in the CL. The lattice elements are determined as an agglomerate of carbon support (Cs), Platinum (Pt), and Ionomer, as shown in Fig. 1.2. Through this method, the agglomerates in the CL are able to apply the kinetic expression and solve the chemical reactions of hydrogen and oxygen to investigate the electrochemical variables such as overpotential, electron transfer, and exchange current in the CL. The Boltzmann transport equation with the source term of chemical reaction will be used to solve for the heat and mass transport in the porous and catalyst layers. The software XFlow 2020 Refresh 1 Beta (Build 108.07) will be used to perform the calculation. Through this modeling, behavior, and characteristics of the reactant gases and products, such as condensed liquid water, oxygen, and water vapor will be investigated under different porous structure and operating conditions. Reacting gases are transported from the flow channel to the catalyst and membrane surface through GDL and MPL. The mass flow

conditions and corresponding water activities in the porous layers will be obtained by macro-scale fuel cell model (STAR-CD 4.20) coupled to the computation of net water flux per proton, the electro-osmotic drag coefficient, and the membrane conductivity.

CHAPTER 2

NUMERICAL DETAIL

2.1 MODEL DEVELOPMENT

The direct-modeling-based LBAM is used to simulate the multi-physics, kinetics, and mass transport in the PEMFC. The multi-scale modeling consists of three main simulation techniques: a macro-scale model, micro-scale LBM, and agglomerate model. Then, these three models are merged using a modification of the co-simulation approach reported by Shimpalee el al. (2019). Typically, catalyst models in the literatures may not be valid at high current density due to simplifying assumption that the CL is a homogeneous continuum. This model has been improved by introducing the nano-structural CL into the LBAM. LBM, incorporated with an agglomerate model, is able to simulate the electrochemical kinetics within the detailed structure of CL, which is useful to the catalyst design by investigating the change in local electrochemical variables such as cell potential and current density with the operating conditions. Note that all the models in this dissertation are unsteady.

Figure 2.1 presents the concept of the co-simulation approach where the fuel cell performance is predicted with a LBAM. The N-S, species (mass) transport, and heat transport equations are used to perform the numerical solution in the flow-field, bipolar plate, and membrane. This method is also used to model the water and heat transport across the membrane. For the micro- and nano- scale model, LBM is used to solve for transport inside the detailed structure of the GDL, MPL, and CL.

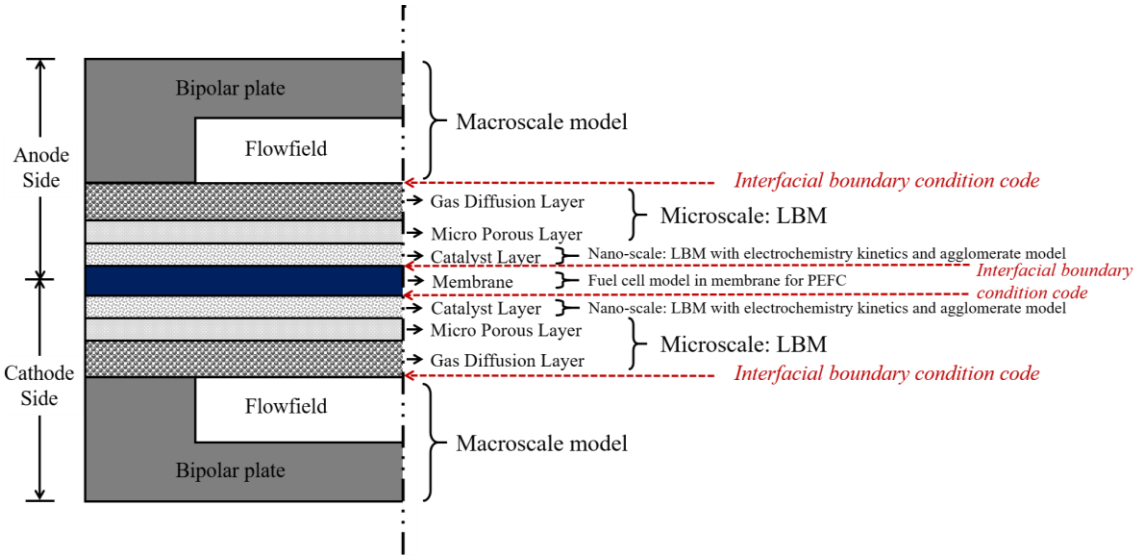

Figure 2.1 Co-simulation approach: Macro-scale model, Micro-scale LBM, and Nano-scale LBAM.

The LBAM is used to predict the distribution of electrochemical variables in the nanoscale CL. The interfacial boundary between the macro-scale and micro-/nano- scale models is used to interchange the numerical data between two models by using the data mappers approach, as shown in Fig. 2.2.

The data mappers approach is used to interpolate the field of data such as velocity field, heat, species mass flux, water sink/source, and heat source from the electrochemical reaction. In this dissertation, the nanoscale CL has been added into the micro-scale component. There are total four interfaces including both anode and cathode that require the data mapper approach in this dissertation. This approach allows the connection between each interface during the simulation that permits all transport properties to pass back and forth efficiently. Each simulation technique has a different grid size and time step. In this study, the indirect grid mapping technique is used to perform the data transfer every ten milliseconds. Below is the detail explanation of specific model applied in this dissertation.

2.2 LATTICE BOLTZMANN METHOD

LBM was originally developed as an improved modification of the Lattice Gas Cellular Automata (LGCA) to remove statistical noise and achieve better Galilean invariance for fast flows. LBM is one of the most powerful techniques for computational fluid dynamics for a wide variety of complex fluid flow problems including single phase, free surface, and multi-phase flow model in complex geometries. The methods concept of streaming and collisions of particles that incorporate the essential physics of microscopic and mesoscopic processes so that the macroscopic averaged properties obey the desired macroscopic equations. Boltzmann's transport equation is defined as follows:

$$f_j\left(\vec{x} + \vec{e}_j\Delta t, t + \Delta t\right) - f_j(\vec{x}, t) = \Omega_j(f_1(\vec{x}, t), \dots, (f_b(\vec{x}, t)), \quad j = 1, \dots, b \qquad (2.1)$$

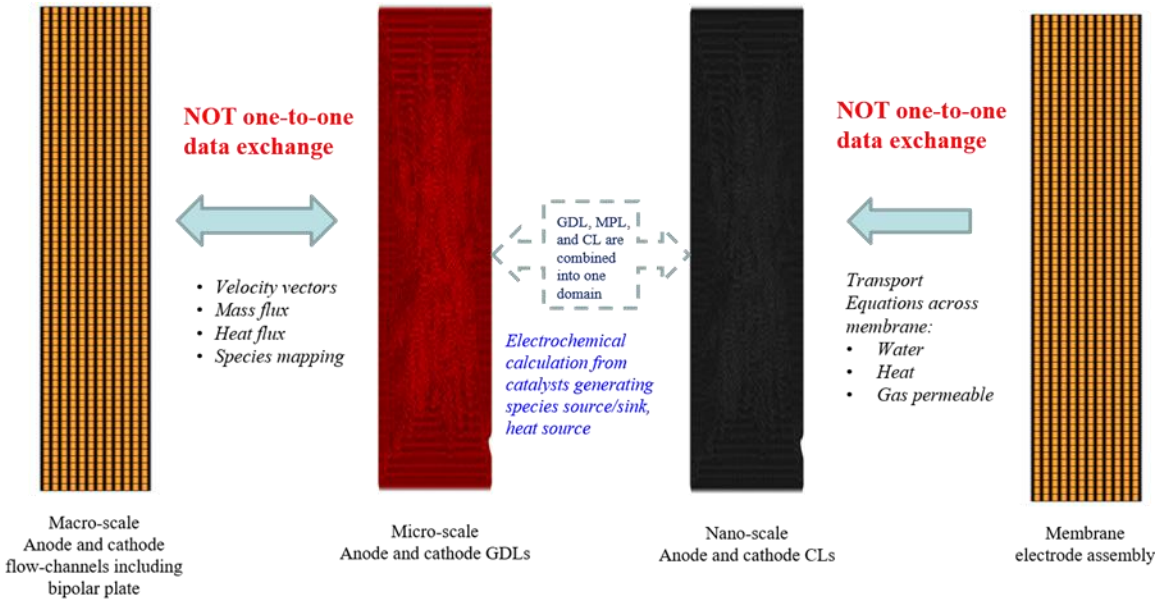

Figure 2.2 Method of interfacial boundary condition transfer and data mappers.

where f_j is the particle distribution function in direction j, $\vec{e}_j$ is the particle discrete velocity, and Ω_j is the collision operator. LBM makes use of a statistical distribution function with real variables, preserving by construction the conservation of mass, momentum, and energy (Chen and Doolen 1998). In the most common approach, the collision operator can be approximated by the Bhatnagar-Gross-Krook (BGK) single relaxation time (SRT) from:

$$\Omega_j^{BGK}(f_j(\vec{x},t)) = \frac{1}{\tau}[f_j^{eq}(\vec{x},t) - f_j(\vec{x},t)] \tag{2.2}$$

The Boltzmann's transport equation with a single relaxation time in the Lattice Bhatnagar-Gross-Krook (LBGK) model for collision operator can be written as:

$$f_j\left(\vec{x} + \vec{e}_j\Delta t, t + \Delta t\right) - f_j(\vec{x},t) = \frac{1}{\tau}[f_j^{eq}(\vec{x},t) - f_j(\vec{x},t)] \tag{2.3}$$

where f_j^{eq} is the equilibrium distribution function and τ is the relaxation time which is related to the macroscopic velocity. Usually, the equilibrium distribution function adopts the following expression:

$$f_j^{eq} = \rho w_j\left[1 + \frac{\vec{e}_{j\alpha}\vec{u}_\alpha}{c_s^2} + \frac{\vec{u}_\alpha\vec{u}_\beta}{2c_s^2}\left(\frac{\vec{e}_{j\alpha}\vec{e}_{j\beta}}{c_s^2} - \delta_{\alpha\beta}\right)\right] \tag{2.4}$$

where c_s is the sound speed, ρ is the macroscopic density, $\vec{u}$ is the macroscopic velocity, δ is the Kronecker delta, α and β subindexes denote the different spatial components of the vectors appearing in the equation, and w_j is the weight factor. The multi-scale Chapman-Enskog expansion gives us the relation between the macroscopic viscosity (ν) and the relaxation parameter:

$$\nu = c_s^2(\tau - \frac{1}{2}) \tag{2.5}$$

$$c = \frac{\Delta x}{\Delta t} \tag{2.6}$$

where Δx is the lattice space and Δt is the time step. For the positive viscosity, $\tau > \frac{\Delta t}{2}$ is required as a stability condition in addition to the relaxation time around 0.5. In the multi-phase fluid flow and multi-component, red and blue particle distribution function were represent two different fluids (e.g., gas phase and liquid phase, liquid phase and solid phase, and gas phase and solid phase) (Chen and Doolen 1998). The total particle distribution function is defined as:

$$f_j^{(m)} = f_j^{(r)} + f_j^{(b)} \tag{2.7}$$

where (m) denotes either the red or blue fluids. The collision operator for Boltzmann's transport equation with a single relaxation time model can be written as:

$$\Omega_j^k = \left(\Omega_j^k\right)^A + \left(\Omega_j^k\right)^B \tag{2.8}$$

where $\left(\Omega_j^k\right)^A$ is the collision operator similar to the Lattice Bhatnagar-Gross-Krook model in Equation 2.2, and $\left(\Omega_j^k\right)^B$ is the additional collision operator contributes to the dynamics in the interface an generates a surface tension defined as:

$$\left(\Omega_j^k\right)^B = A_m \left|\vec{F}\right| cos2\left(\theta_j - \theta_f\right) \tag{2.9}$$

where A_m is a parameter which determines the surface tension by using the definition of mechanical surface tension (σ) , $\vec{F}$ is the local color gradient, θ_j is the angle of lattice direction, and θ_f is the angle of local color gradient (e.g., for fluid-solid interface, θ_f is contact angle).

Macroscopic variables such as density ρ and velocity $\vec{u}$ can be calculated as the moments of the density distribution function.

$$\rho = \sum_{j=1}^{b} f_j \tag{2.10}$$

$$\rho\vec{u} = \sum_{j=1}^{b} c f_j \, \vec{e}_j \tag{2.11}$$

The macroscopic fluid pressures are calculated from the equation of stage:

$$P = \rho c_s^2 \tag{2.12}$$

LBM schemes are classified as a function of the spatial dimensions m and the number of distribution functions n, resulting in the notation *DmQn*. The most common schemes in two dimensions are the *D2Q7* and *D2Q9*, while in three dimensions the most used schemes are the *D3Q13*, *D3Q15*, *D3Q19* and *D3Q27*. In this work the commercial LBM solver, XFlow 2020 Refresh 1 Beta (Build 108.07), was chosen to perform the calculation. This solver uses the twenty-seven velocity D3Q27 lattice model as shown in Fig. 2.3.

The advanced collision operators were approximated by Multiple Relaxation Time (MRT) scheme. In general, collision operators in MRT model schemes are formally defined by:

$$\Omega_j^{MRT} = M_{jl}^{-1} \hat{S}_{jl} \left(m_j^{eq} - m_j \right) \tag{2.13}$$

where the collision matrix $\hat{S}_{jl}$ is a $b \times b$ diagonal relaxation matrix, m_j^{eq} is the equilibrium value of the moment m_j and M_{jl} is a $b \times b$ matrix which transforms the distribution function to macroscopic moment (Shan and Chen 2007; d'Humieres 2007). The collision operator is based on a multiple relaxation time scheme.

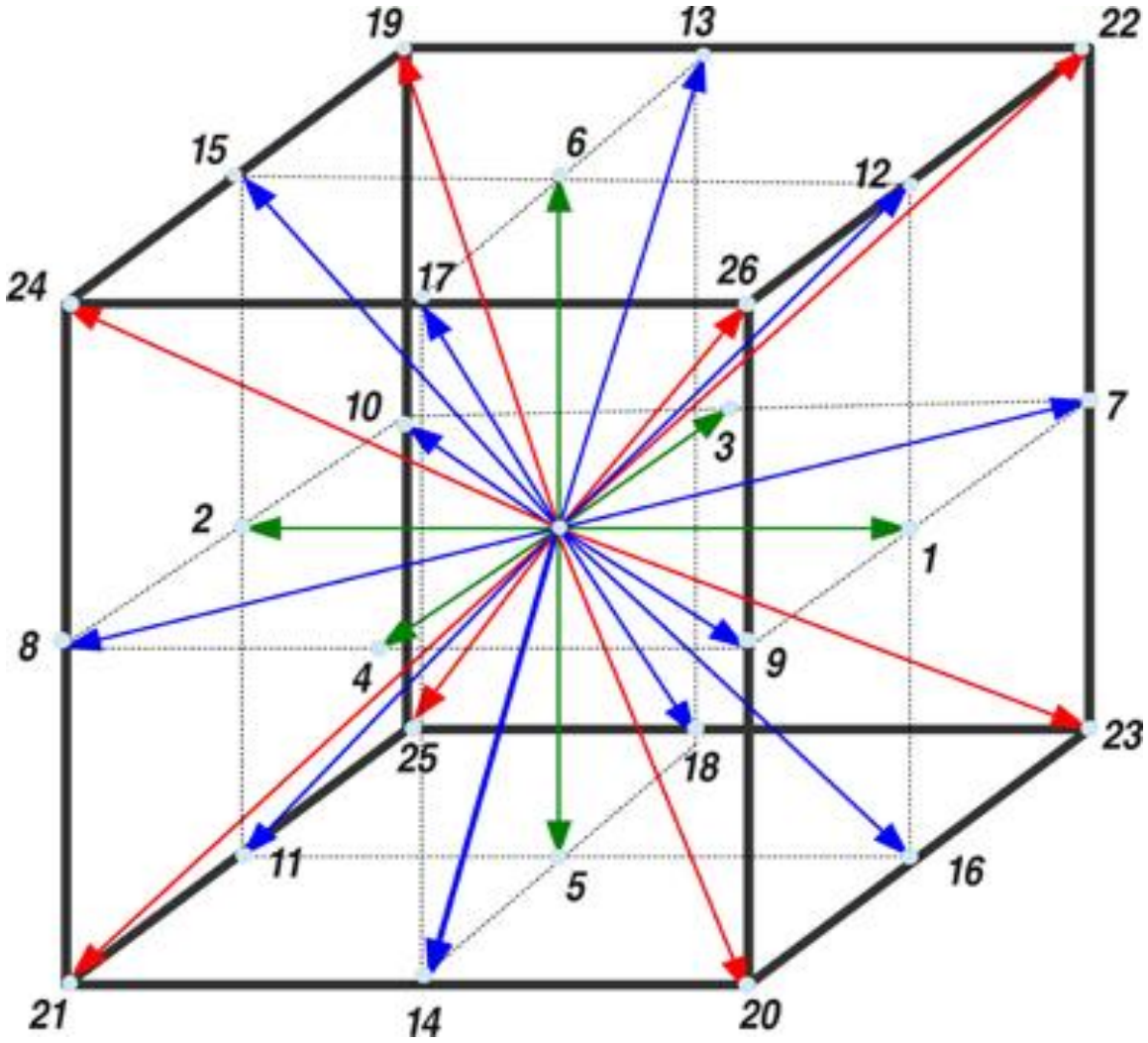

Figure 2.3 The lattice structure of D3Q27 model. The weight factors (w_i) for the D3Q27 are w_0 = 8/27 (the cell-center), w_i = 2/27 (i = 1-6), w_i = 1/54 (i = 7-18), and w_i = 1/126 (i = 19-29).

However, as opposed to standard MRT, the scattering operator is implemented in central moment space. The relaxation process is performed in a moving reference frame by shifting the discrete particle velocities with the local macroscopic velocity, naturally improving the Galilean invariance and the numerical stability for a given velocity set (Holman et al. 2012; Premnath and Banerjee 2012). Raw moments can be defined as:

$$\mu x^k y^l z^m = \sum_j^N f_j e_{jx}^k \, e_{jy}^l e_{jz}^m \tag{2.14}$$

and the central moments can be defined as:

$$\tilde{\mu} x^k y^l z^m = \sum_j^N f_j \left(e_{jx} - u_x\right)^k \left(e_{jy} - u_y\right)^l \left(e_{jz} - u_z\right)^m \tag{2.15}$$

2.3 LATTICE BOLTZMANN AGGLOMERATION METHOD

The LBAM is introduced to perform numerical analysis in the detailed structure of the porous and catalyst layers of the PEMFC. This method is the combination of two numerical simulation techniques consisting of LBM and the agglomerate model. The Boltzmann transport equation was solved and used to predict the mass transport in the GDL, MPL, and CL. This dissertation is unique because it integrates the lattice elements from LBM in the agglomerate of CL. All transport variables from LBM were transferred into the agglomerate model to simulate the electrochemical kinetics distribution in the CL. The lattice elements were defined and represent as the agglomeration of the Cs/Pt/Ionomer to enabled ease of data in a form of CL detailed structures for the LBAM.

In this dissertation, the agglomerate catalyst model (Weber et al. 2014; Harvey et al. 2008; Cetinbas et al. 2014; Moore et al. 2014; Zenyuk et al. 2016) is used to manipulate the local overpotential and volumetric current density at the anode and cathode. It uses a

modified form of the Butler-Volmer equation which considers hydrogen (H_2) and oxygen (O_2) transport within both sides of the CLs. The kinetic expression LBAM simulates the chemical reactions of H_2 and O_2 to investigate the electrical potentials, electrical current, electron transfer, and exchange current in the CL. The expression for the agglomerate current is obtained as the following equations:

$$i_{agg} = \frac{nF\bar{V}_{agg}P_{O_2}}{H_{O_2}}\left[\left(\frac{r_{agg}^2\delta_{agg}}{3D_{O_2}\left(r_{agg}+\delta_{agg}\right)}+\frac{1}{E_r k_c(1-\varepsilon_{CL})}\right)^{-1}\right] \tag{2.16}$$

$$i_{agg} = \int_{V_{agg}} i\,dV = \int_{0}^{r_{agg}} 4\pi r^2 \cdot i\,dr \tag{2.17}$$

$$\bar{V}_{agg} = \frac{r_{agg}^3}{\left(r_{agg}+\delta_{agg}\right)^3} \tag{2.18}$$

$$r_{agg} = \left[\frac{4}{3}\pi(1-\varepsilon_{CL})(2r_{lattice})^3\right]^{\frac{1}{3}} \tag{2.19}$$

where i_{agg} is the total agglomerate volumetric current density, i is the current per unit volume in the CL, n is the number of electrons involved in the reaction per mole of reactant, F is the Faraday's constant, P_{H_2} is the hydrogen pressure, P_{O_2} is the oxygen pressure, H_{H_2} is the Henry's constant of hydrogen, H_{O_2} is the Henry's constant of oxygen, E_r is an effectiveness factor of the spherical agglomerate, ε_{CL} is the CL porosity, $\bar{V}_{agg}$ is the active area scaling factor, r_{agg} or r is the agglomerate radius, $r_{lattice}$ is the lattice radius, V_{agg} is the agglomerate volume, V is the total volume that agglomerate and thin-film occupy, δ_{agg} is the thickness of the Nafion™ film, D_{H_2} is the diffusivity of the dissolved hydrogen in Nafion™, and D_{O_2} is the diffusivity of the dissolved oxygen in

Nafion™. The reaction rate at the surface of the agglomerate core of anode (k_a) and cathode (k_c) are shown in the below equation:

$$k_a = \frac{a_{Pt}^{eff} i_{o,a}}{nFC_{H_2}^{ref}} \left[exp\left(\frac{\alpha_a F}{RT}\eta_a\right) - exp\left(-\frac{(1-\alpha_a)F}{RT}\eta_a\right)\right] \quad (2.20)$$

$$k_c = -\frac{a_{Pt}^{eff} i_{o,c}}{nFC_{O_2}^{ref}} \left[exp\left(\frac{-\alpha_c F}{RT}\eta_c\right) + exp\left(\frac{(1-\alpha_c)F}{RT}\eta_c\right)\right] \quad (2.21)$$

where a_{Pt}^{eff} is the effective reaction area, $i_{o,a}$ is the anode exchange current density, $i_{o,c}$ is the cathode exchange current density, R is the ideal gas constant, T is the local temperature, $C_{H_2}^{ref}$ is the reference hydrogen concentration, $C_{O_2}^{ref}$ is the reference oxygen concentration, and α_c is the anode charge transfer coefficient. The kinetic expression used in the catalyst model to calculate the over-potential for both the cathode and anode CLs are shown below:

$$\eta_a = \frac{RT}{\alpha_a F} ln\left[\frac{i \times P_{H_2}^{ref}}{i_{0,a} \times P_{H_2}}\right] - \frac{RT}{2F} ln\left[\frac{P_{H_2}^{ref}}{P_{H_2}}\right] \quad (2.22)$$

$$\eta_c = \frac{RT}{\alpha_c F} ln\left[\frac{i \times P_{O_2}^{ref}}{i_{0,c} \times P_{O_2}}\right] + \frac{RT}{4F} ln\left[\frac{P_{O_2}^{ref}}{P_{O_2}}\right] \quad (2.23)$$

where η_a is the local anode overpotential, η_c is the local cathode overpotential, $P_{H_2}^{ref}$ is the reference hydrogen pressure or hydrogen inlet pressure, $P_{O_2}^{ref}$ is the reference oxygen pressure or oxygen inlet pressure. The effective reaction area (a_{Pt}^{eff}) is a function of specific platinum surface area per unit CL volume (a_{Pt}), Pt loading (m_{Pt}), Pt density (ρ_{Pt}), CL thickness (t_{CL}), and the CL porosity (ε_{CL}), are used to calculate the effective reaction area for the portions of the CL that are unable to encounter the requirements for the electrochemical reaction:

$$a_{Pt}^{eff} = \frac{a_{Pt} m_{Pt}}{\rho_{Pt} t_{CL}(1 - \varepsilon_{CL})} \tag{2.24}$$

The anode and cathode exchange current density are a function of the reference exchange density $i_{o,a}$ and $i_{o,c}$, activation energy (E_{act}), and local temperature. The anode and cathode exchange density are shown in the equation below:

$$i_{o,a} = i_{o,a}^{ref} exp\left[\frac{-\Delta E_{act}}{R}\left(\frac{1}{T} - \frac{1}{T_0}\right)\right] \tag{2.25}$$

$$i_{o,c} = i_{o,c}^{ref} exp\left[\frac{-\Delta E_{act}}{R}\left(\frac{1}{T} - \frac{1}{T_0}\right)\right] \tag{2.26}$$

The effectiveness factor of the spherical agglomerate is obtained by the analytical solution of the effectiveness of the electrode reaction. This can be explained as a ratio of the actual reaction rate to the rate if the entire interior surface is exposed to the conditions outside of the particle (Yoon and Weber 2011). The effectiveness factor is shown in the following equation:

$$E_r = \frac{1}{\emptyset_{L,c}}\left(\frac{1}{tanh(3\emptyset_{L,c})} - \frac{1}{3\emptyset_{L,c}}\right) \tag{2.27}$$

where $\emptyset_L$ is the Thiele's modulus, which characterizes the reaction transport process for a given geometry. Thiele's modulus for chemical reactions can be found as:

$$\emptyset_L = \frac{r_{agg}}{3}\sqrt{\frac{k_c}{D_{eff,O_2}}} \tag{2.28}$$

where D_{eff,O_2} is the effective diffusivity of dissolved reactant (O_2) in Nafion™ presented in the agglomerate core and is approximated by using Bruggeman's relation (Harvey et al. 2008; Moore et al. 2014). The equation describing proton transport can be derived with the electro-neutrality assumption, which is then reduced to Ohm's law, i.e.,

$$\nabla \cdot \left(D_{\emptyset}^{eff} \nabla \cdot \emptyset_m \right) = \nabla \cdot i \tag{2.29}$$

where $D_{\emptyset}^{eff}$ is the effective diffusion coefficient of proton conductivity, and $\emptyset_m$ is the electrolyte potential.

2.4 MACRO-SCALE MODEL

The macro-scale model is a conventional CFD based model that used to solve the coupled governing equations (i.e., N-S, species transport, and heat transport) inside flow-field, bipolar plate, and membrane. The mass flow conditions and corresponding water activities in the porous layers will be obtained by macro-scale model coupled to the computation of net water flux per proton, the electro-osmotic drag coefficient, and the membrane conductivity. A commercial software (STAR-CD 2019.1.1) is used to perform the numerical analysis and shared the transports as the boundary conditions to the LBAM model.

2.5 NUMERICAL PROCEDURE

In this dissertation, there are difference numerical procedure that used to perform numerical calculation by including direct modeling-based LBM and LBAM. The LBM modeling is used to examine the liquid water transport inside the porous layers that used in PFMFCs. The model prediction is used to compared and validated with *ex-situ* breakthrough pressure and *in-situ* flow visualization. The LBAM is used to perform the numerical simulation of electrochemical kinetics and multi-physics/species transport inside porous layers for PEMFCs.

For the *ex-situ* and *in-situ* models validation, direct-modeling-based LBM combined with *ex-situ* and *in-situ* flow visualization, is used to explore fundamentally the transport of liquid-water inside the gas-diffusion layers (GDLs) used in PEMFCs. The

time-dependent simulations of liquid-water saturation inside a GDL for PEMFCs with a free surface model were run for several GDL samples, SGL10BA, SGL24BA, SGL25BC, that were injected with water in a variety of configurations. The LBM solver uses 3 spatial dimensions and 27 discrete velocities (i.e. *D3Q27*). The lattice element size was 1 μm, giving a total number of 17,117,826 to 23,403,898 elements, depending on the size and resolution of the computed geometry. The time step was set to 0.1 μs. The liquid-water was injected under the sample at the same locations and pressures as in the experiments (i.e. beginning at 500 Pa and increasing by 500 Pa until breakthrough pressure is reached). The surface tension of liquid-water was set to 0.072 N/m, which corresponds to the surface tension of water in contact with air at 25 °C. Surface tension is also responsible for the contact angle (θ) where a surface meets a GDL surface. This is determined by the interactions across the fluid-fluid and fluid-solid interface. The GDL contact angle in the simulation was assumed to be constant and uniform at 130°. The maximum computational time was 12 hours using 20 cores in a single node of an Intel Xeon 2.8 GHz with 256 GB RAM.

Aimed at modeling of electrochemical kinetics by using LBAM modeling, 3D time-dependent simulations of electrochemical kinetics and multi-physics/species transport inside porous layers for PEMFCs with the LBAM multi-phase flow model were run for these GDL, MPL, and CL. The computational lattice sizes were dependent on the size and the resolution of computed geometry. The lattice size was 1.33 μm for GDL and MPL. The adaptive lattice spacing approach was applied to the surface of the CL with a lattice size of 10 nm. The agglomerate structure was exported from the lattice structure in the CL with the diameter of 1.00 μm. LBM was used lattice node and voxels to replace the typical

computational meshes for its direct numerical simulation. According to the size of geometry, the time step was set to 0.001 microsecond per time step for micro- and nano-scale LBAM model. For the macro-scale model, the time step was set to 1.00 millisecond per time step. Through this modeling, the behavior and characteristics of the reactant gases and products, such as condensed liquid water, O_2, and water vapor were investigated under various operating conditions. Reacting gases are transported from the flow channel to the catalyst and membrane surfaces through the GDL and MPL. The mass flow conditions and corresponding water activities in the porous layers were obtained with a macro-scale model coupled via the computation of net water flux per proton, the electro-osmotic drag coefficient, and the membrane conductivity, as discussed above. The MPL was assumed to be a porous region and the Darcy-Ergun equation was applied to calculate pressure drop across the medium and solve the mass transport inside the MPL (Chen and Doolen 1998). Heat and mass transport in porous layers are governed by the Boltzmann transport equation with the source term of the chemical reaction, which is an integral-differential equation of time, real space, and phase space. The software XFlow 2020 Refresh 1 Beta (Build 108.07) was used to perform the calculation. This dissertation also used the kinetics and mass transport information from the macro-scale model as a boundary condition. The agglomerate model was computed using MATLAB R2018b coupled to the transport data from LBM. The parameters used by the agglomerate model are reported in Table 2.1.

The two simulation models were selected for evaluation the electrochemical kinetics in this dissertation. The first model was used for examining the LBAM modeling technique, as an examination case. The second model was used with the LBAM for studying the local transport losses and electrochemical kinetics in 50 cm^2 reactive area.

Table 2.1 Electrochemical reaction kinetics and agglomerate model parameters.

Parameter	**Symbol**	**Value**	**Units**
Agglomerate radius	r_{agg}	50	nm
Effective Agglomerate surface area	a_{agg}	3,600	cm^2/cm^3
CL Porosity	ε_{CL}	0.460	-
CL Thickness	t_{CL}	9	μm
Ionomer thin-film thickness	δ	8	nm
CL active surface area of Pt	a_{Pt}	4.382×10^4	cm^2/cm^3
Pt loading	m_{Pt}	0.300	mg/cm^2
O_2 diffusion coef. in Nafion™	D_{O_2}	8.450×10^{-6}	cm^2/s
H_2 diffusion coef. in Nafion™	D_{H_2}	2.000×10^{-6}	cm^2/s
Henry's constant	H	3.166×10^{10}	$Pa.cm^3/mol$
Reference O_2 concentration	$C_{O_2}^{ref}$	8.500×10^{-7}	mol/cm^3
Reference H_2 concentration	$C_{H_2}^{ref}$	5.640×10^{-5}	mol/cm^3
Cathode Ref. current density	$i_{o,c}^{ref}$	1.500×10^{-6}	A/cm^2
Anode Ref. current density	$i_{o,a}^{ref}$	2.295×10^{-3}	A/cm^2

In the first model, this examination case was introduced for comparison between the macro-kinetics model and LBAM. Note that the macro-kinetics model is the sub-model of macro-scale model, which is reported by Shimpalee et al. (2017 and 2019) and Satjaritanun et al. (2019). The GDL sample used in this model was SGL 25BC. The computational domain examined was divided from the 2,000x2,000x240 μm^3 sample, which has a size of 470x800x240 μm^3, as shown in Fig. 2.4 The cathode side of the fuel cell was assumed to be the control in this model. The gas inlet was fed at the left-hand side of the computational domain, which is the inlet boundary, as shown in the right-hand side of Fig. 2.4 The reaction surface boundary was set at the top of the domain, as shown in the right-hand side of Fig. 2.4 also. For the operating condition, the average current density of 1.0 A/cm^2 was applied to the reaction interface boundary. Air (O^2 and N^2) was fed to the cathode inlet flow boundary at a stoichiometric ratio of 2.0 at 1 atm. The cell temperature was maintained at 70 °C with a relative humidity of 100%. The transport equations mentioned above were applied to predict transport behavior, kinetics and multi-phase/phase-change physics inside the GDL, MPL, and CL.

The second model was used for performing the LBAM in the 50-cm^2 parallel flow-field with 23 straight channels, as shown in Fig. 2.5 This model is used for studying and investigating the local transport losses, partial flooding, diffusion resistance, electrochemical kinetics, and cell performance. The co-flow condition was applied in this case. In this dissertation, there are different three locations (#1, #2, and #3) that represent the inlet, middle, and exit area, respectively. In each selected location has a computational domain of 2,000x2,000x240 μm^3. In previous work (Shimpalee et al. 2019), the homogeneous CL was used to simulate the kinetics by utilizing the macro-kinetics model.

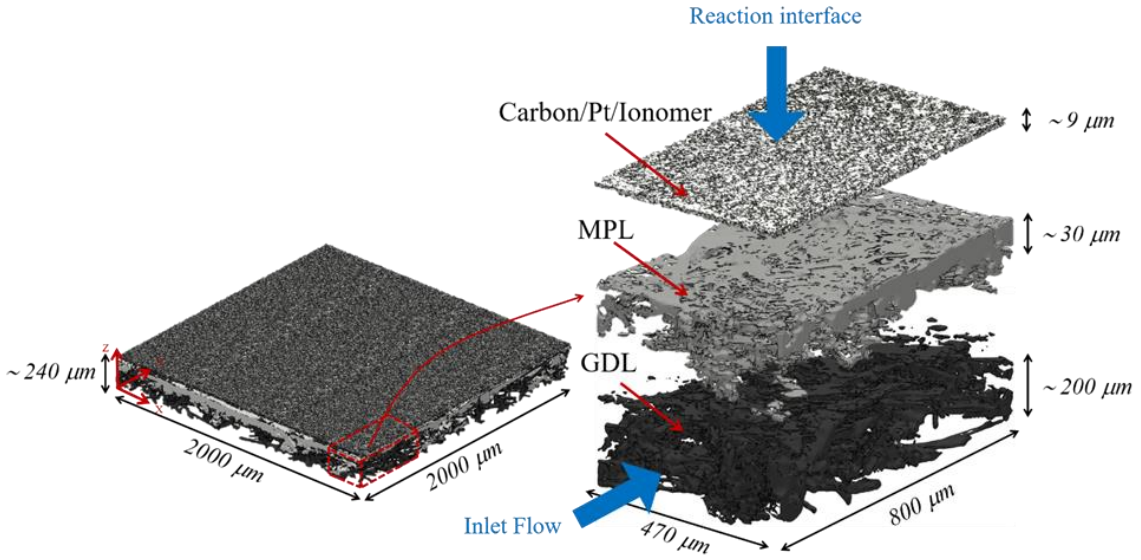

Figure 2.4 Detail structure of GDL, MPL, and CL that used for examination the LBAM modeling technique.

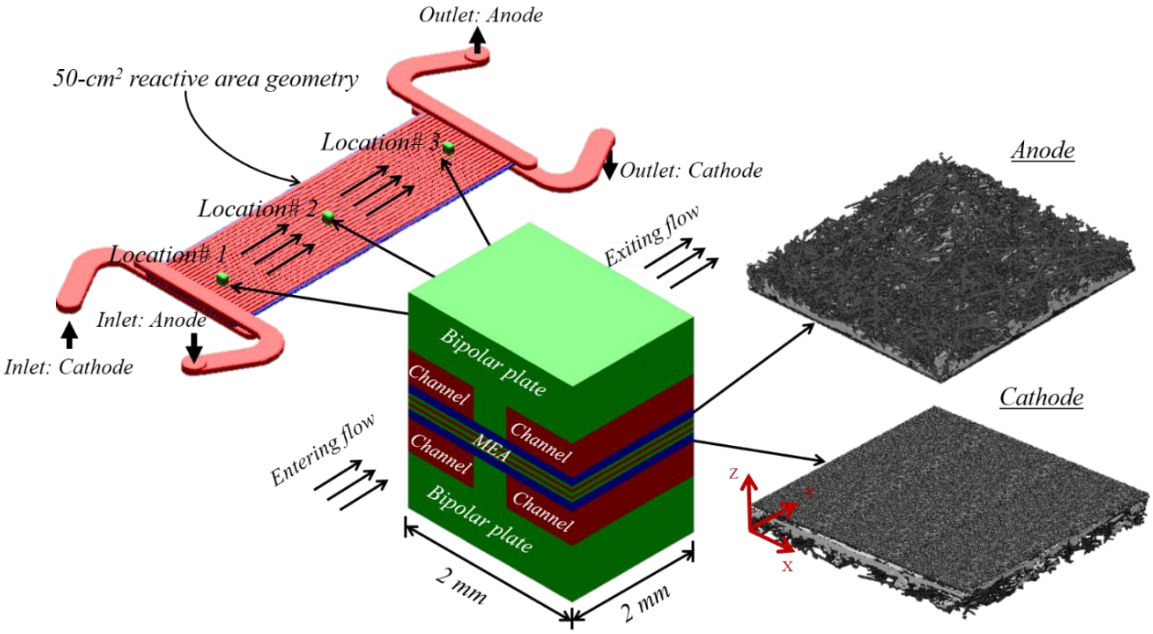

Figure 2.5 Details of multi-scale model of 50-cm^2 reactive area geometry. Macro-scale: 23 Straight channels flow-field with bipolar plates and MEA, Micro-scale: SGL 25BC, and Nano-scale: CL Ion Power.

In this work, the detailed structure of the CL is introduced into this simulation, which is able to predict the local electrochemical kinetics by using the LBAM. The comparison between two models that used a detailed CL (LBAM) and homogeneous CL (Multi-scale model) have been reported in this work. For operating condition, the current density was set at 1.0 A/cm^2 with the cell temperature of 60 °C. The H^2 gas was fed to the anode side with a fixed stoichiometric ratio of 10 at 1.0 A/cm^2. The air gas was fed to the cathode side with a fixed stoichiometric ratio of 15 at 1.0 A/cm^2. The system pressure was set at 251 kPa with a dewpoint temperature of 60 °C for both sides. The maximum computational time was 36 hours using parallel computing under 22 cores in a single node of Linux cluster (Intel Xeon 2.8 GHz with 256 GB RAM).

CHAPTER 3

MODEL VALIDATION OF MICRO- AND NANO-SCALE WITH EX-SITU DATA

3.1 INTRODUCTION

The main objective of this chapter is to validate micro- and nano-scale model by predicting the breakthrough pressure of liquid water transport through the GDL and/or MPL used in PEMFCs. The integration of structural GDL and MPL with LBM is primary focused in this chapter. The numerical predictions are also compared with experimental data. The interaction between liquid phase and different surface treatments of solid structures controls the evolution of liquid water and the change of capillary pressure. The geometries of GDLs and MPLs were obtained by three-dimensional reconstructed micro-structure images from both nanometer and micrometer-scaled high spatial resolution X-ray computed tomography (CT). The predictions of water breakthrough pressure agree with the data observed in the experiment. They also reveal that the breakthrough pressure and liquid water evolution inside the GDL samples are different when the wetting properties of GDL and/or MPL are changed. The detailed microporous property can be obtained using high spatial resolution image from nanometer-scaled X-ray CT, a.k.a. Nano X-ray CT. Meanwhile, images from micrometer-scaled X-ray CT, a.k.a. Micro X-ray CT, give proper field of view to cover complete vision of porous materials, including cracks in the MPL.

3.2 WATER BREAKTHROUGH PRESSURE MEASUREMENT

The water breakthrough pressures of the commercially available GDLs were measured in an *ex-situ* setup, as shown in Fig. 3.1. In this setup, the GDL was sandwiched between two stainless steel plates. Water was injected into the GDL (or GDL/MPL) through the bottom plate via uniformly drilled holes of 1 mm diameter with 1 mm interspaces in a ∅ = 25 mm circle. The actual water/GDL contact area was limited to a diameter of 22 mm by using a 125 μm thick adhesive-backed PTFE film (McMaster-Carr), which prevents lateral water leakage from occurring. To ensure the proper GDL compression, a 125 μm thick hydrophilic PVDF membrane (GVWP02500, 0.22 μm, Millipore) of a diameter of 22 mm was placed in the center hole of the PTFE film. This hydrophilic membrane has a negative capillary pressure and is capable of high flow rate of water; therefore, it does not affect the water breakthrough behavior, but acts to distribute water uniformly over the GDL surface. The top stainless-steel plate is a mirror image of the bottom plate and was used as the water outlet. GDL samples with ∅ = 34 mm were die cut and tested in the experiment. The compression of GDL was monitored with a load cell and kept at 200 psi, which is a typical GDL compression in a fuel cell stack.

The water injection rate was controlled by a syringe pump (Harvard Apparatus 11 Elite). After an initial testing of a wide range of injection rates, the water injection rate for the GDL water breakthrough studies was fixed at 43 μL/min, which corresponded to an equivalent water production rate at current density of 2.0 A/cm^2 and to a capillary number on the order of 10^{-6}. The liquid pressure, as referenced to the atmospheric pressure, was measured with a differential pressure transducer (Model FDW2AR, Honeywell) and was recorded with a National Instruments DAQ system at 100 Hz.

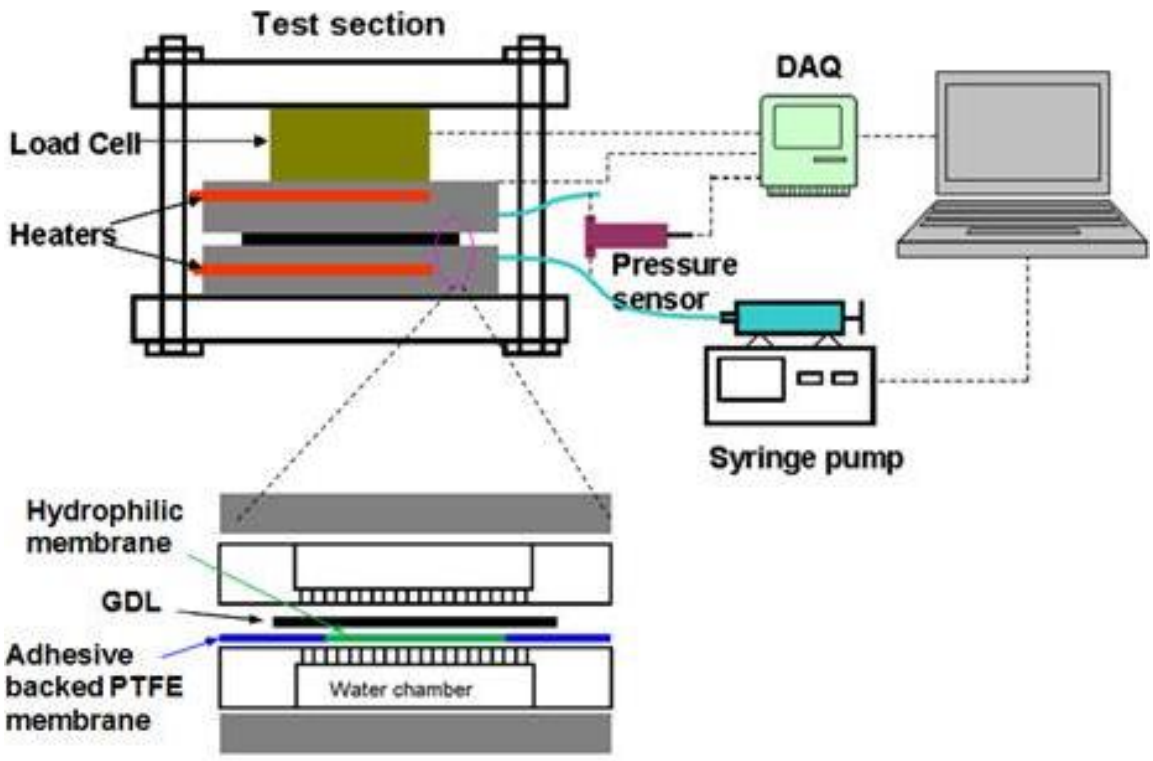

Figure 3.1 Setup for ex-situ water breakthrough and transport in GDL.

Assuming that the air pressure in the GDL is equilibrated with the ambient pressure, the pressure transducer directly measures the capillary pressure (i.e., the pressure difference between the water and the air across the meniscus within GDL.)

Thermal gradients within the GDL were avoided by controlling the temperatures of the top and bottom plates to a common temperature with two electrical heaters. The bottom plate was designed with a water reservoir of about 5 mL. This reservoir volume was much larger than the amount of water injected to GDL (typically less than 0.5 mL); it is therefore reasonable to assume that the water was maintained at a constant temperature during the injection even though the water pipeline itself was not temperature controlled in the experiment. The GDL materials investigated in the work and the measured water breakthrough pressures are listed in Table 3.1.

3.3 WATER BREAKTHROUGH IN GAS DIFFUSION LAYER WITHOUT MICRO POROUS LAYER

Figure 3.2 shows a single piece from a GDL sample (SGL 24BA) reconstructed by Nano X-ray CT. Figure 3.2a show raw data of selected unprocessed virtual slices from reconstructed scans. Figure 3.2b presents an image of 3D rendering with the size of 65 μm diameter. This image also provides the separation of 3 carbon fibers and PTFE/binder structure. It is noted that the PTFE/binder structure shown in this image is noisy and some binders could not be clearly detected. These undetected binders found in this work is around 10% of the total volume of the sample. Figure 3.2c is the computational geometry converted from 3D rendered image and it is also split into 2 solid parts, fibers and PTFE/binder. Therefore, the properties of both solid parts can be individually input (e.g., contact angle of liquid water to the solid surface).

Table 3.1 GDL materials and measured water breakthrough pressures.

GDL	Description	Water contact angle (°)	Water breakthrough pressure (kPa)	Stagnation pressure (kPa)
SGL 24BA	Single-layer, teflonated with 5 wt% PTFE	138 ± 3	1.8 ± 0.1	1.12 ± 0.1
SGL 25BC	Bi-layer, teflonated and MPL coated (5 wt% PTFE in substrate with 23 wt% PTFE in MPL)	153 ± 2 (MPL side)	7.6 ± 0.2	4.75 ± 0.2

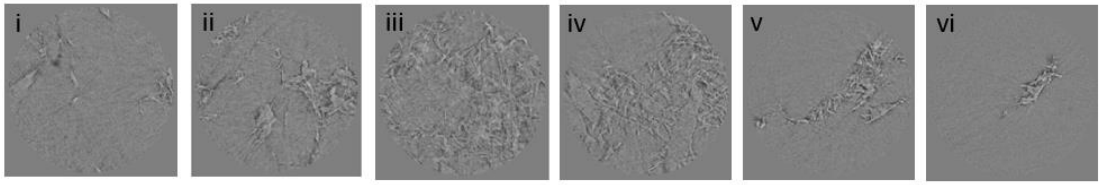

(a)

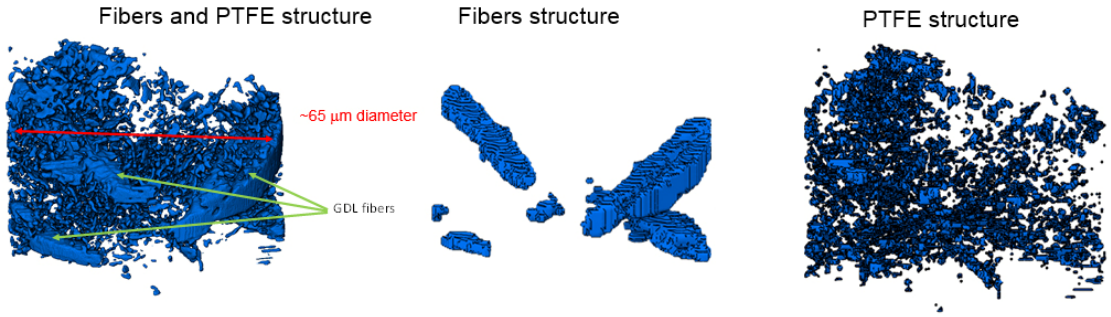

(b)

(c)

Figure 3.2 The reconstructed micro-structure of GDL and PTFE from Nano Computed Tomography. a) raw data before binarization b) 3D rendered image with the separation of fibers and binder/PTFE c) computed geometry used in LBM.

In this section of study, the contact angle of PTFE/binder structure was varied at 40°, 90°, and 140° and the contact angle of carbon fibers were fixed at 90°. It is noted the change in wettability of binder/PTFE can control the different surface treatment during the manufacturing process. The liquid water was fed from the top to the bottom of the geometry with the same condition as given in the experimental setup (43 μl/min).

Figure 3.3 shows the prediction of liquid water evolution from LBM with different wettability of PTFE/binder structure. The maximum time for these calculations was 23 hrs. The shape of liquid water and its growth are different with the change of contact angle of PTFE/binder structure. The high hydrophobicity case (140° contact angle) presents significant different appearance compared to the others (90° and 40° contact angles) as it needs more energy to push the water through the GDL.

The evolution of liquid water is high sphericity for higher hydrophobicity (non-wetting) of PTFE/binder as liquid water has high contact angle on the structure. The pressures when the liquid water breaks through the GDL from all three predictions are given in Fig. 3.4. This graph shows pressure versus dimensionless time (*tD*) for three different wettability of PTFE structure. This pressure was numerically measured by the difference between the pressure of liquid water at the location where the liquid water is fed and pressure at the outlet. So, when the liquid water is moving through the GDL and the exit location is occupied by air, this pressure is also known as capillary pressure. Once the liquid water passes through the GDL and continuously flows inside the pore-network of GDL toward the exit, the pressure difference is stagnation pressure (sum of dynamic pressure and static pressure). Also, in this work, dimensionless time is defined as the ratio of local time to the time approaching steady state.

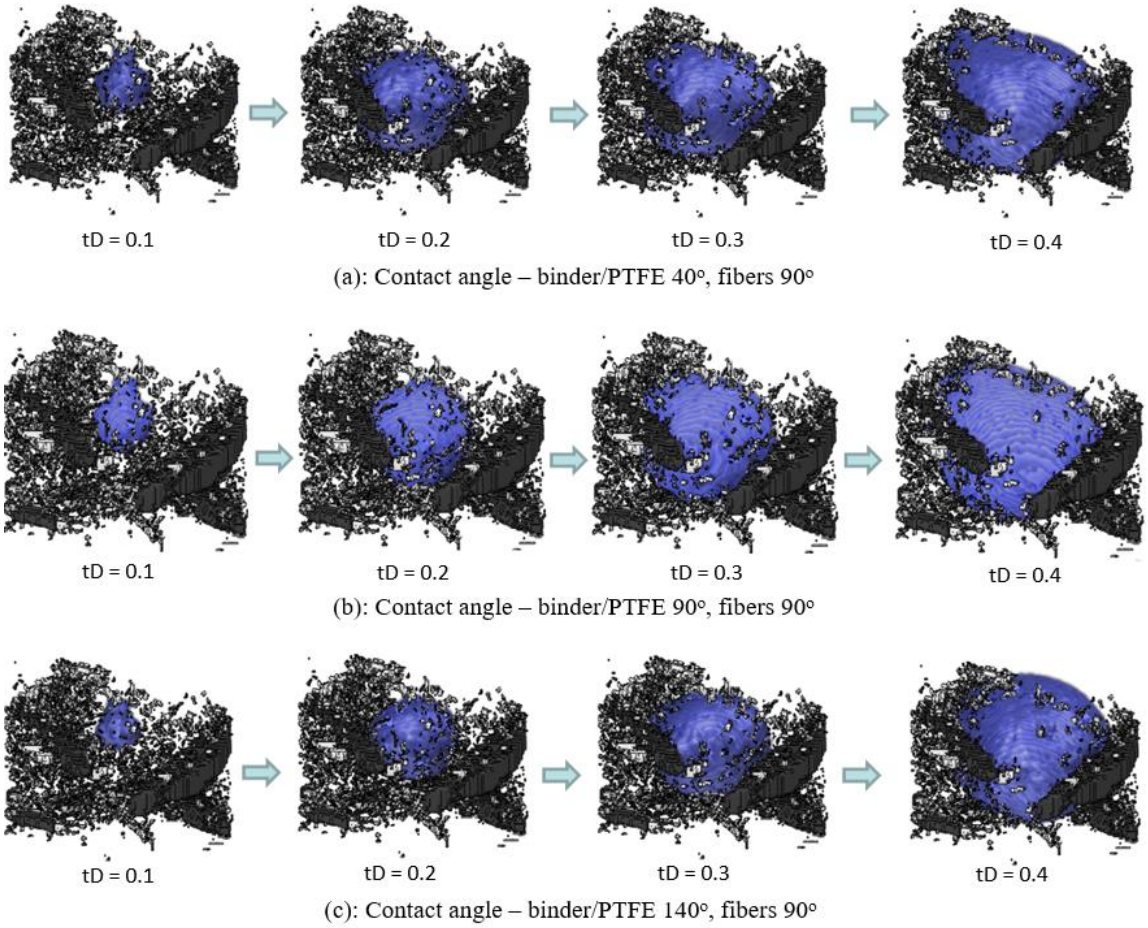

Figure 3.3 Prediction of the effect of wettability on liquid water evolution.

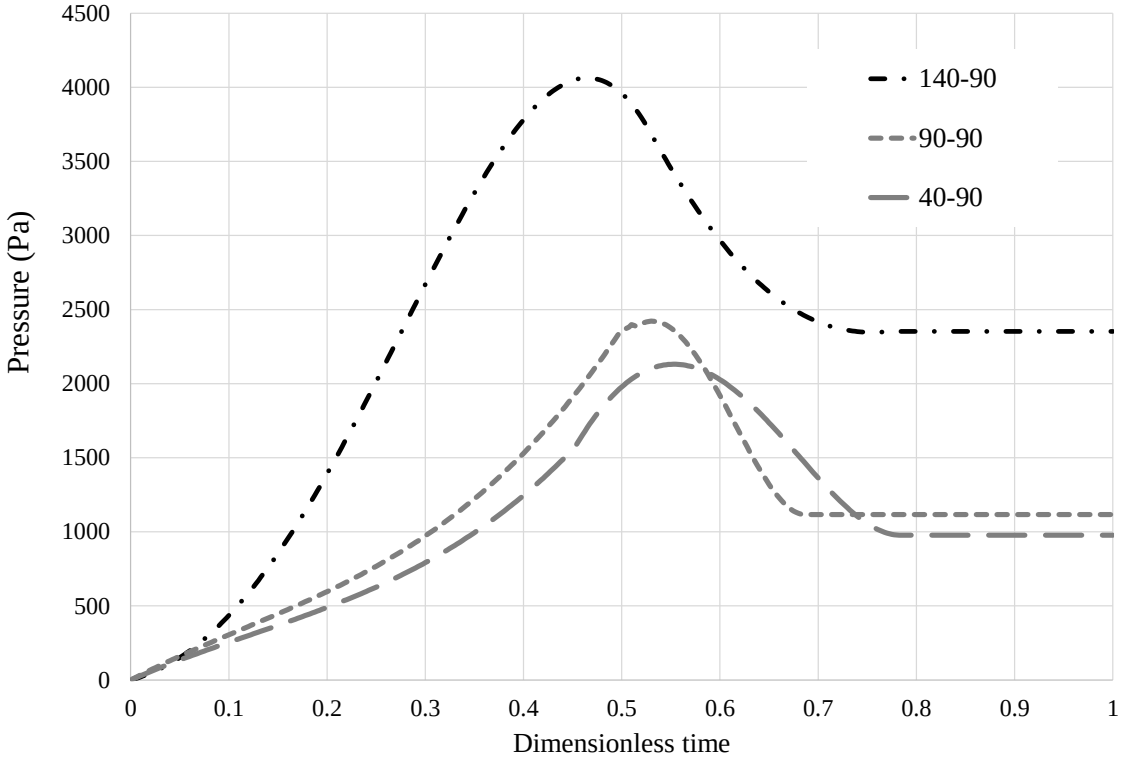

Figure 3.4 The effect of wettability of water breakthrough pressure (Pa) for original binder/PTFE dispersion.

All plots show similar profiles as the capillary pressure rises to the maximum when the liquid water passes through the GDL then it decreases to the steady state value as capillary pressure no longer holds and it changes to stagnation pressure as liquid water flows through the pore structure of GDL. The capillary breakthrough pressure was chosen at the maximum pressure for each case. The case of high contact angle or non-wetting of PTFE structure gives the highest breakthrough pressure of 4,000 Pa. The breakthrough pressure decreases as the PTFE structure changes to the more wetting material. However, the case of 90° contact angle shows slightly higher water breakthrough pressure than 40° contact angle.

The next simulation was computed using the same GDL sample but the image was taken and rendered from the Micro X-ray CT. Figure 3.5a the raw data of cross-section tomography for grey-scale and threshold data of SGL 24BA (Zenyuk et al. 2016). Mostly, Otsu algorithm was used to segment the data. Although the binder shows some micro-porosity, its nano-porosity is not resolved with micro-CT (Zenyuk et al. 2016). Figure 3.5b shows the detailed structure of GDL and it has a much larger size than the image taken by Nano X-ray CT but this image has a lower resolution (i.e., 2.58x1.20x0.24 mm^3). As shown in the figure 3.5, both fibers, PTFE structure, and binders are combined to one solid piece. In order to compare the prediction of breakthrough pressure with the previous results that were calculated using the smaller geometry from Nano X-ray CT, three random locations of the GDL in Fig. 3.5b were chosen and they all have the same volume as the volume of geometry imaged from Nano X-ray CT. Figure 3.5c shows the three GDL structures that were randomly picked from different positions shown Fig. 3.5b (Positions 1, 2, and 3).

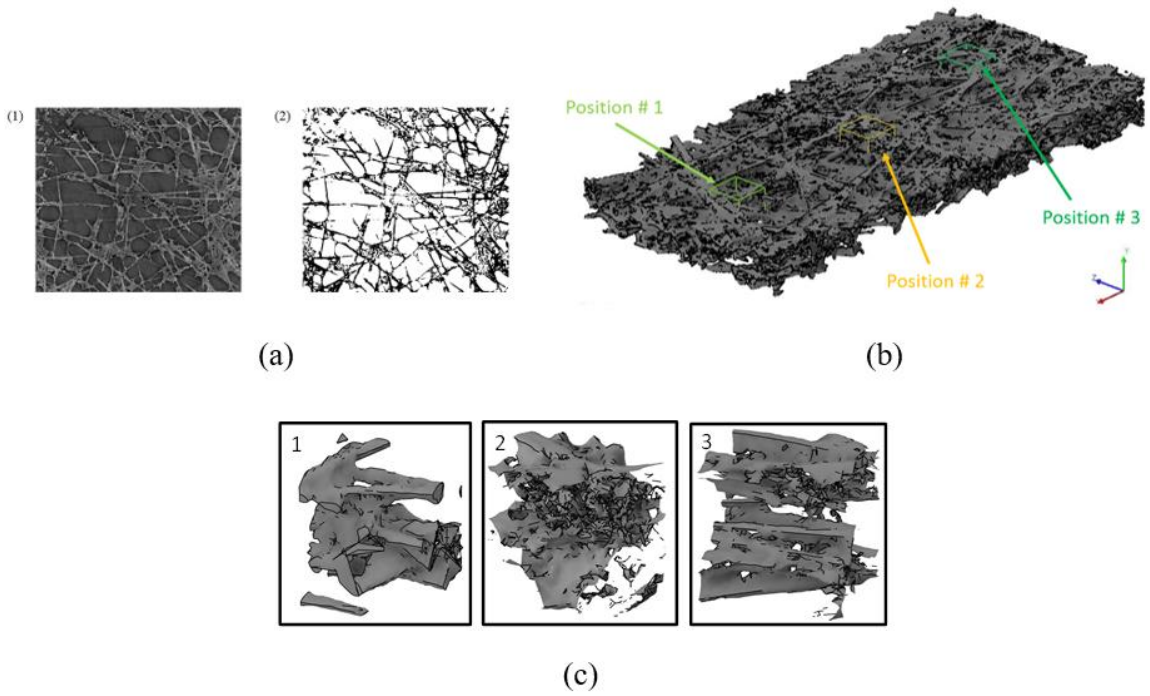

Figure 3.5 3D rendered image from Micro Computed Tomography of SGL 24BA a) cross-section tomography for greyscale (1) and threshold data (2), b) 3D rendering image, c) Locations 1, 2 and 3 were selected for water breakthrough predictions.

These GDLs have different structure and porosity. Positions 1, 2, and 3 have porosity of 0.7, 0.5, and 0.6, respectively. As mentioned above that the image taken by Micro X-Ray CT, the solid parts of GDL cannot be separated due to its limited resolution. Therefore, only the wetting property of the single solid part can be input into the model.

Figure 3.6 shows the prediction of pressure profile against dimensionless time for three different positions as given in Fig. 3.5. Once again, the maximum pressure of each profile represents the water breakthrough pressure. This figure also provides the snapshots of water evolution inside the GDLs that have the same contact angle of 90°. Note that the longest time of calculation in these studies was 12 hrs. The overall predictions give the same summary as given in the simulation using higher resolution image from Nano X-ray CT. The maximum breakthrough pressure is shown at the high contact angle (i.e., 140°) and both contact angle of 90° and 40° show similar pressure profile. The GDL at Position# 1 where the solid structure is loose and has the highest porosity gives the maximum breakthrough pressure of 1,750 Pa with stagnation pressure of 1,450 Pa for contact angle of 140° and the minimum of 1,100 Pa with stagnation pressure of around 1,020 Pa for the contact angle of 40°. The water evolution also confirms that the liquid water simply moves from the top to the bottom of GDL. At Position # 2 where the GDL has the densest of solid structure and the lowest porosity, the highest breakthrough pressure rises to 3,650 Pa with stagnation pressure of 1,750 Pa and the lowest breakthrough pressure increases to around 1,600 Pa with stagnation pressure of around 1,370 Pa. With the lower wettability of solid structure, the breakthrough pressure seems to be more sensitive to the porosity of the GDL. The snapshots of the water movement reveal that it requires more pressure than other positions to push liquid water through the GDL.

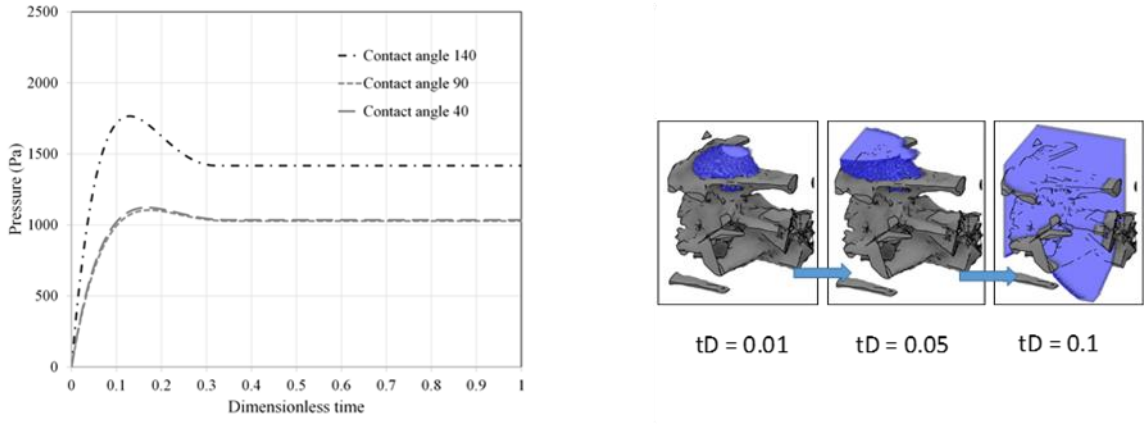

(a)

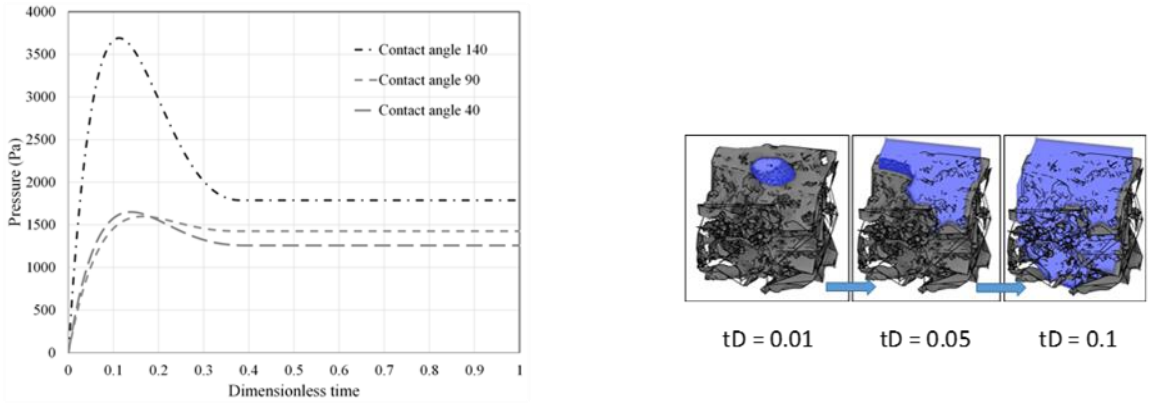

(b)

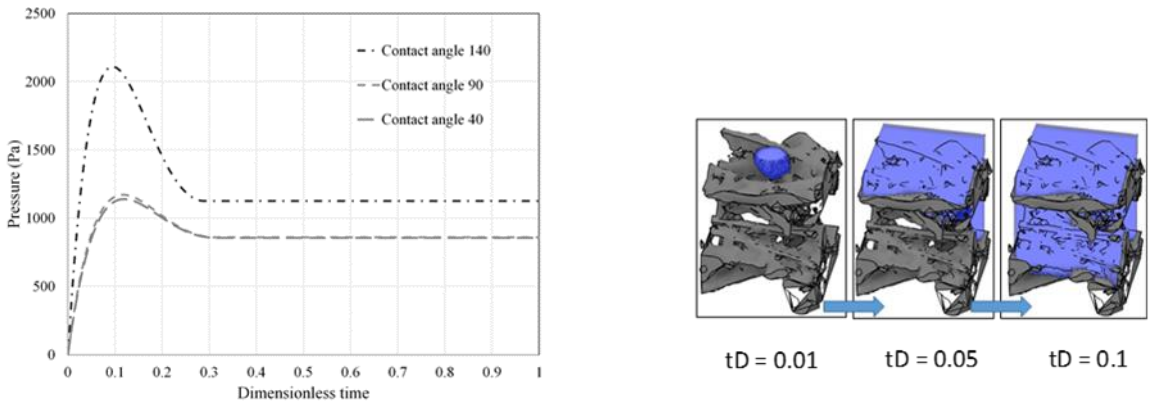

(c)

Figure 3.6 The effect of wettability on water breakthrough pressure (Pa) in SGL 24BA from 3D Micro CT at a) Position # 1, b) Position # 2, and c) Position # 3. The snapshots of water transport inside GDL at wettability of 90° contact angle.

The GDL at Position# 3 has the porosity value of 0.6 which it is not too coarse or too dense. It has the dense structure at the top and bottom but has high porosity in the middle. The maximum pressure at contact angle of 140° is 2,100 Pa with stagnation pressure of approximately 1,200 Pa and the minimum pressure at contact angle of 40° is 1,200 Pa with stagnation pressure of around 820 Pa. The water transport behavior is similar to the case of GDL at Position# 2. But once it passes through the dense area of solid structure at the top, the liquid water easily move to the bottom and then additional pressure is created to pass through it. The average maximum breakthrough pressure from those three GDL at the contact angle of 140° is around 2,500 Pa and the average minimum breakthrough pressure at the contact angle of 40° is around 1,320 Pa. Moreover, the average maximum stagnation pressure from those three GDL at the contact angle of 140° is around 1,467 Pa and the average minimum breakthrough pressure at the contact angle of 40° is around 1,070 Pa. From the experiment described above (i.e., Water Breakthrough Measurement), the breakthrough pressure of SGL 24BA GDL is 1,770 Pa and the stagnation pressure (steady state pressure) is around 1,120 Pa which are in the range of model predictions.

The model prediction of water breakthrough pressure was extended to the larger size of SGL 24BA GDL taken from Micro X-ray CT as shown in Figure 3.7. This GDL is around two orders of magnitude larger than the size taken from Nano X-ray CT. The pressure profiles of the three cases at different contact angles vary from the smaller size in Fig. 3.6 especially in the case of 90° contact angle. The breakthrough pressure at 90° contact angle gives a much higher value than the case at 40° contact angle. The maximum of these calculation times was 27 hr.

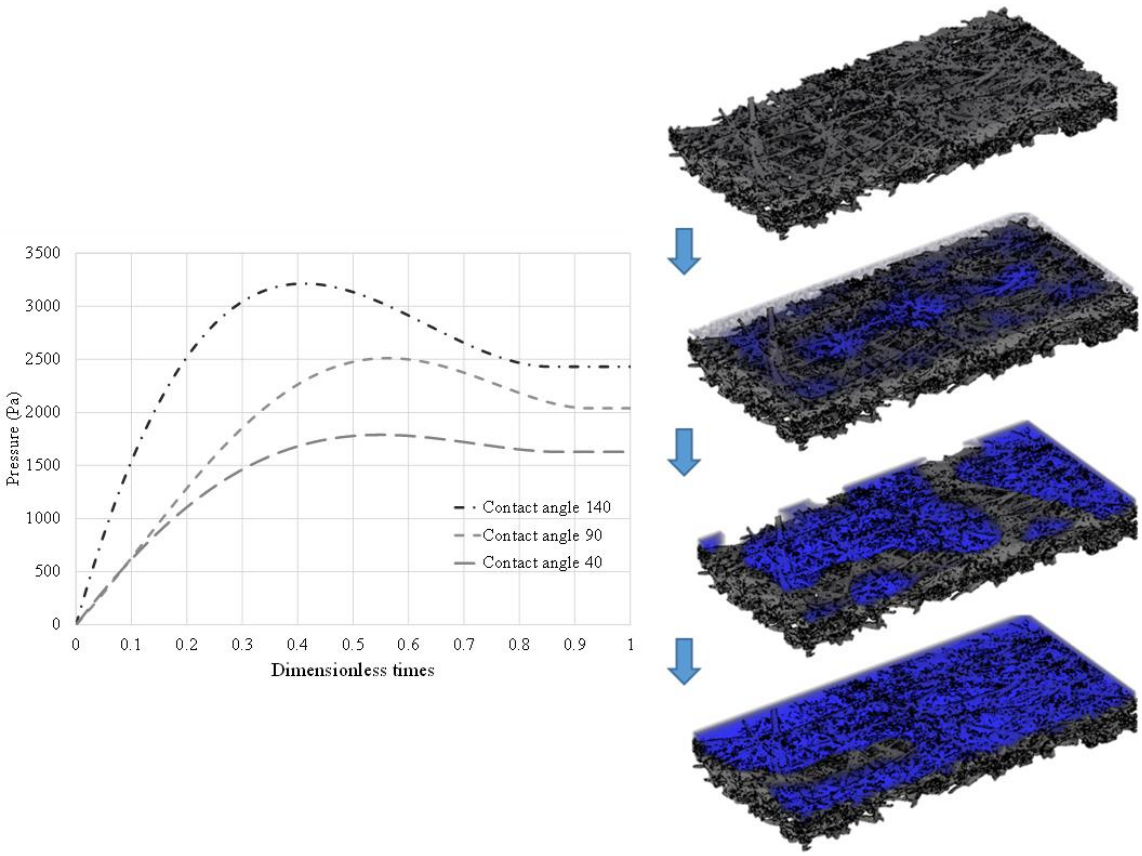

Figure 3.7 Prediction of water breakthrough pressure (Pa) at different contact angle and snapshots of liquid water transport inside SGL 24BA at contact angle of 90°.

The values of the breakthrough pressure are 3,300, 2,500, and 1,750 Pa for contact angle of 140°, 90°, and 40°, respectively. They are also in the range of the value taken by the breakthrough experiment. For the stagnation pressure, the values are 2,450, 2,000, and 1,520 Pa for contact angle of 140°, 90°, and 40°, respectively. The water evolution shows liquid water spreading layer by layer of the GDL from top to bottom.

3.4 WATER BREAKTHROUGH IN GAS DIFFUSION LAYER WITH MICRO POROUS LAYER

In order to predict water breakthrough pressure of GDL with MPL, the structure of MPL needs to be included into the model. Figure 3.8 shows the 3D reconstructed GDL, MPL, and PTEF/Binders used in this simulation. Figure 3.8a show the structure of MPL of SGL 25BC from Nano X-ray CT with the dimension only 3.375 cubic micron. But the fiber and PTFE shown in Fig. 3.8b has the dimension of 15,625 cubic and it has the area of 277 times larger than the geometry of MPL shown in Fig. 3.8a. Moreover, there is an evident crack on MPL as provided in Fig. 3.8c. Therefore, before creating the complete geometry of GDL and MPL, the surface area of MPL from Fig. 3.8a must be increased by manually performing the periodic repetition of the Nano X-ray CT data. So that the MPL has the same surface area as GDL as shown in Fig. 3.8b. Then the space was also manually made to represent the crack shown in Fig. 3.8c. Figure 3.8d presents the complete geometry taken by Nano X-ray CT that was used for water breakthrough simulation using LBM. Due to the complexity of MPL micro-structure, the maximum computational time was increased to 100 hrs.

Figure 3.9 presents the snapshots of water evolution inside the GDL and MPL. As the MPL is located on only one side of the GDL, the water breakthrough pressure prediction was performed at both sides, MPL to GDL (Figure 3.9a), and GDL to MPL (Figure 3.9b).

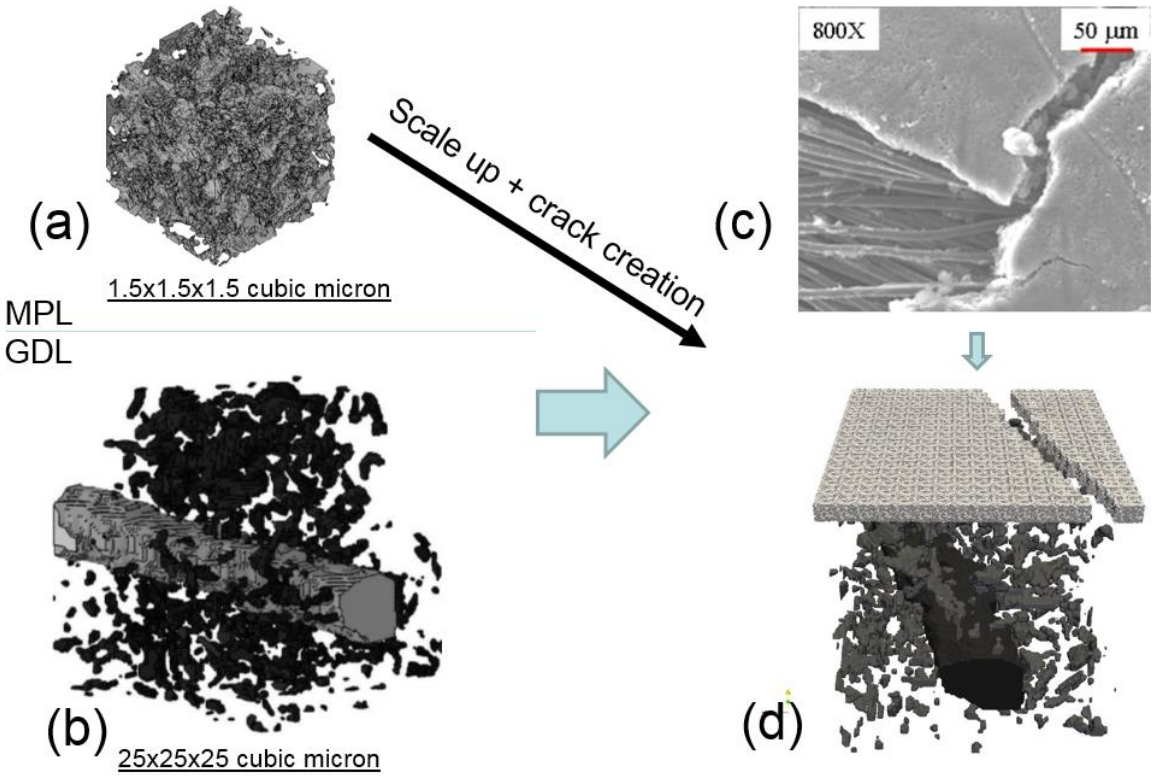

Figure 3.8 The reconstructed micro-structure of GDL, PTFE, and MPL from Nano X-ray Computed Tomography. a) Micro porous layer (MPL), b) GDL with fiber binder/PTFE, c) the SEM showing cracks in MPL and d) combined GDL and MPL for computed geometry in LBM.

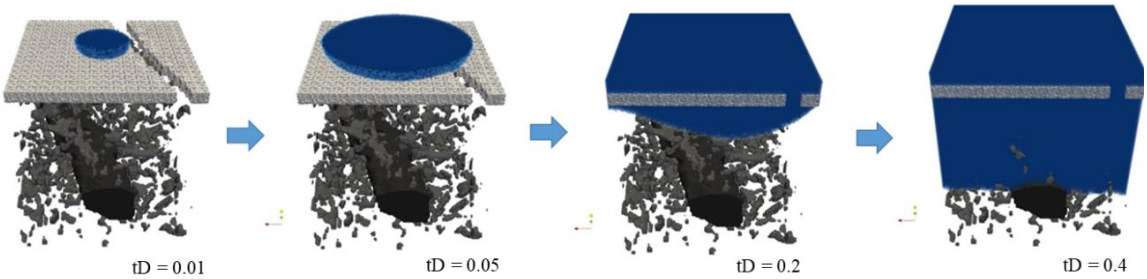

(a) From MPL thru GDL

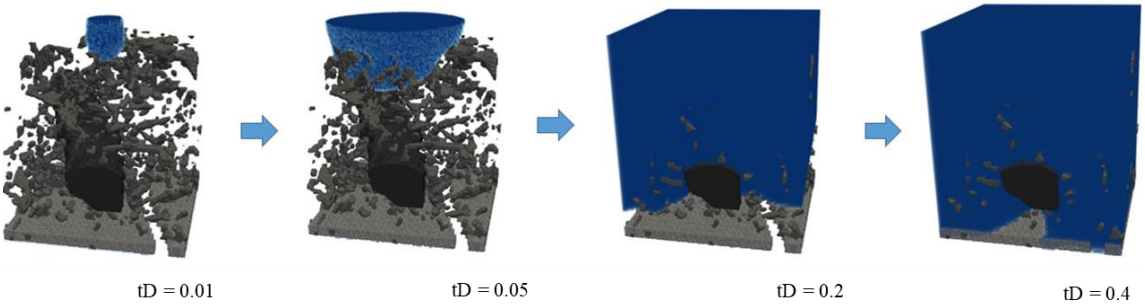

(b) From GDL thru MPL

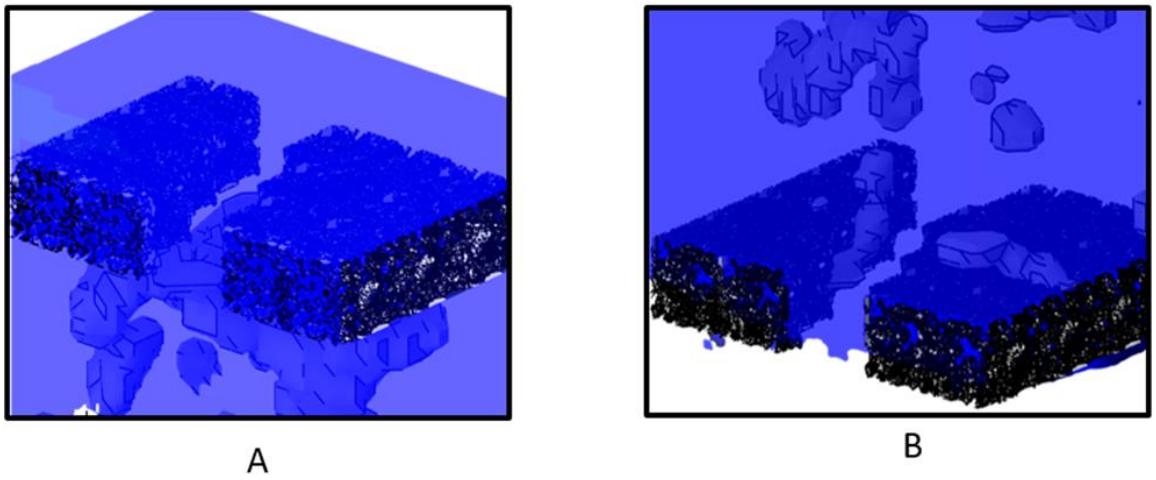

(c) Close-up view showing liquid water penetrates through MPL and crack

Figure 3.9 Snapshots of water transport during water breakthrough: a) liquid water was push from MPL thru GDL, b) liquid water was push from GDL thru MPL, and c) close-up view of MPL and crack.

With the 3D structure taken from Nano X-ray CT, the fiber, PTFE/binder, and MPL structure can be individually separated. In this study, only wettability of PTFE/binder structure was varied, and the rests were kept constant at 90° contact angle. Both Figures 3.9a and 3.9b show different progression of liquid water during breakthrough process. When the liquid water was pushed from MPL to GDL, liquid water spread all over the MPL before it moves toward the GDL. This is because the pressure required to push the liquid water thru the MPL structure or the crack in MPL is higher than the pressure used for liquid water spreads on the top of MPL. But when the liquid water moved from GDL to MPL, liquid water easily transported and grew through the fiber and PTEF/binder structure inside the GDL then liquid water accumulated over the MPL layer and moved past MPL once it reached the breakthrough pressure. Figure 3.9c shows the close-up views of liquid water passes through MPL and crack from both in Figure 3.9a and Figure 3.9b.

Figure 3.10 presents the pressure profiles during the movement of liquid water when it was pushed from MPL to GDL (Figure 3.10a) and from GDL to MPL (Figure 3.10b). The contact angle of solid fiber of GDL was fixed at 90° whereas PTFE/binder of GDL and solid structure of MPL were varied at 40°, 90°, and 140°. The overall profiles are similar to the predictions of GDL without MPL from Nano X-ray CT as the pressure increases until it reaches the breakthrough pressure then it decreases to the steady state value. The contact angle of 40° gives the lowest pressure profile following by the pressure profiles at 90° and 140° contact angle. When the liquid water was pushed from the MPL to the GDL as shown in Fig. 3.10a, the increase in pressure with dimensionless time for 140° and 90° contact angle values are similar as liquid water was spread all over the top of MPL before it moves to the GDL.

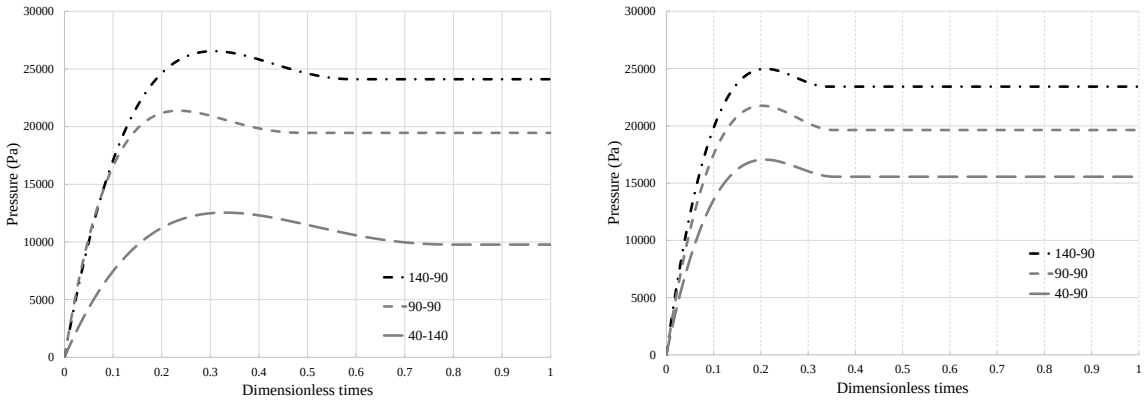

(a) (b)

Figure 3.10 The effect of wettability on water breakthrough pressure (Pa): a) liquid water was push from MPL thru GDL and b) liquid water was push from GDL thru MPL.

Because the required pressure to push the liquid water completely through the MPL and the crack is higher than the pressure needed to spread liquid water on top of the MPL. After the liquid is fully spread out these two cases give different pressure profiles. For the case at a 40° contact angle, the pressure profile is different compared to the other two cases. This is due to the hydrophilic nature of the solid surface which allows liquid water to flow through the MPL and crack with less pressure than non-wetting surface. It gives the maximum pressure of 12.5 kPa before it drops to around 10.0 kPa at stable pressure. The case at a 90° contact angle shows the maximum pressure of 21.0 kPa and then the pressure decreases to a steady state value of 19.5 kPa. For the case of a 140° contact angle, the pressure increases to reach the maximum at 26.5 kPa then it slightly reduces to reach the steady value at 24.0 kPa. Figure 3.10b shows the pressure profiles with different contact angles when the liquid water was pushed from GDL. The profiles of all three cases are similar but with different values. This is because the liquid water transports from the coarse structure of GDL through the fine/dense structure of MPL and therefore these pressure profiles are proportional to the wettability of porous material. The breakthrough capillary pressure is 26.0 kPa, 20.0 kPa, and 17.0 kPa for the contact angle of 140°, 90°, and 40°, respectively. It is noted that the overall values of pressure profiles and breakthrough pressure are much higher than the experimental data (i.e., For SGL 25BC, the breakthrough pressure is 7,600 Pa and the stagnation pressure is 4,750 Pa). This could be due to 1) the sample size used in experiment is much larger than it is used in the LBM model and 2) the MPL used in experiment has multiple cracks with different sizes whereas there is only one artificial crack in the MPL geometry and it much smaller than what was observed due to the geometry size used in the model. It is noted that Shimpalee et al. (2016) demonstrated

the water evolution and its breakthrough pressure inside the GDL with no-crack MPL. Their predictions give very high breakthrough pressure as around 10 times of experimental value.

The reconstructed micro-structure of SGL 25BC GDL from Micro X-ray CT geometry was also used to exercise the model. Figure 3.11a shows cross-section tomography, threshold data with blue represents fiber and red denotes MPL, and 3D rendered image of SGL 25BC (GDL and MPL). As mention earlier that the detailed structure of GDL/MPL from Micro X-ray CT gives only one single solid domain. Therefore, the MPL from this geometry was converted to solid layer with several cracks also shown in Fig. 3.11a. In order to predict the liquid water transports through both MPL and cracks, the cracks were preserved while the solid part of MPL was replaced by porous model and its properties were taken from the measurement in 3D reconstructed micro-structure of MPL of SGL 25BC from Nano X-ray CT as shown in Fig. 3.8a. In the LBM used in this work, the porous model applies the Darcy-Ergun formulation to calculate pressure drop (Δp) across the media:

$$\Delta p = -th\left(\frac{\mu}{k}v + \rho\frac{c_E}{\sqrt{k}}v^2\right) \tag{3.1}$$

where k is the permeability, v is the velocity normal to the porous surface, c_E is the Ergun coefficient of 0.2, and th is the sample thickness. The porosity of the MPL is 52% and the permeability is around $1.0\text{x}10^{-15}$ m^2 for all directions. Figures 3.11b and 3.11c present the snapshots of water transport during the water breakthrough progression. Figure 3.11b shows the snapshots when the liquid water was pushed from MPL to GDL and Figure 3.11c shows when the liquid water was pushed from GDL to MPL. The contact angle of solid structure was set at 90° for both figures.

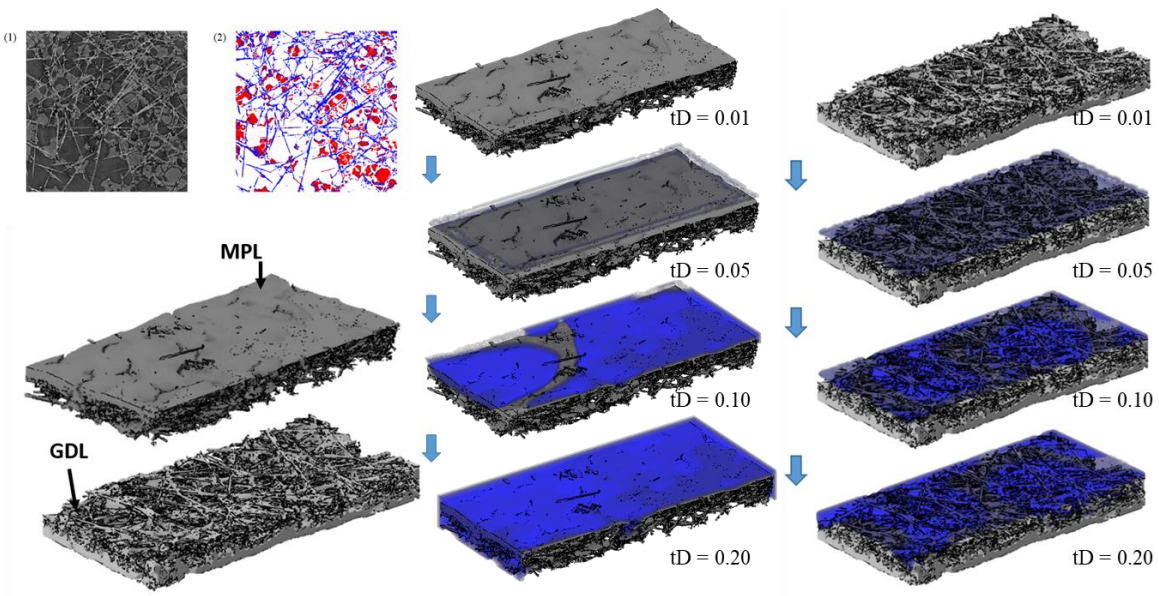

Figure 3.11 Snapshots of water transport during water breakthrough: a) cross-section tomography (1), threshold data (2) (blue is fibers; red is MPL, and 3D rendering image of SGL 25BC, b) liquid water was push from MPL thru GDL for the contact angle of 90° and c) liquid water was push from GDL thru MPL for the contact angle of 90°.

The behavior of liquid water is similar to what it was shown in Figs. 3.9a and 3.9b using the geometry from Nano X-ray CT. Figure 3.11b shows the liquid water spreads over the top of MPL before it breaks through the MPL and then GDL. In Figure 3.11c, the liquid water grows throughout the GDL structure and stays on top of MPL before it breaks through the cracks and MPL. With this approach, the maximum calculation time was reduced to 36 hrs.

Figure 3.12 presents the pressure profiles during water evolution starting from MPL to GDL (Figure 3.12a) and from GDL to MPL (Figure 3.12b). The contact angle of solid structure was varied over the contact angle of 40°, 90°, and 140°. The overall profiles are similar to the predictions of GDL without MPL (i.e., SGL 24BA) as the pressure increase to reach the breakthrough pressure then it decreases to the stable value. The wettability of 140° gives the highest-pressure profile following by the pressure profiles of 90° and 40° contact angle conditions. When the water was pushed from the top of MPL to the GDL as shown in Fig. 3.12a, the increasing in pressure with dimensionless time for all three contact angle values are similar as liquid water was spread all over the top of MPL. Then all three cases give the pressure profiles differently. The case of 40° contact angle gives the maximum pressure of 4,500 Pa before it drops to 4,000 Pa at the stagnation pressure (stable pressure). The case of 90° contact angle shows the maximum pressure of 6,000 Pa and then the pressure decreases to 4,500 Pa. For the case of 140° contact angle, the pressure increases to reach the maximum at 7,800 Pa then it slightly reduces to reach the steady value at 6,900 Pa. As already mention, the maximum pressure is the breakthrough pressure or capillary breakthrough pressure. Once liquid pass through and occupy all pore networks, the capillary pressure will no longer hold thus, reducing to static liquid water pressure.

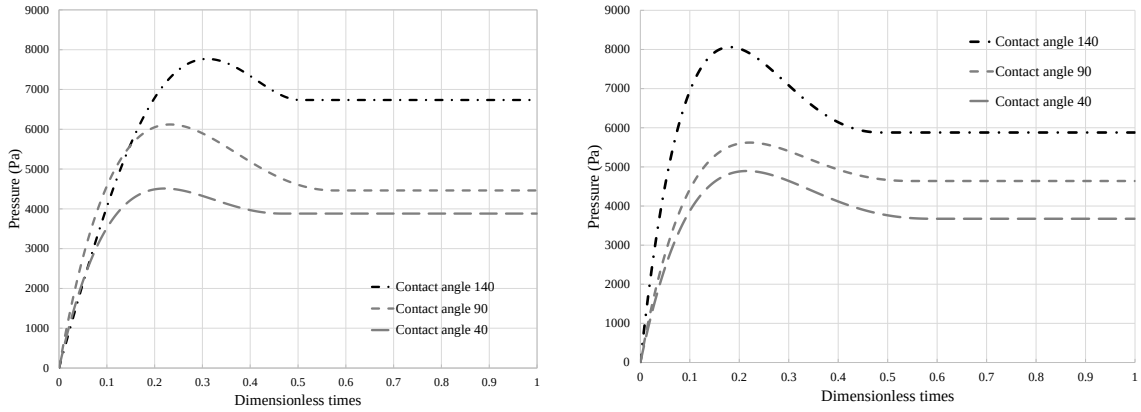

Figure 3.12 The effect of wettability on water breakthrough pressure (Pa): a) liquid water was push from MPL thru GDL and b) liquid water was push from GDL thru MPL.

Figure 3.12b shows the capillary pressure profiles with different contact angles when the liquid water was push from GDL to MPL. Once again, the pressure profiles are similar to the predictions from Nano X-ray CT structure. The breakthrough capillary pressure is 8,000 Pa, 5,700 Pa, and 5,000 Pa and the stagnation pressure is 6,000 Pa, 4,600 Pa, and 3,630 Pa for the contact angle of 140°, 90°, and 40°, respectively.

The values of breakthrough pressure from both orientations shown in Figure 3.12 are close to the value observed in the experiment especially at the contact angle of 140°. With the range of breakthrough pressure with contact angle, the contact angle of 135° from Fig. 3.12a and 131° from Fig. 3.12b represent the angle that are needed to represent the breakthrough pressure measurement. The predictions of breakthrough pressure are also much lower than the predictions from geometry taken by Nano X-ray CT. This is because the size of SGL 25BC used in the model is compatible to the one used in the experiment even though the detailed PTFE/binder has been ignored. Further, the number of cracks and their size are same as the real sample as the resolution and the scale from Micro X-ray CT can capture those details.

3.5 SUMMARY

In this chapter, a three-dimensional numerical simulation using the Lattice Boltzmann Method has been introduced to study the water transport inside the porous material used in polymer electrolyte membrane fuel cells. The liquid water breakthrough dynamics across the GDL with and without a MPL were predicted and compared with an ex-situ experimental data. The geometries of 3D reconstructed micro-structure GDL and MPL from both micro-scale and nanoscale X-ray CT were used to exercise the model. From the images taken by both resolutions, the overall predictions are in the range of data

observed in experiment. The motion of liquid water in the pore structure MPL can only be predicted using the geometry taken by Nano X-ray CT. However, the size of 3D reconstructed MPL requires tremendously scale up in order to create a complete GDL with MPL model geometry. The simulation technique by applying the transport properties of MPL from Nano X-ray CT to porous layer of MPL from Micro X-ray CT appears to predict well and it will require less computational resources. The breakthrough capillary pressure and the evolution of liquid water inside the GDL samples are different with the change of wetting properties of GDL and/or MPL. Due to the irregular and inconsistent shape of pore space in porous material used in PEMFC, it is impossible to only solve Young-Laplace equation and provide the qualitative conclusion. A more detailed analysis of local saturation of liquid water under breakthrough dynamics across the GDLs with and without an MPL was shown in Appendix A. The LBM technique can successfully simulate to two-phase transport inside the porous media using the geometries from both Nano and Micro X-ray CT depending on the purpose of the research. The properties of carbon fiber and other components such as binders and PTFE can be separated using high resolution image from Nano X-ray CT but the sample will be very small whereas, Micro X-ray CT give much larger sample and wide-ranging vision of porous material but the detailed structure inside cannot be observed and separated.

CHAPTER 4

MODEL VALIDATION OF MICRO-SCALE WITH IN-SITU DATA FLOW VISUALIZATION

4.1 INTRODUCTION

In this chapter, direct-modeling-based LBM combined with *in-situ* flow visualization, is used to explore fundamentally the transport of liquid-water inside the GDLs used in PEMFC. Studies of the water evolution, water saturation, and breakthrough pressure inside a GDL with single and multiple injection points under land and channel geometries are explored. The model and experiment demonstrate good agreement between geometries of GDLs provided in this study which were obtained by a three-dimensional, reconstructed micro-structure from micro X-ray CT. The overall predictions of water evolution within the GDL agree well with the data visualized from the X-ray CT experiment for all cases studied. It also reveals that the liquid-water saturation profiles inside the GDL and breakthrough pressure are different when the location of the water injection point is altered, thereby providing analysis as to the impact of microporous layers or catalyst-layer functioning. Moreover, the uncompressed GDL undergoes a significantly different mechanism of water transport than that of the compressed GDL. Furthermore, the predictions show that the wettability variation is one of the key factors of the saturation characteristics.

In this study, CFD with LBM is used to extend the model to study the geometrical land and channel effects on the liquid-water distribution in a GDL. In addition, both modeling and data used multiple injection locations so as to understand better the impact of microporous layers and in-plane liquid flow in GDLs, which are more representative of actual PEMFC operation. The model is validated against the 3-D X-ray CT images, where the dry GDLs are also taken as input geometries for the computational model. As mentioned above, LBM is suitable for complex geometries, including microscopic simulations. The main objective of this study is to predict the liquid-water progression through a GDL at different injection pressures under locations. There are four cases of interest in this study as shown in Fig. 4.1. Case 1 is an uncompressed GDL with single injection hole under the channel as shown in Fig. 4.1a. Case 2 is similar, but with a compressed GDL, as shown in Fig. 4.1b to elucidate the impacts of compression. Figure 4.1c presents Case 3 of this work, which is a compressed GDL having two injection points under the channel. Case 4 is also a compressed GDL with two injection points, but where one is under the land and the other under the channel, as shown in Fig. 4.1d. A comparison and analysis of numerical predictions with in-situ experimental data is reported and discussed. The overall results of this study contribute to a fundamental understanding of water transport in GDLs using a combination of CFD-LBM modeling and experimental visualizations of GDL morphology and water distribution.

4.2 MICRO X-RAY COMPUTED TOMOGRAPHY

The experimental setup was a custom apparatus as described in Zenyuk et al. 2015 and depicted in Fig. 4.2. The experimental data was collected using the Advanced Light Source (ALS) Beamline 8.3.2 at Lawrence Berkeley National Laboratory (LBNL).

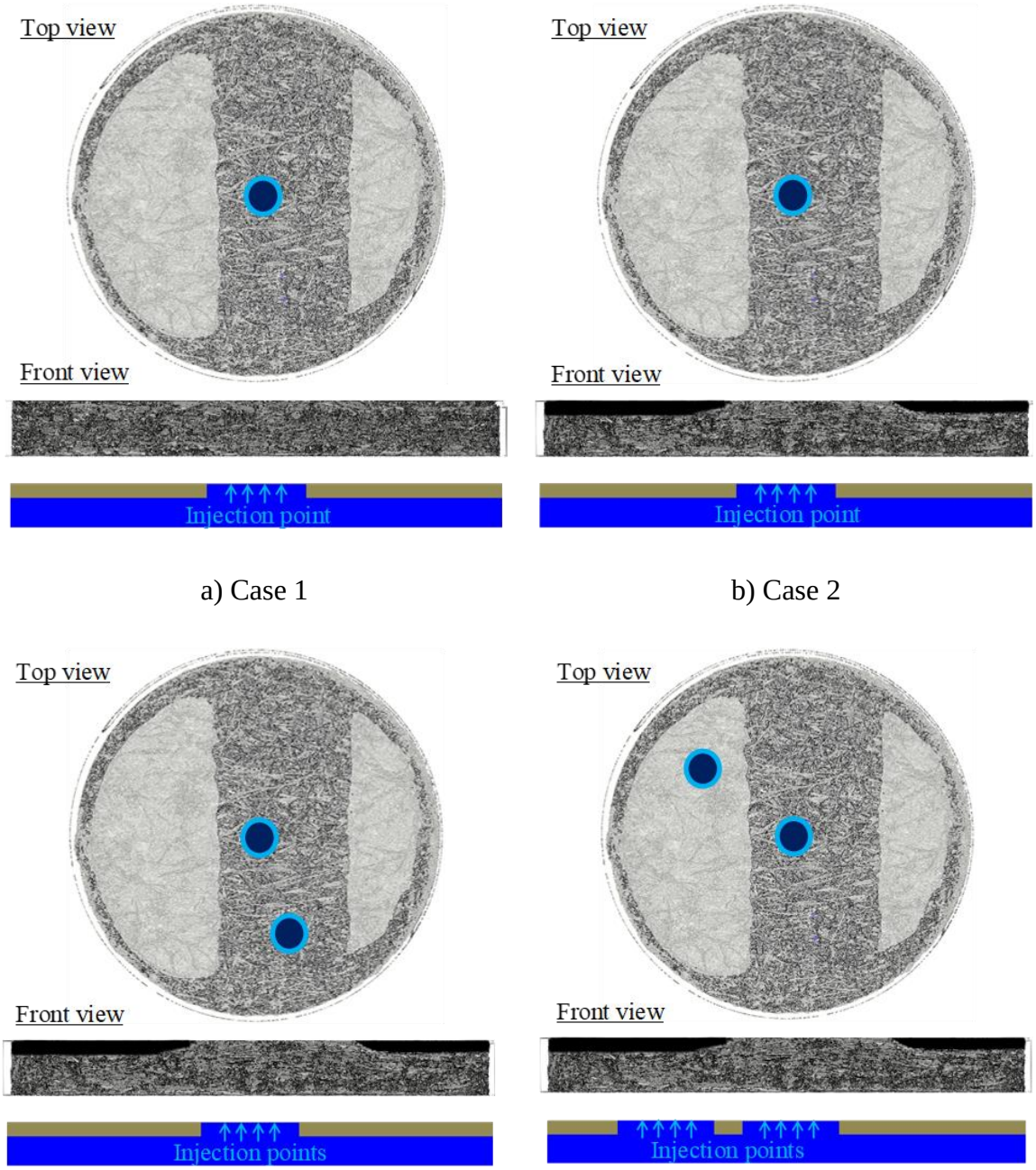

a) Case 1

b) Case 2

c) Case 3

d) Case 4

Figure 4.1 The four experimental and numerical procedures used in this study: a) Case 1, Uncompressed GDL with single injection hole under channel, b) Case 2, Compressed GDL with single injection hole under channel, c) Case 3, Compressed GDL with two injection holes under channel, and d) Case 4, Compressed GDL with first injection hole under channel, and second injection hole under land.

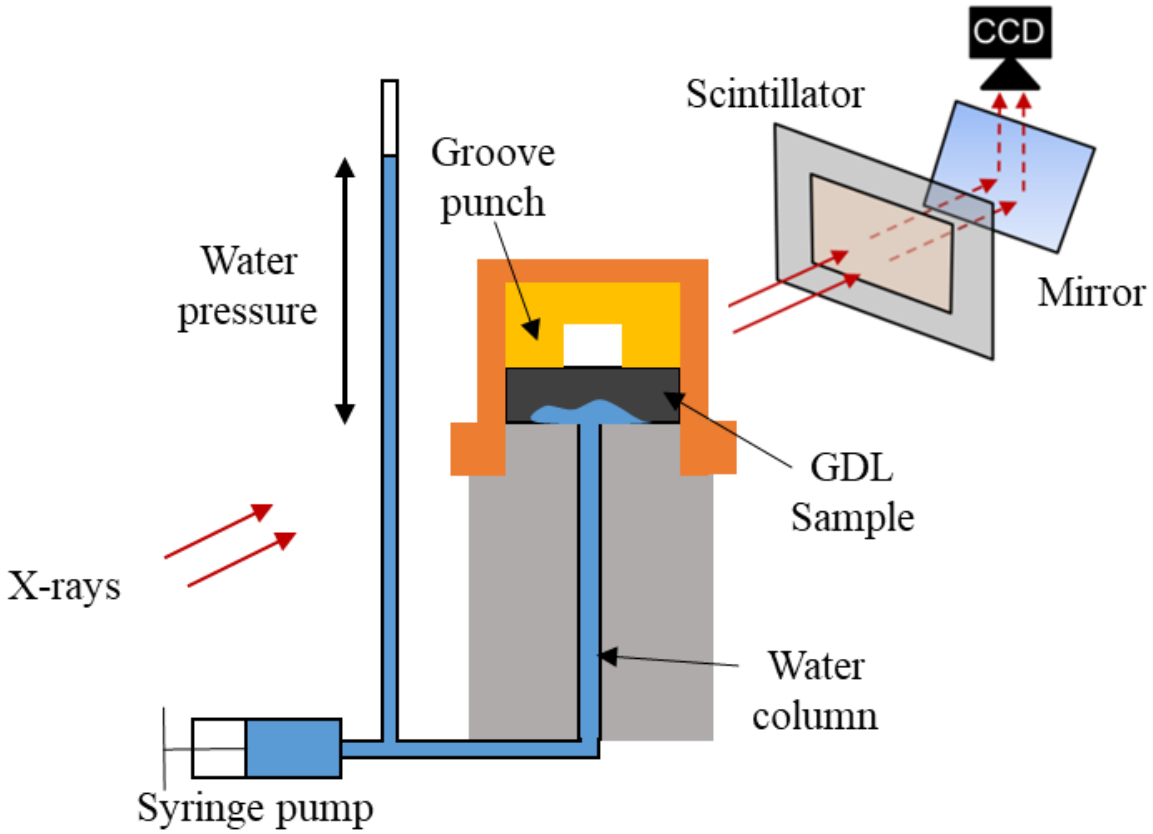

Figure 4.2 Experimental apparatus used to evaluate liquid-water saturation and capture experimental data.

X-ray scans were performed at 14 keV, 1,025 projections, and exposure time of 500 ms. This resulted in a square field of view of 3.3 mm with a resolution of 1.33 μm. At the bottom was an aluminum stage with a hollow column and holes at the top so that water could be injected into the sample. Furthermore, a hydrophobic membrane was placed on the top of the aluminum stage with a one or two holes at different locations to simulate single and double injection sites. The capillary pressure in the sample was controlled via the height of the water column. The samples were circular pieces of SGL10BA (SGL CARBON GmbH - Fuel Cell Components, Meitingen, Germany); each with a diameter of 3.2 mm and a thickness of 400 μm. The sample was placed over the holes at the top of the stage. To emulate the land/channel effects of an actual PEMFC, a stamp with a 1 mm groove was placed on top of the sample. A Kapton cap was then used to cover and maintain the alignment of the top of the stage, the sample, and the stamp. For each sample, a reference scan of the dry state, followed by scans of the sample at various capillary pressures, was acquired.

4.3 IMAGE PROCESSING

Pre- and post-processing of data was done using Fiji (Schneider et al. 2012) while the reconstruction step was conducted using Octopus 8.5 (Groso et al. 2006). In post-processing, all image stacks were first converted from 32-bit grayscale to 8-bit grayscale and then thresholded using the Otsu algorithm (thus isolating the pore phase). For each sample, the dry stack was then subtracted from each of the wet stacks (thus isolating the solid and water phases). To remove noise (primarily the remaining solid phase) from the water phase stacks, Fiji's 2D binary operation "Open" was used with 12 iterations and a neighbor count of 4. A single Open iteration consists of a single iteration of the erosion

operation followed by a single iteration of the dilation operation. The “Iso-surface” operation from the BoneJ (Doube et al. 2010) plugin was used to generate STL files from the solid and water phase stacks. A value of 4 was used for resampling for the iso-surface.

4.4 LIQUID WATER SATURATION MEASUREMENT

The liquid-water saturation was measured in a GDL domain, as shown in Fig. 4.3. The GDL images and liquid-water saturation were obtained from micro X-ray CT. GDL sample SGL10BA (carbon paper material) was used with a diameter of 3.20 mm, an average thickness of 400 μm, a reported uncompressed porosity of 0.88, and a PTFE loading of 5%. For the compressed GDL, the average thickness in this study was 290 μm with a compression pressure of 1.25 MPa at 27.5% compression (interpolated). In this experimental setup, the GDL was sandwiched between two aluminum plates. A grooved 1 mm punch was used to mimic the PEMFC land/channel geometry. Water was injected into the GDL through the bottom plate via uniformly drilled holes of 0.25 mm diameter. The water injection pressure was controlled by a syringe pump and water column. After initial testing of a wide range of injection pressures, the water injection pressure for the GDL liquid-water saturation studies was varied from 500 Pa to the breakthrough pressure.

To calculate the liquid-water saturation profiles, the GDL domain was created in a rectangular shape with the size of 2,400 x 2,400 μm, and the thickness was varied by the samples. The axis origin was located at the bottom left corner, as shown in Fig. 4.3. A MATLAB program was used to obtain the liquid-water saturation profiles for these experiments, which were calculated from the steady-state average intraporous liquid volume fractions within each plane (x-z plane) for 1,000 planes along the y-direction and subsequently plotted along the x-dimension.

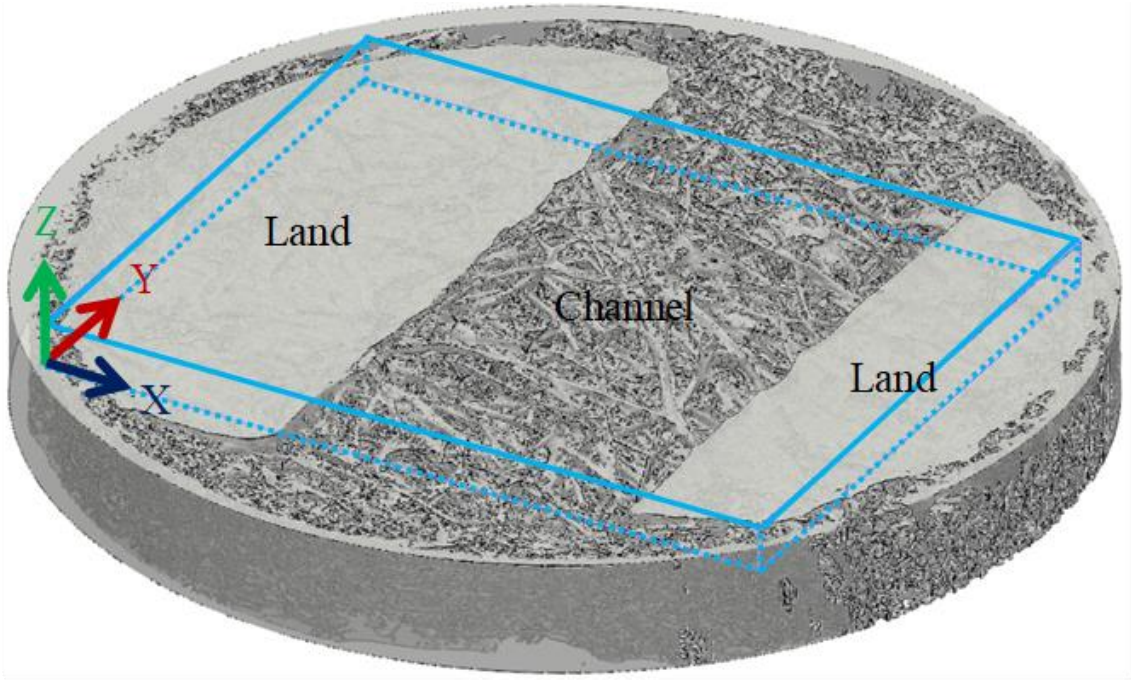

Figure 4.3 The micro-structure of GDL sample SGL 10BA from micro X-ray Computed Tomography with the rectangular fluid domain and the coordinate axis x, y, and z.

4.5 WATER PROGRESSION THROUGH UNCOMPRESSED GDL (CASE 1)

Figure 4.4 compares CFD predictions with experimental results of liquid-water saturation, defined as the total volume of liquid-water divided by total volume of pores, in an uncompressed GDL with a single injection hole in the bottom center (Case 1). In this study, the injection pressure was varied at 1,000, 1,500, 1,750, and 2,000 Pa., and the GDL contact angle in the simulation was fixed at 130°. The results show that the height of the liquid phase increases with pressure and the liquid-water fills the larger pores under the channel domain. The breakthrough pressure for this sample is around 2,000 Pa, and it is shown to have a porosity of 0.75. Figure 4.4a shows the lateral spread of liquid-water at the interface between the GDL and injection plate due to the wide interfacial gap, a result of the lack of compression. The amount of liquid-water under the channel is higher than under the land domain. This is because the injection is located under the channel, which causes the water to easily move through the pores under the channel rather than under the lands. Thus, the pressure under the channel is lower. Such an arrangement could be representative of a poorly compressed PEMFC or perhaps one with a very hydrophilic catalyst layer or a gap due to material degradation or under high current where the channel region is more active. The experimental liquid-water saturation profiles recorded at different inlet pressures are given in Fig. 4.4c. This graph shows liquid-water saturation versus the length of the GDL sample in the x-direction for pressures from 1,000 to 2,000 Pa. Again, these liquid saturation profiles at steady state were determined by calculating the average volume fraction of liquid in the in-plane (x-z planes) along the through-plane of y-direction and plotting the averages along x. Note that the porosity profile of the GDL sample was calculated before water was injected.

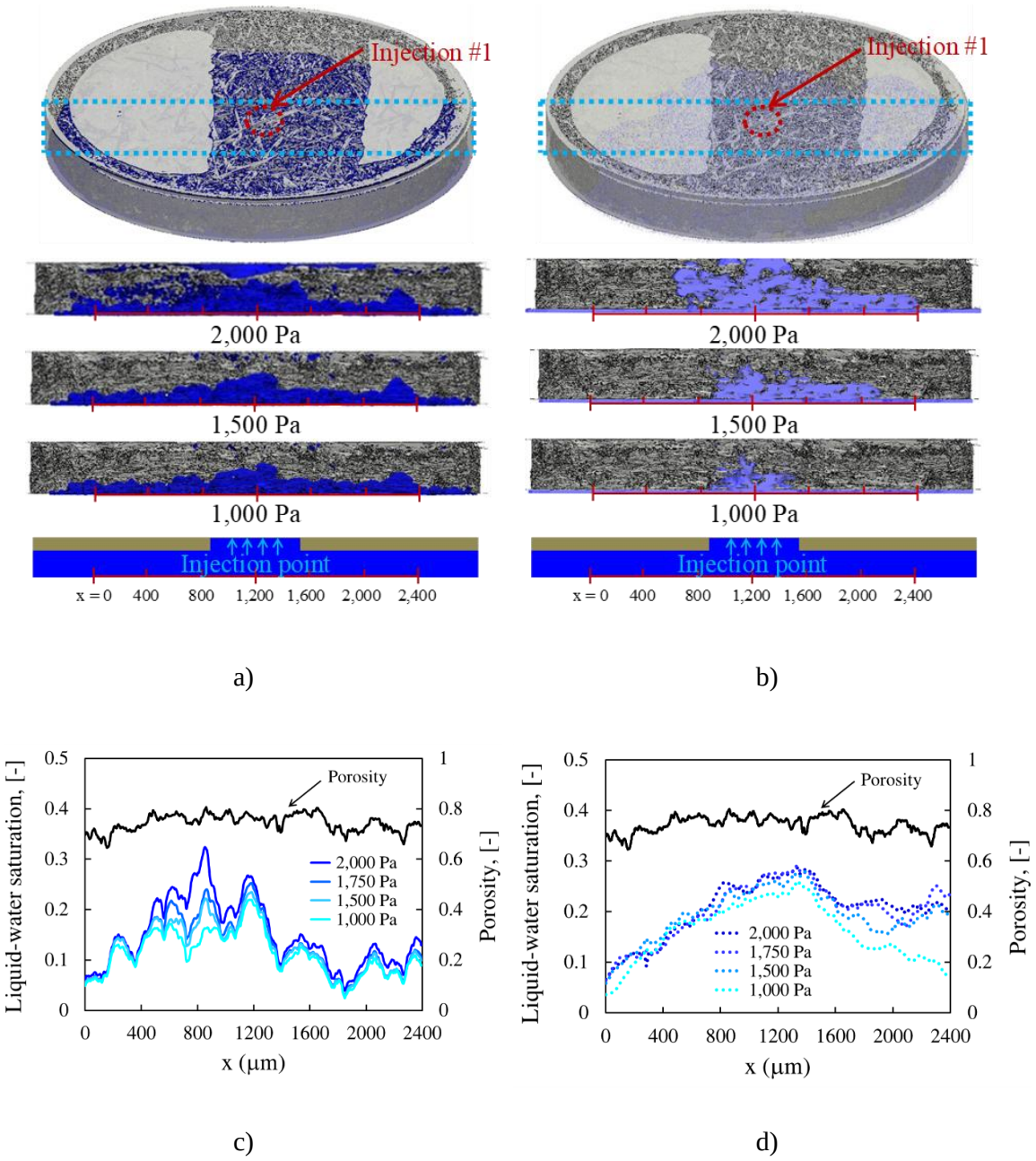

Figure 4.4 Experimental and simulated liquid-water saturation inside the uncompressed GDL with single injection hole in bottom center under channel. a) Cross sectional volume of liquid phase of experimental with the pressure of 1,000, 1,500, and 2,000 Pa, b) Cross sectional volume of liquid phase of CFD simulation with the pressure of 1,000, 1,500, and 2,000 Pa, c) Experimental liquid-water saturation profiles, and d) Simulated liquid-water saturation profiles.

According to the graph, the saturation reaches a maximum of about 25% at the middle left of the channel domain and 10% in the land domain. The plot also shows that the liquid-water saturation is a function of pressure as higher liquid-water saturation levels are observed for higher injection pressures.

In the CFD simulation, the gap between the GDL and injection plate was set at 3 μm to mimic experimental conditions. Figure 4.4b presents the simulated cross-sectional liquid-water progression through the GDL. When liquid-water is first injected, it spreads across the interfacial gap before advancing toward larger pores within the GDL. The shape of liquid-water differs from that of the experiment, and liquid-water growth remains highest beneath the channel domain. Although there is space under the sample, the volume of liquid-water in this area is still less than that observed because the roughness of the GDL interface creates non-uniformity in the interfacial gap size. The predictions confirm that most liquid-water occupies the pores under the channel.

The maximum saturation is about 30% at the middle of channel domain, which exceeds the experimental value. However, the gap beneath the uncompressed GDL affects the CFD model validation. The gap size is unknown and affects the amount of liquid-water under the uncompressed GDL before progression through the GDL begins. Therefore, the GDL should be compressed just enough to eliminate the interfacial gap and prevent the accumulation of excess liquid-water under the sample.

4.6 WATER PROGRESSION THROUGH COMPRESSED GDL WITH SINGLE INJECTION HOLE UNDER CHANNEL (CASE 2)

To explore a more representative PEMFC case, 27.5% compression is applied to the sample. After compression, the porosity of the sample is reduced from 0.75 to 0.70. The comparison between experiments and CFD simulations of water saturation in the

compressed GDL with a single injection hole in the bottom center (under the channel) at injection pressures of 500, 1,000, 2,000, 2,500, and 3,000 Pa is shown in Fig. 4.6. The observations from X-ray CT show that the manner of liquid-water progression in this case is similar to that of Case 1. The results also reveal the absence of excess liquid-water inside the gap area, as shown in Figs. 4.6a and 4.6b. There is significant liquid-water saturation under the channel area due to the higher GDL porosity under the channel and the position of the injection. It can be clearly seen that compression leads to a decrease of the liquid-water saturation in the entire GDL gap between the GDL and injection plate. This is due not only to a decrease in the gap itself but also to a decrease in pore-size (see Fig. 4.5). This decrease in pore size increases the lateral transport resistance. Furthermore, there is good agreement between the CFD simulations and experiments. The experimental data reported by Garcia-Salaberri et al. 2015 are inconsistent with this study, Case 2. For example, the larger liquid-water saturation profiles in those experiments, which is caused by the open channel at the top of sample holder and larger injector diameter (diameter of 1.50 mm vs. 0.25 mm). Even though the experiments conducted here were close to their experiments, our experimental design can study the effect of geometrical lands/channel and the effect of multiple injection points. Note that they used the different GDL sample (Toray TGP-H-120), which also indicates some of different behavior between our work and their work. From Figs. 4.6a and 4.6b, the liquid-water saturation profiles in the GDL along the length (x-direction) can be observed to quantify and validate the liquid-water saturation distributions.

Figures 4.6c and 4.6d present the comparison of experiments and CFD simulations of liquid-water saturation profiles under the compressed GDL with a single injection hole.

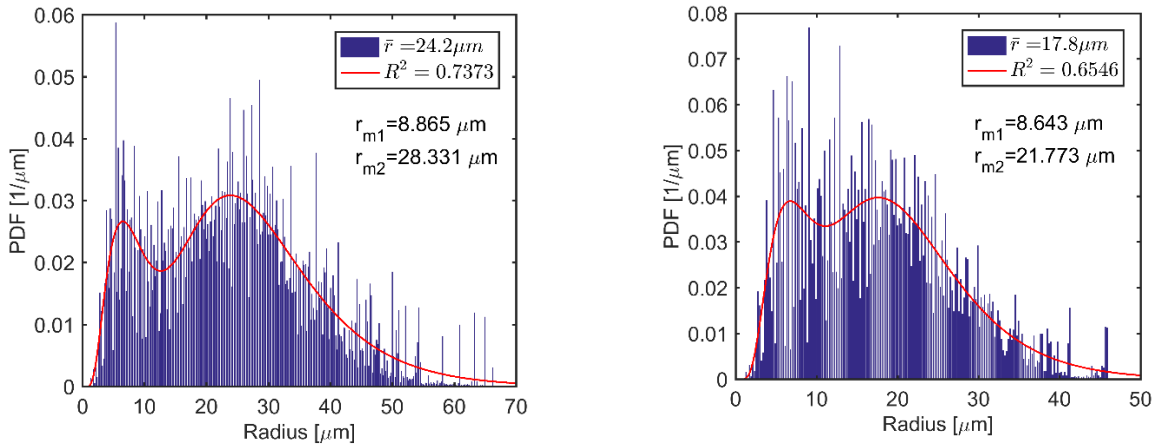

Figure 4.5 The pore-size distributions (or probability density functions (PDFs)) for Case 1 (left) and Case 2 (right). The bimodal fits are shown and the two peak radii of the PDFs are reported. The mean radius of each distribution is shown as well.

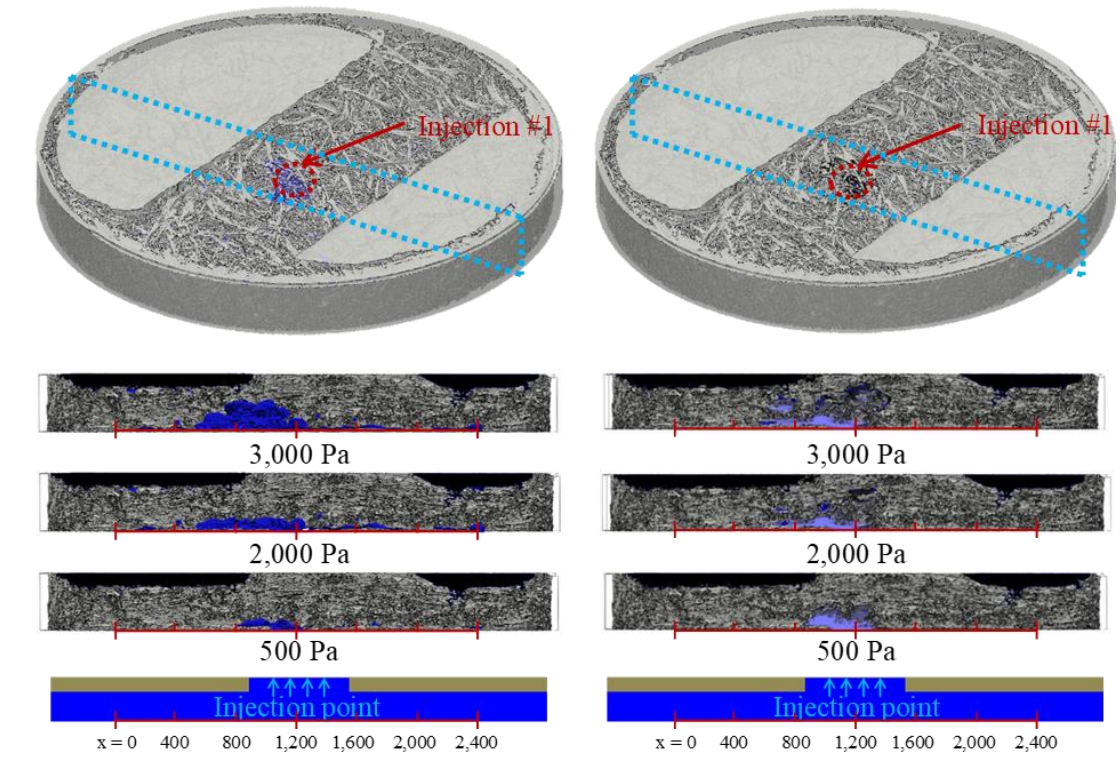

a) b)

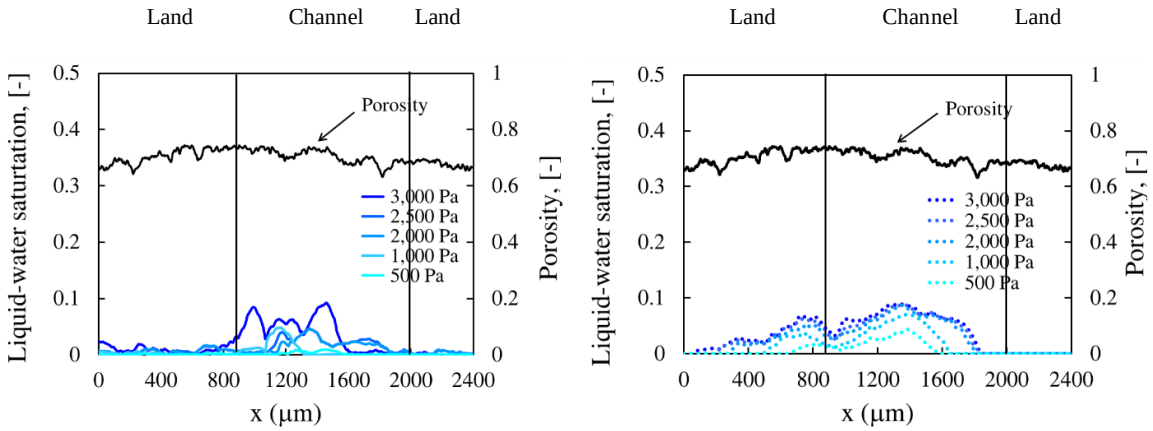

c) d)

Figure 4.6 Experimental and simulated liquid-water saturation inside the compressed GDL with single injection hole in bottom center under channel. a) Cross sectional volume of liquid phase of experimental with the pressure of 500, 2,000, and 3,000 Pa, b) Cross sectional volume of liquid phase of CFD simulation with the pressure of 500, 2,000, and 3,000 Pa, c) Experimental liquid-water saturation profiles, and d) Simulated liquid-water saturation profiles.

The liquid-water saturation profiles confirm the higher accumulation of liquid-water under the channel than under the lands. The experimental saturation profiles show that the total volume fraction of liquid-water reaches a maximum of about 10% under the channel domain and less than 2% under the land domain, as shown in Fig. 4.6c. The model predictions of water evolution show the similarity of the shape of liquid-water as experiment, especially when the pressure is below 1,000 Pa, as shown in Fig. 4.6. For this case, the compressed GDL structure diminishes the liquid-saturation profiles and increases the breakthrough pressure because it is more difficult for liquid-water to move through the restricted pores. With this approach, the breakthrough pressure has been increased from 2,000 to 3,000 Pa. Although the breakthrough pressure is increased, the narrowing of the dominant water pathways and lower overall saturation should result in better PEMFC performance, which was demonstrated recently in similar findings of GDLs with porosity variations (Steinbach et al. 2018). Furthermore, the liquid-water saturation far from the injection almost vanishes as the GDL becomes less porous (because there is no longer an interfacial gap) and lateral transport resistance increases (because of decreasing pore-size (see Fig. 4.5)). So, the compressed sample is better than the uncompressed where the water is a layer and takes the transport pathways under the channel.

Figure 4.5 shows pore-size distributions (or probability density functions (PDFs)) for both Case 1 (left) for uncompressed sample and Case 2 (right) for compressed sample. Case 1 shows peak radii that are 8.9 μm and 28.3 μm, whereas Case 2 shows a similar smaller peak radius of 8.6 μm but a smaller larger peak radius of 21.8 μm. Upon compression, larger voids decrease in size; thus also affecting water transport properties

within the GDL. It is noted that when we crop the samples further (to exclude the space under the sample), the pore-size distribution shifts to smaller radii for Case 2.

4.7 WATER PROGRESSION THROUGH COMPRESSED GDL WITH TWO INJECTION HOLES (CASE 3 AND 4)

To explore the lateral movement of water in the GDL and the influence of multiple injection sites, which may occur as one goes from a GDL to a GDL with a microporous layer perhaps, the next studies utilized two injection holes with one under the channel and the other either under the channel (Case 3) or under the land (Case 4). For Case 3, the liquid-saturation profiles are shown in Figs. 4.7c and 4.7d. The experimental data and computational prediction both reveal the similarity of the shape and location of the liquid-water saturation. When the injections start to feed the liquid-water, the liquid-water begins to flow up from the two injections and percolates vertically above injection locations until breakthrough (3,000 Pa) is reached, as shown in Figs. 4.7a and 4.7b. Interestingly, they do not strongly influence each other at this distance of 800 μm. This then demonstrates that even though the GDL is anisotropic with higher in-plane permeability, the dominant flow pathway is still straight through. Such a finding agrees with previous analysis of the impact of multiple versus single injection, albeit in ex-situ setup without visualization capabilities, where the multiple sites were hypothesized to mainly interact at the injection side and not within the GDL (Quesnel et al. 2015).

Figures 4.7c and 4.7d compare experiments and CFD simulations of liquid-water saturation at steady state for varied pressures at 500, 1,000, 1,500, 2,000, 2,500, 3,000 Pa. The overall prediction of liquid-water saturation profiles is similar to the experimental data. However, the amount of liquid-water saturation from predictions are higher than the experimental data at x-coordinates from 400 to 800 μm.

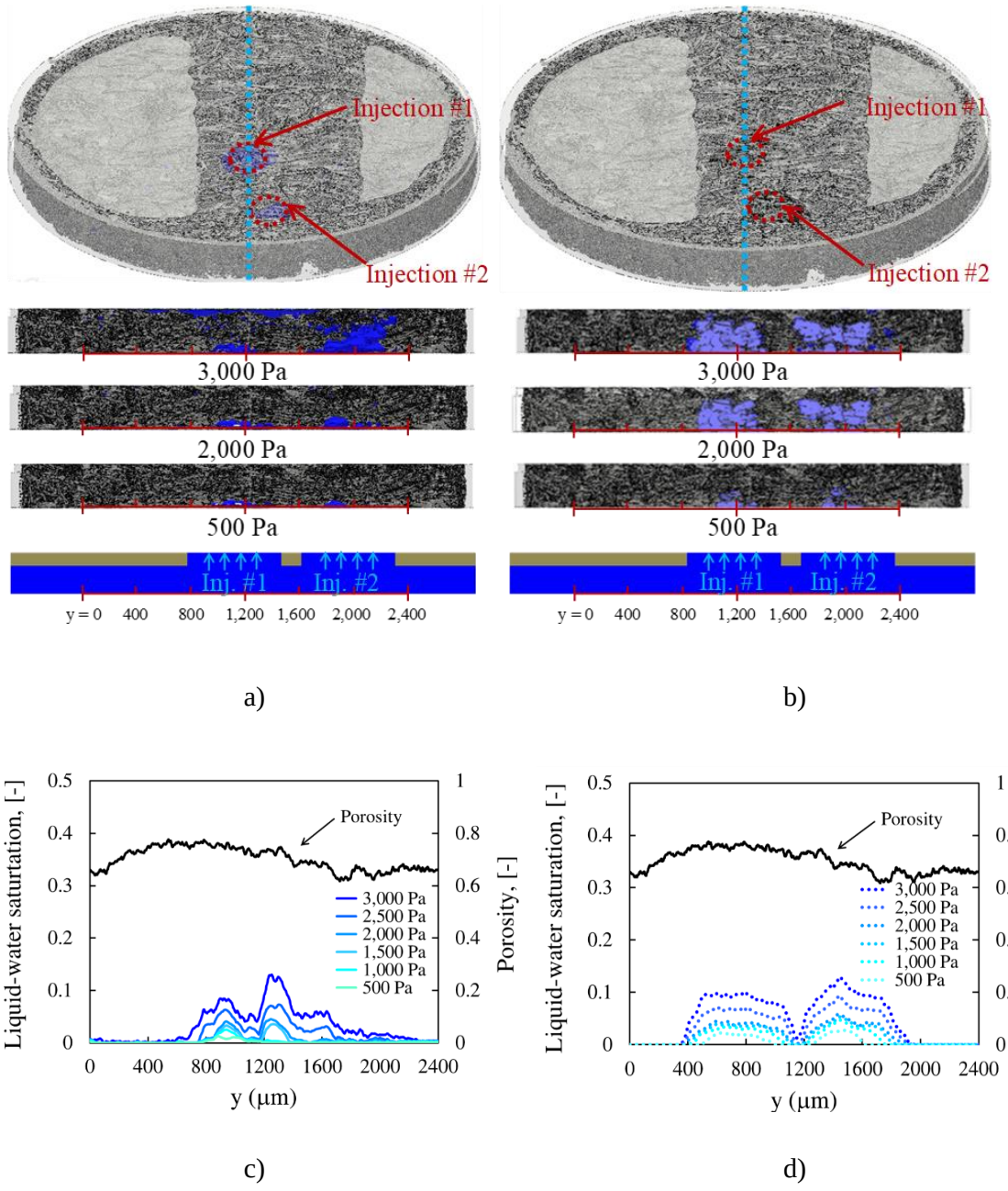

Figure 4.7 Experimental and simulated liquid-water saturation inside the compressed GDL with two injection holes in bottom under channel a) Cross sectional volume of liquid phase of experimental with the pressure of 500, 2,000, and 3,000 Pa, b) Cross sectional volume of liquid phase of CFD simulation with the pressure of 500, 2,000, and 3,000 Pa, c) Experimental liquid-water saturation profiles, and d) Simulated liquid-water saturation profiles.

According to the porosity profile, the porosity in this area is higher and simulations suggest that water can percolate easily in this region. Furthermore, the results show the relationship between liquid-water saturation and porosity of the dry sample. When the porosity is decreased in the areas through which water flows, it is more difficult to push the water through, as higher pressure is required. Thus, with the same pressure, higher porosity results in more liquid-water saturation. For example, in this case, the liquid-water saturation profiles show slightly reduced progression at x-coordinates beyond 1,800 μm due to the lower porosity (porosity reduced to 0.6), which results in difficulty percolating liquid-water.

Similar to Case 3, Case 4 explores two injection sites but where one is under the land. Again, this could be indicative of a GDL with a microporous layer that provides selective injection sites. Note that the diameter of the second injection is half that of the first injection. The GDL was compressed to a thickness of 290 μm. Figures 4.8a and 4.8b present the comparison between experimental data and CFD simulations at pressures of 500, 2,000, and 4,000 Pa. The cross-section that represents the planes is used to measure the liquid-water saturation profiles from experiments and CFD simulations. The visual observation reveals that the liquid-water emerges under the land area first and does not fully progress through the GDL. This is because the porosity of the GDL under the land area is reduced due to compression and it is possible that there is a small tendril that goes to the top of the land and then feeds back to the channel. It also has the effect of capillary action in the narrow spaces of channel and the size of the injection holes. Upon increasing pressure, the liquid-water fills pores under the channel area until breakthrough occurs (about 4,000 Pa).

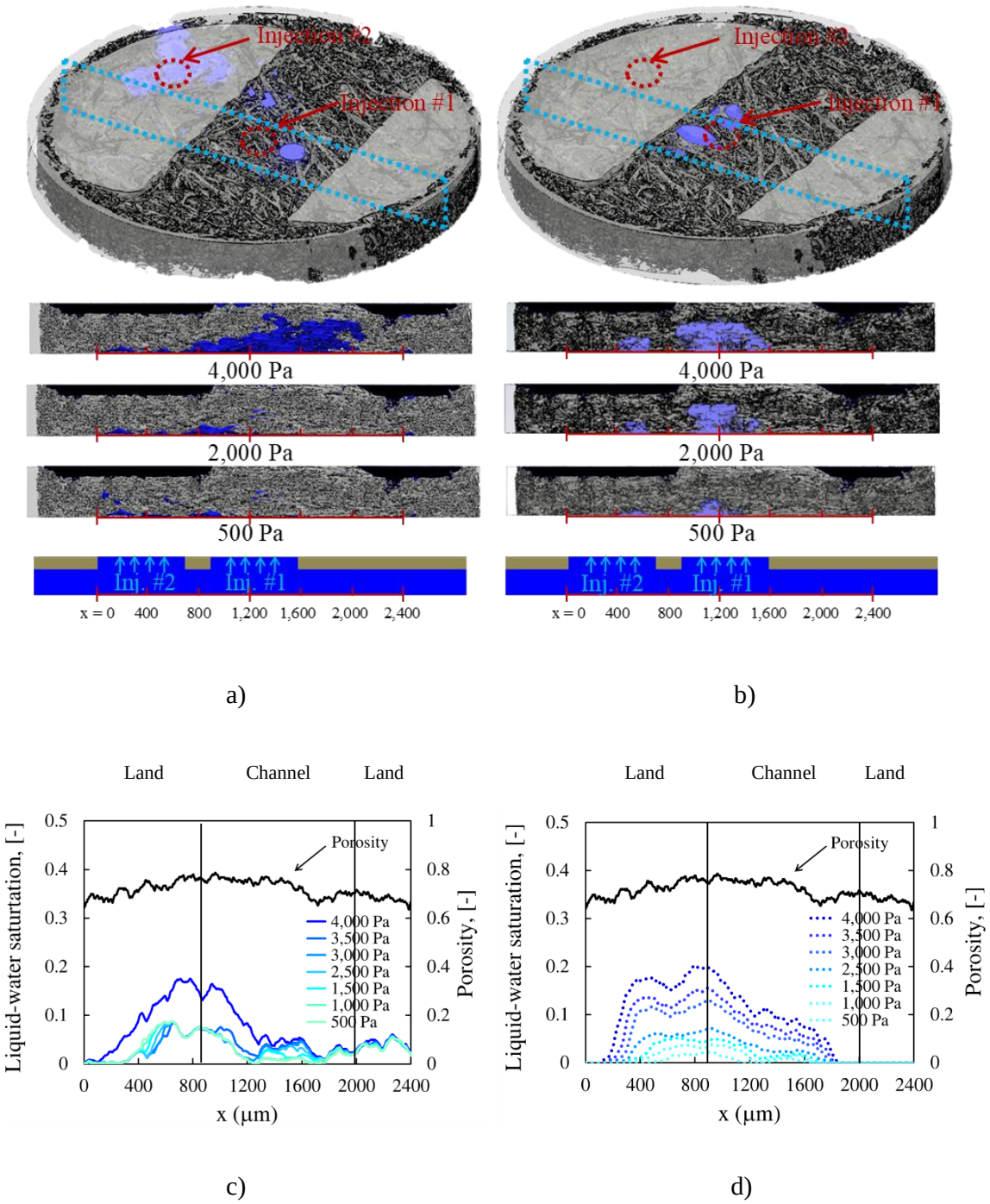

Figure 4.8 Experimental and simulated liquid-water saturation inside the compressed GDL with one injection point under channel, and second injection point under land. a) Cross sectional volume of liquid phase of experimental with the pressure of 500, 2,000, and 4,000 Pa, b) Cross sectional volume of liquid phase of CFD simulation with the pressure of 500, 2,000, and 4,000 Pa, c) Experimental liquid-water saturation profiles, and d) Simulated liquid-water saturation profiles.

Figures 4.8c and 4.8d present the comparison of experiments and CFD simulations of liquid-water saturation profiles with pressures varied from 500 to 4,000 Pa. The experimental and simulated saturation profiles are comparable at all pressures. The saturated region becomes wider in the area between the channel and land domains at x-coordinates from 300 to 1,800 μm, thereby filling more of the pore space. A significant liquid-water saturation can be found at pressures greater than 3,500 Pa. A large amount of water accumulates in the high-porosity area between land and channel from 400 to 1,200 μm in the x-direction; the liquid-water saturation reaches about 20% in this area. Usually, in this area, the liquid-water flows easily. For pressures less than 3,500 Pa, the liquid-water saturation reaches about 10% in the channel domain and 5% under the lands. The results also reveal a liquid connection through the entire length of the sample, allowing for water transport between two injectors. This differs from the previous case (Case 3) in which they do not influence each other reciprocally. The liquid-water transport between the injection holes is influenced by intermolecular forces and the hydrophilicity of surrounding GDL surfaces. This is because of the high porosity in this area and the location of one of the injectors in the land domain. Again, the water can move easily across the GDL via the higher-porosity pathways under the channel. So, when the liquid-water is flowing under the GDL at land-channel domain edges, liquid-water can percolate into the channel domain easily, which results in water transference between the two injection holes.

4.8 ERROR ANALYSIS

The error associated with the CFD simulation and experimental data was examined using statistics. The percent error indicates the degree of random fluctuations, which is reported in Table 4.1.

Table 4.1 Percentage error between CFD simulation and experimental data.

Case 1		**Case 2**		**Case 3**		**Case 4**	
Pressure [Pa]	**Error [%]**	**Pressure [Pa]**	**Error [%]**	**Pressure [Pa]**	**Error [%]**	**Pressure [Pa]**	**Error [%]**
1,000	29.67	1,000	36.20	1,000	38.01	1,000	36.98
1,500	36.51	2,000	26.30	1,500	34.75	1,500	33.22
1,750	36.08	2,500	27.58	2,000	23.56	2,000	29.54
2,000	26.99	3,000	3.04	2,500	22.42	2,500	20.06
				3,000	8.48	3,000	21.91
						3,500	20.94
						4,000	6.21

The percent error was calculated as the difference between two plots at each voxel in the computed domain, and take the average over all elements. The results from the CFD simulation have relatively low percent error of liquid water saturation at high pressure, especially at or beyond the breakthrough pressure, because deviations remain constant despite the increased magnitude of saturation. Furthermore, the error between experimental data and CFD simulations could also be due to the non-uniform wettability in the GDL sample, which led to the substantial difference of liquid water distribution and its saturation in some locations. Even though the error is higher at low pressure, the CFD simulation can provide a possible distribution pattern and transport pathway of the liquid water progression through the GDL sample.

4.9 QUANTITATIVE ANALYSIS OF THE EFFECT OF POROSITY ON LIQUID WATER SATURATION

Figure 4.9 presents the quantile-quantile (Q-Q) plots of experimental data to confirm the correlation between porosity and liquid saturation. There are 1,800 randomized positions for each case which are used to analyze and report the quantitative data of pore space where liquid-water saturation is occupied. The overall profiles confirm that there is a strong relation between porosity and liquid saturation. At the same pressure of water injection, the liquid-water saturation is greater in the location where the porosity is higher. When the water pressure is increased, the overall water saturation also increases. For an uncompressed GDL (Case 1), the results indicate significant higher liquid-water saturation compared to other cases under compressed GDL (Cases 2 to 4). This is because more water can enter to the GDL through a wide interfacial gap as explained earlier. Cases 2 and 3 show the comparison of the profiles between one and two injection locations. Note that both cases have the injection hole located under the channel areas.

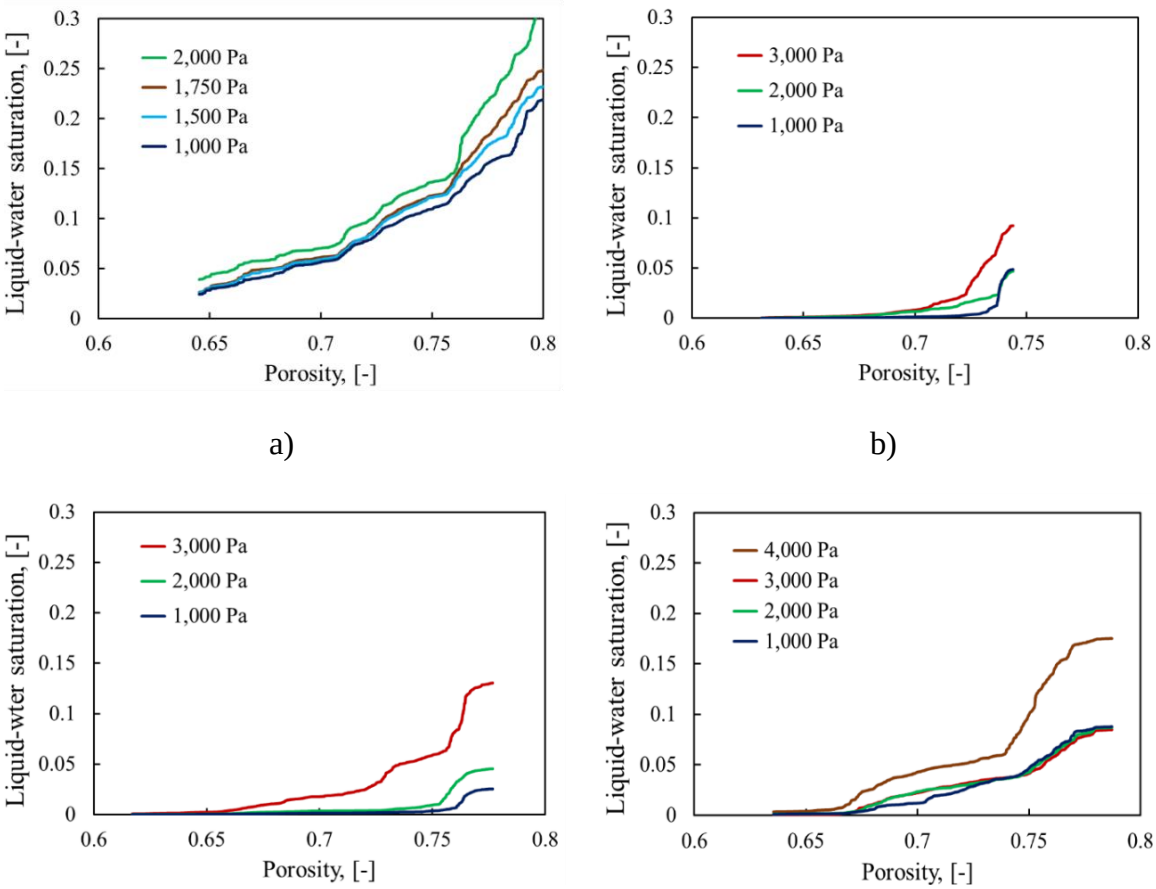

Figure 4.9 Quantile-quantile (Q-Q) plots of liquid water saturation with the porosity presented of a) Case 1, b) Case 2, c) Case 3, and d) Case 4.

The profiles of liquid-water saturation against porosity in Cases 2 and 3 look alike for all injected pressure, but the values of liquid-water saturation from Case 3 are higher than Case 2. This is because the amount of liquid water injected through the GDL is larger than single injection point from Case 2.

Figure 4.9d displays the liquid-water saturation profiles against porosity at different injected pressure conditions for Case 4. In this case, there are two injection points, but one injector is located under the land area, as shown in Figure 4.1d. The liquid-water saturation profiles of this case are different than in Case 3 (two injectors under the channel). Having one injector located under the land area causes the liquid-water saturation increases in those locations where the porosity is lower ($0.74< \varepsilon < 0.67$). These profiles do not appear in Case 3 (two injection holes under the channel area) until it reaches the breakthrough pressure of around 3,000 Pa. Keep in mind Case 4 has the highest water breakthrough pressure. This is due to the impact from the liquid water as it moves through the hole under the land. The GDL does not reach the break-through pressure because the land stops it, then the water fills the voids under and around channel injection hole until a breakthrough occurs.

4.10 THE EFFECT OF WETTABILITY ON LIQUID WATER SATURATION

The wettability of carbon fibers can be controlled by degree of graphitization and surface treatments during the manufacturing process. Changes in the wettability of carbon fibers from the surface treatment can affect the liquid-water saturation and breakthrough pressure in the GDL (Nguyen et al. 2015; Weber 2010; Santamaria et al. 2014). To explore this effect, the contact angle of carbon fibers was varied at 90°, 130°, and 150° with the model. The testing condition and GDL sample from Case 3 were used for this study, as shown in Fig. 4.10. The liquid-water was fed at a pressure from 500 to 3,000 Pa.

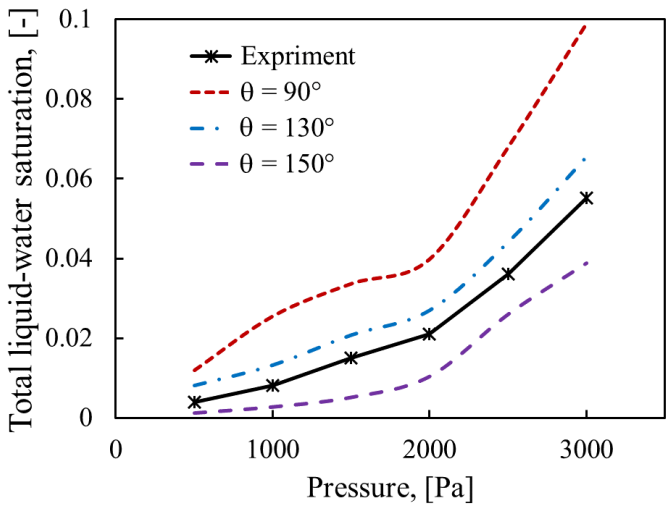

a)

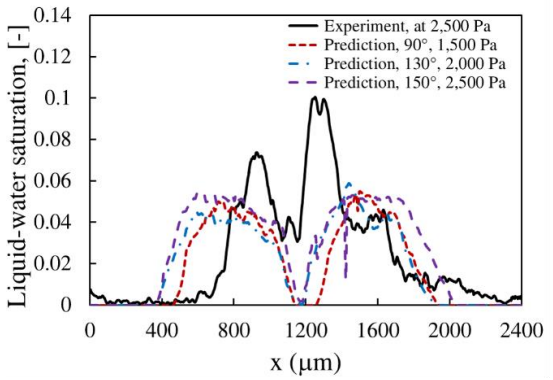

b)

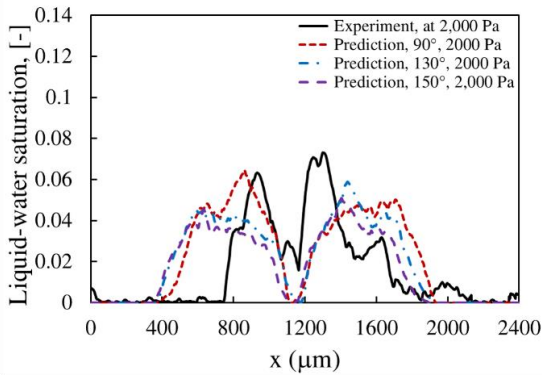

c)

Figure 4.10 The effect of wettability on liquid-water saturation comparison between experimental data and CFD simulation for SGL 10BA, a) under injection pressure from 500 to 3,000 Pa with different contact angle, b) under the constant total liquid water saturation of 0.035 with different contact angle, and c) under constant injection pressure of 2,000 Pa with different contact angle.

Figure 4.10a presents the overall liquid saturation profile against pressure at different contact angle. This figure explains how pressure could change the quantity of liquid water injected to the GDL and the wettability can control the amount of liquid water at the same pressure. The results reveal that at the same pressure, the amount of liquid saturation will increase with a decrease in the contact angle. When the pressure is increased at the same wettability, the liquid saturation increases. Figure 4.10b shows the local liquid saturation profile along the x-direction with constant total liquid saturation of around 0.035. The wettability has been varied and therefore the pressure of each contact angle will be different. The selected pressure for the contact angles of 90°, 130°, 150°, of the experiment are 1,500, 2,000, 2,500, and 2,500, respectively. The results show that the local liquid saturation profiles are not exactly the same (identical) at different wettability while the amount of liquid water inside the GDL is controlled. Moreover, the shape, also is not similar when it is compared with the profiles with the same pressure. As shown in Figure 4.10c, that is compared in the liquid saturation profile along x-direction at different wettability under the constant pressure. Figure 4.10c presents the effect of wettability at the same pressure under the breakthrough pressure (2,000 Pa), the result shows that the water percolates vertically above the injection locations and does not progress through the GDL because the pressure is insufficient for breakthrough to occur. At contact angle of 130°, both the experiment and CFD simulation illustrate the similarity of the shape and growth of the liquid phase, as shown in Figs. 4.7a and 4.7b, which is remarkable seeing as the measured contact angle also contains surface pinning and interactions. Thus, one might consider that such forces also dominate within the GDL as well. The changes in wettability on the surfaces of carbon fibers result in change of water behavior, varied shape, and

growth of water. The high-hydrophobicity case (150° contact angle) presents less water saturation than the others (90° and 130°) as more energy is needed to push the water through the GDL. With the lower wettability of solid structure (90° contact angle), the liquid saturation is higher than the other cases because the liquid-water easily moves through and fills the structure.

The benefit of this model is the change in the contact angle of GDL surface allows for the study of the effect of wettability alteration, which can help material designers work out the unsatisfactory features of the material and assist the on-going process before laboratory testing. The results also reveal that the contact angle is an important factor. For example, the increase in hydrophilicity causes the formation of a liquid film, leading to substantially less gas pathways and more lateral flow. With higher contact angles, the saturation seems to be more sensitive to the wettability since more pressure is required to push the liquid water through the GDL. In future work, we wish to verify whether CFD simulations can be confidently used to predict accurately the contact angle of the GDL if such information is unavailable. Moreover, the results from our CFD simulation can reflect to the PEMFCs performance and design optimal of GDL structure (Shimpalee et al. 2017).

4.11 SUMMARY

In this chapter, three-dimensional direct numerical simulation using the Lattice Boltzmann Method was used to explore liquid-water transport inside gas-diffusion layers used in polymer-electrolyte fuel cells. It was observed that efficient water progression across a GDL is dependent on sufficient compression in order to avoid flooding of the catalyst layer, but the land areas of the flow plate, which provide this compression, stifle transport and force lateral water movement. This presents a problem for the design of fuel

cell flow plates that can be handled with CFD simulations. A model was validated by comparison to in-situ experimental data involving multiple injection points during X-ray tomography. The liquid-water saturation can be calculated from this visualization and it agreed well with the simulations. The motion of liquid-water saturation in the pore structure was predicted using the geometry taken by micro X-Ray CT. The local saturation of liquid-water inside the GDL samples varies with the change of injection locations, including under land and channel, because the pore space, shape, and size of porous materials used in PEMFCs are variable and irregular for uncompressed and compressed samples. The results reveal the correlation between liquid-water saturation and porosity for the compressed sample, resulting in lateral transport pathways. The similarities between simulated water saturation profiles and experimental data strongly suggests that the LBM technique can be utilized in enhancing our fundamental understanding of the transport of liquid-water and air inside the gas diffusion layers used in PEMFCs.

CHAPTER 5

MULTI-SCALE MODELING OF PEMFC USING LBAM

5.1 INTRODUCTION

This chapter proposes the development of direct-modeling based within the multi-scalar structures of the porous media and CL to understand the electrochemical kinetics and multi-scalar/multi-physics transport. The direct modeling-based Lattice Boltzmann Agglomeration Method (LBAM) is used to explore the electrochemical kinetics and multi-scalar/multi-physics transport inside the detailed structure of the porous and catalyst layers inside polymer electrolyte membrane fuel cells (PEMFCs). The complete structure of the samples is obtained by both micro- and nano- X-ray computed tomography (CT). LBAM is able to predict the electrochemical kinetics in the nanoscale catalyst layer and investigate the electrochemical variables during cell operation. This work shows success in integrating the lattice elements into an agglomerate structure in the catalyst layer. The predictions of LBAM were compared with a macro-kinetics model and experimental data. The overall predictions reveal that the local saturation of liquid water, distributions of electrochemical variables, and mass fraction across the samples can be controlled by the regulation of operating conditions. LBAM is a highly effective method of predicting the partial flooding issue, understanding the transport resistance, and investigating transport inside the porous transport layer that affects the overall cell performance in the PEMFC. The outcome of this work will be used for the optimization of porous structure design, durability, and water management improvement, for novel porous materials, particularly in the catalyst layer.

In this study, the porous media consist of GDL, micro porous layer (MPL), and CL, as shown in Fig. 1.2 The GDL sample used in this study is SGL 25BC, the CL sample is Ion Power, and the membrane is similar type to Nafion^{TM} 211. The model geometries of porous and CL provided in this study will be obtained by a 3D, reconstructed microstructure from both micro- and nano- X-ray computed tomography (CT). The complex detailed structure of the porous layers and the CL model is in the micro- and nano-scale. The voxel sizes of the micro- and nano- X-ray CT are 1.33 and 0.024 micrometers, respectively. The CFD simulation with the Lattice Boltzmann Method (LBM) particles-based approach will be used to solve for the mass transport in the porous and catalyst layers. The combination of LBM and Agglomerate model, Lattice Boltzmann Agglomeration Method (LBAM), is used to simulate the electrochemical kinetics in the CL. The lattice elements are determined as an agglomerate of carbon support (Cs), Platinum (Pt), and Ionomer, as shown in Fig. 1.2. Through this method, the agglomerates in the CL are able to apply the kinetic expression and solve the electrochemical variables such as overpotential and current density. The studies will include a prediction and explanation of water evolution, water saturation, heat transfer, species transport, and electrochemical kinetics inside porous and catalyst layers used in PEMFC.

5.2 EXAMINING THE LBAM MODELING TECHNIQUE

The first model under examination is simulated to test the possibility of the LBAM technique and comparison between two kinetic models, as mentioned above. Figure 5.1 shows the prediction of temperature, O_2 mass fraction, water vapor mass fraction, and liquid-water saturation in the computational domain (SGL 25BC with the CL) obtained from the LBAM. The initial temperature for the entire geometry is set at 70 °C (343 K).

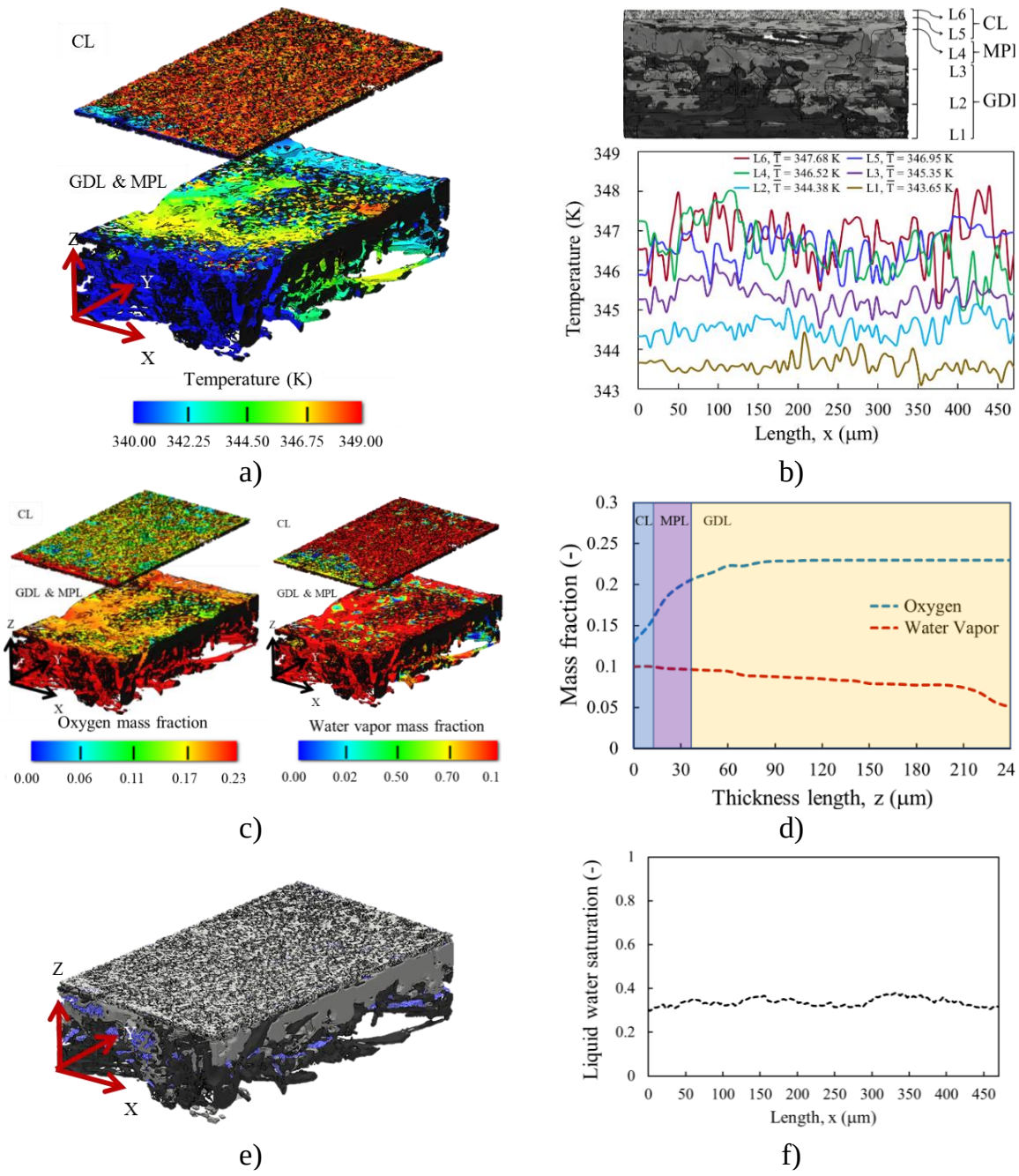

Figure 5.1 Prediction of temperature, oxygen mass fraction, and water saturation under sample operating condition. a) 3D visualization temperature of GDL/MPL/CL, b) Temperature profile across x-direction of sample, c) 3D visualization oxygen and water vapor mass fraction of GDL/MPL/CL, d) Oxygen and water vapor mass fraction profile along with the thickness (z-direction) of sample, e) 3D visualization liquid saturation, and f) average liquid water saturation profile across x-direction of sample.

The current density is maintained at 1 A/cm^2 at the potential of 0.675 V. The steady state temperature distribution for this sample is shown in Fig. 5.1a. This figure also presents the 3D visualization of heat transport through the carbon fiber, binder, and CL that cannot be predicted by simply using a macro-scale model. The temperature is highest at the reaction surface and it decreases throughout the MPL and GDL. The average temperature profiles across the xz-plane at several locations (L6 to L1) along the y-direction is presented in Fig. 5.1b. L6 and L5 are located within the CL, where the electrochemical reaction takes place. These locations have similar temperature distributions due to the thinness of the CL. The highest temperature is in the CL region due to the electrochemical reaction, which is exothermic. The locations within the GDL and MPL have lower temperatures because of cooling gas (i.e., O_2) that flows from the channel through the GDL and MPL.

Figure 5.1c presents the mass fraction distribution of O_2 and water vapor in the sample. The observations show that the O_2 gas is consumed and water vapor is produced by the electrochemical reaction at the CL. There is a high O_2 mass fraction gradient at the bottom of the GDL due to its proximity to the channel. Likewise, water vapor has a high mass fraction gradient in the MPL of due to water vapor generation at the CL. Figure 5.1d shows the O_2 and water vapor mass fraction profile along the thickness of the sample. The O_2 mass fraction is reduced from the bottom of the GDL towards the top of the CL, as the electrochemical reaction is taking place in the CL. Meanwhile, water, which is a byproduct of the electrochemical reaction, is generated from the CL and flows towards the bottom of the GDL. This causes the mass fraction of water vapor to increase from CL toward the GDL. Further, for this examination case, the water vapor mass fraction was high enough

that the partial pressure of water was greater than water saturation pressure. Therefore, water condensation was detected, which subsequently formed liquid water, as shown in Figure 5.1e. This liquid water came from water condensation in this operating condition, as mentioned above. This model displayed the ability to predict the liquid water saturation inside the CL and all other model geometries (i.e., GDL and MPL). The average liquid water saturation profile across the x-direction of the sample is shown in Fig. 5.1f. The contact angle of water on the GDL was set at 130 degrees. In order to obtain the average liquid water saturation profiles, the average intraporous liquid volume fractions within each xz-plane for several planes were calculated along the y-direction. The prediction shows the average liquid water saturation to be about 0.33.

Figure 5.2 shows the comparison of the macro-kinetics model and LBAM in which the average current density is maintained at 1 A/cm^2. The distributions of electrochemical variables, i.e. cathode overpotential and current density, inside the CL in the macro-kinetics model are shown in Figs. 5.2a and 5.2b. The distribution of the cathode overpotential is related to the distribution of O_2 and the water vapor mass fraction of the CL predicted in Figs. 5.1c and 5.1d, as well as the liquid water distribution in Fig. 5.1e. The predictions from the macro-kinetics model show an average cathode overpotential of 0.23 V and a current density of 1.09 A/cm^2. The cathode overpotential and current density from LBAM are shown in Figs. 5.2c and 5.2d. The results show that the distributions in the LBAM model are similar to those of the macro-kinetics model, which predicts an average cathode overpotential of 0.25 V and a current density of 0.98 A/cm^2. The overpotential from LBAM is slightly higher than the macro-kinetics model, which result in a reduced current density. The LBAM model better predicts the electrochemical kinetics parameters.

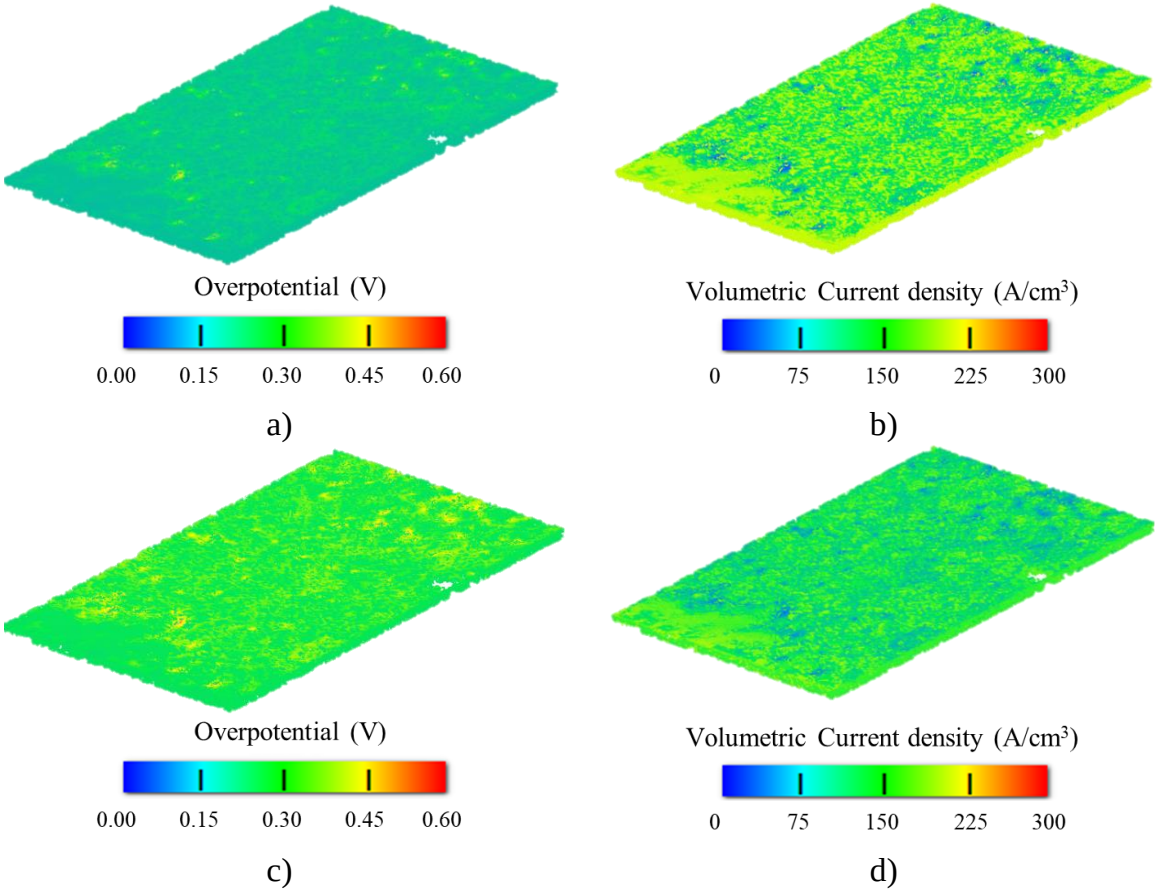

Figure 5.2 Comparison of kinetics models and predictions of the electrochemical parameters in the catalyst layer. a) Macro-kinetics model, cathode overpotential, b) Macro-kinetics model, cathode volumetric current density, c) LBAM, cathode overpotential, and d) LBAM, cathode volumetric current density.

This is because the effective reaction surface area is more accurately represented by introducing the agglomerate model of the CL in the LBAM. So, the LBAM is selected to compute the electrochemical variables inside the CL of the 50-cm^2 reactive area geometry fuel cell in this work. The 50-cm^2 model geometry is used with LBAM to study the local transport losses, partial flooding, electrochemical kinetics, and the effect of humidity on local cell performance.

5.3 50-CM^2 REACTIVE AREA GEOMETRY WITH THREE STUDY LOCATIONS

Figure 5.3 shows the polarization curve of a single cell under the same cell operating conditions as before with both kinetic models and their respective simulation approaches. The numerical predictions at 8 points were chosen to cover the entire range of current densities (i.e., 0.05, 0.1, 0.2, 0.4, 0.6, 0.8, 1, and 1.2 A/cm^2). The co-current flow direction was chosen for both the experiment and simulation setup. The overall predictions from the two models look similar at low current density (open circuit voltage (OCV) to 0.4 A/cm^2). Both models present good agreement with experimental data. However, at high current densities starting from 0.6 A/cm^2, LBAM fits experimental data better than the macro-kinetics model. This is because the overpotential prediction of the LBAM is higher than macro-kinetics model due to the low partial pressure of O_2 gas and the high amount of water production. The LBAM can predict local liquid water evaporation/condensation within the detailed structure of the sample. However, the macro-kinetics model uses the entire prediction in the homogeneous CL. So, LBAM is a highly effective method of predicting the O_2 composition and partial flooding that affects the overall cell performance in the PEMFC.

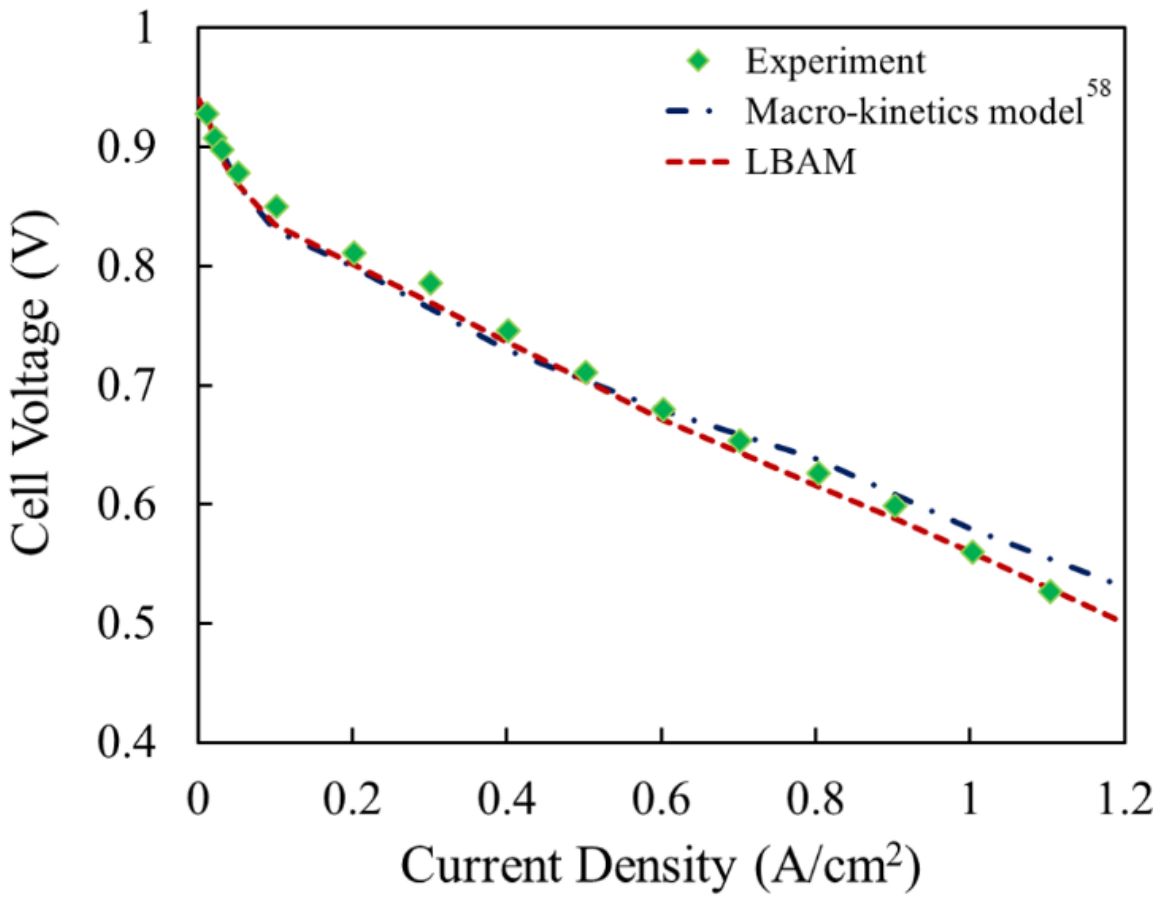

Figure 5.3 Polarization curve comparison between experimental result, macro-kinetics model, and LBAM.

Figure 5.4 shows the distribution prediction of volumetric current density, liquid-water saturation, heat, and mass transport inside the samples (GDL, MPL, and CL) at Location 1. This location is located near the inlet of the cell where all reacting gases start to flow into the cell. The predictions of anode and cathode temperature distributions are shown in Figs. 5.4a and 5.4b, respectively. The surface boundary conditions of the temperature on both sides were obtained from the macro-scale model and it were used the data mapping approach to interchange the numerical data between two models. The temperature in the cathode side is slightly higher than the anode side because the electrochemical reaction occurs at the CL of the cathode side. The highest temperature is located at the CL and it decreases toward the MPL to the bottom of GDL. This location has the average temperature of the anode and cathode sides about 336.60 K and 337.48 K, respectively. The surface temperature under the channel is higher than the land area, especially at the CL. This is because more reactant gases are consumed exothermically under the channel. Moreover, there is better heat transfer under the land area of the bipolar plate because of the higher thermal conductivity of the solid phase relative to the gas phase. The liquid water accumulation in the porous layers is observed as liquid water saturation in this location as presented in Fig. 5.4c. It is incurred by the chemical reaction and local condensation. There is small amount of liquid water accumulation at the center of the sample, where it is located under the rib area. The liquid water is then transported from the CL to the channel through the MPL and GDL. The highest liquid water saturation is located at the MPL region and it decreases throughout the GDL toward the channel, also shown in Fig. 5.4c. The reactants, H_2 and O_2, are consumed by the electrochemical reaction in the CL where oxidation takes place at the anode and reduction takes place at the cathode.

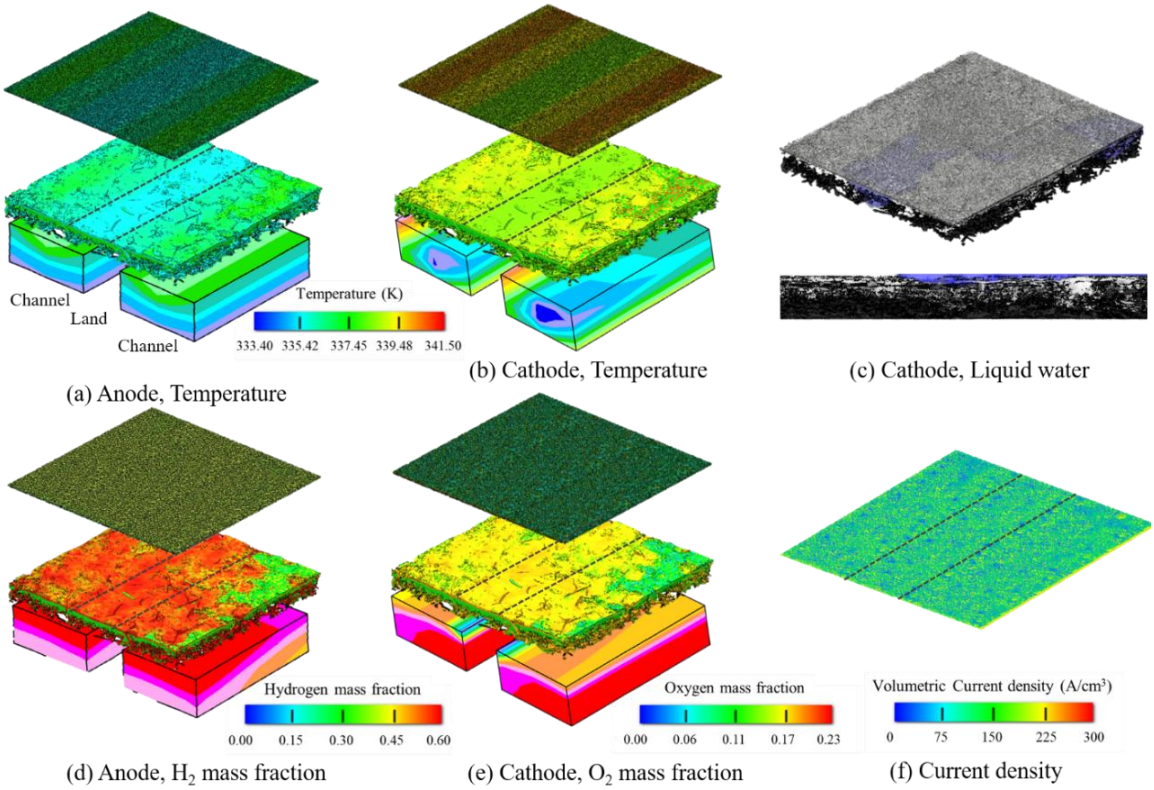

Figure 5.4 Prediction of volumetric current density, liquid water saturation, heat, and mass transport in the anode and cathode at Location 1 under an average current density of 1 A/cm^2 and 0.585 V. a) Anode temperature in the channels (macro-scale model) and GDL/MPL/CL, b) Cathode temperature in the channels (macro-scale model) and GDL/MPL/CL, c) Liquid water in the GDL/MPL/CL, d) Anode hydrogen mass fraction in the channels (macro-scale model) and GDL/MPL/CL, e) Cathode oxygen mass fraction in the channels (macro-scale model) and GDL/MPL/CL, and f) Current density on MEA surface.

The species transport at the anode and cathode, characterized by the H_2 and O_2 mass fractions, were predicted and are presented in Figs. 5.4d and 5.4e, respectively. Both species mass fractions decrease from the channel to the top of GDL and are consumed at the CL by the electrochemical reaction. At Location 1, there is a slight mass fraction distribution gradient due to the location near the inlet where there is a still enough reactants gas. The prediction of volumetric current density is shown in Fig. 5.4f. The average current density at this location is maintained at 1 A/cm^2 with the local potential of 0.585 V. The result shows the uniform distribution of current density with the anode and cathode overpotential of 0.013 V and 0.237 V, respectively.

Figure 5.5 shows the distribution of species mass fraction, temperature, liquid water saturation, and current density at Location 2. This location is located in the middle of the model geometry where the reactants gases still consume and have more liquid water accumulated. The predictions show a similar distribution of heat and mass transport when compared with the previous location. The average temperatures in this location for both sides are slightly higher than in Location 1, as shown in Figs. 5.5a and 5.5b. The average temperature of the anode and cathode sides are about 336.88 K and 338.08 K, respectively. However, the temperature distribution in this location is also the same as in the previous location, which has a higher temperature under the channel area than under the land area. Although the temperature is higher than at the previous location, the amount of liquid water saturation is nevertheless slightly increased, as shown in Fig. 5.5c. This shows that the temperature has a mild influence on the local liquid water saturation. The predictions of species transport in the anode and cathode sides are shown in Figs. 5.5d and 5.5e, respectively.

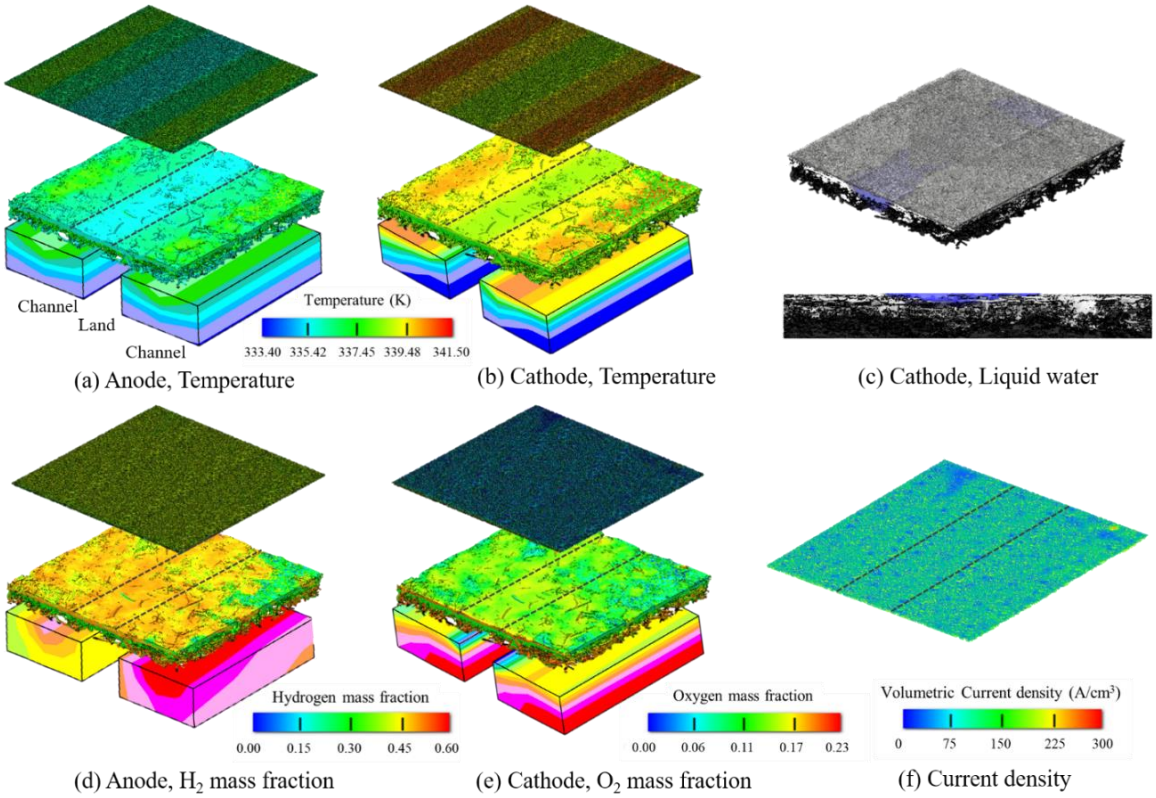

Figure 5.5 Prediction of volumetric current density, heat, and mass transport in the anode and cathode at Location 2 under an average current density of 1 A/cm^2 and 0.564 V. a) Anode temperature in the channels (macro-scale model) and GDL/MPL/CL, b) Cathode temperature in the channels (macro-scale model) and GDL/MPL/CL, c) Liquid water in the GDL/MPL/CL, d) Anode hydrogen mass fraction in the channels (macro-scale model) and GDL/MPL/CL, e) Cathode oxygen mass fraction in the channels (macro-scale model) and GDL/MPL/CL, and f) Current density on MEA surface.

The results show that the mass fractions of both species decrease with increasing distance from the inlet. There is a high mass fraction gradient for H_2 and O_2 from the channel to the CL. This shows the effect of diffusion on the transport of a species due to a mass fraction gradient in the porous layers. The consumption of both species during the HOR and ORR results in reactant depletion at the CL agglomerate boundary. In this location, the electrochemical variables were predicted under the same operating condition with the average current density of 1.0 A/cm^2, as shown in Fig. 5.5f. This location has the local potential of 0.564 V with the anode and cathode overpotential of 0.015 V and 0.260 V, respectively. This shows the voltage drop due to the loss of mass transport when compared with the previous location.

Figure 5.6 presents the model prediction of Location 3. This location is of interest because it lies in the outlet region of the cell where partial flooding may occur. The distribution of mass fractions, temperature, and current density behave similarly to the other locations, but this location has higher gradients of temperature and species mass fraction than the previous locations. This location has average temperatures at the anode and cathode of 337.50 K and 338.93 K, respectively, as shown in Figs. 5.6a and 5.6b. Figure 5.6c shows the liquid water saturation in the cathode side at Location 3. It was observed that high liquid saturation occurs in the middle of the cell where the land area is located. At the cathode, the liquid saturation is higher than the other locations mentioned above. This is because the vapor is saturated, leading to condensation in the flow-field. The liquid water saturation also comes from the electrochemical reaction that occurs at the cathode. The reacting gases were consumed by the electrochemical reaction to induce current and produce water and heat.

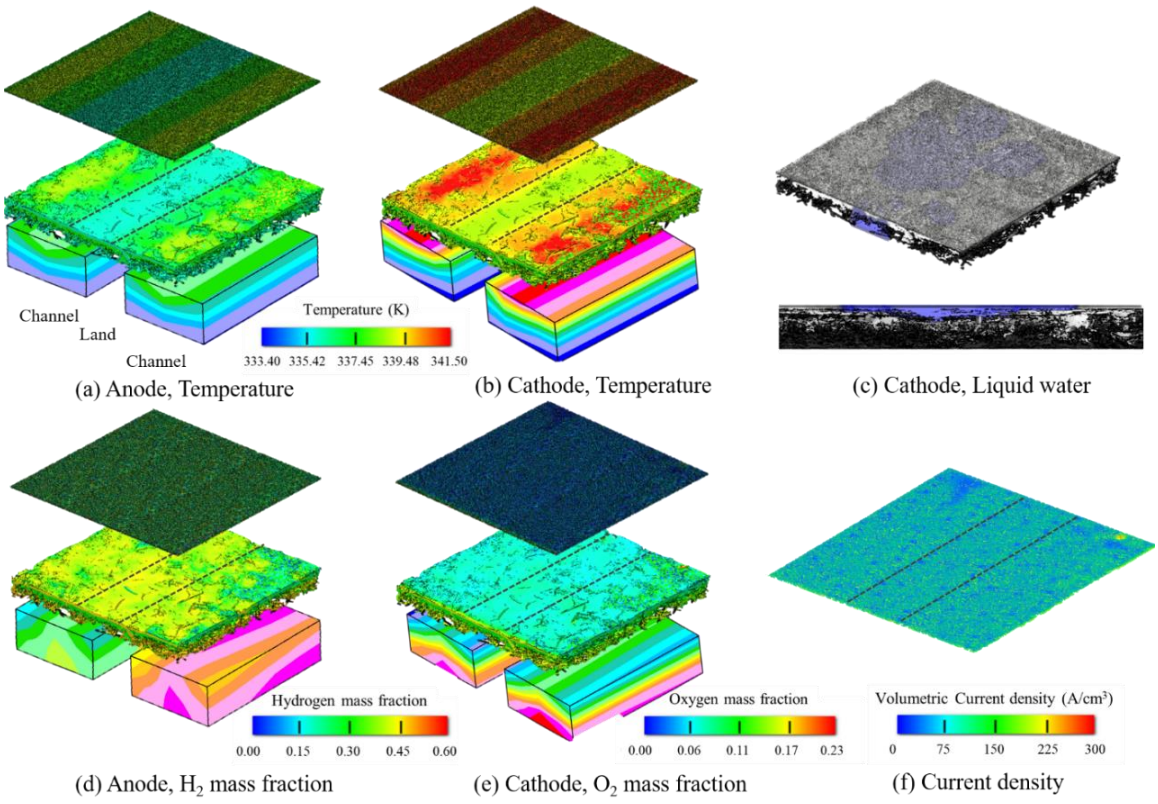

Figure 5.6 Prediction of volumetric current density, heat, and mass transport in the anode and cathode at Location 3 under an average current density of 1 A/cm^2 and 0.532 V. a) Anode temperature in the channels (macro-scale model) and GDL/MPL/CL, b) Cathode temperature in the channels (macro-scale model) and GDL/MPL/CL, c) Liquid water in the GDL/MPL/CL, d) Anode hydrogen mass fraction in the channels (macro-scale model) and GDL/MPL/CL, e) Cathode oxygen mass fraction in the channels (macro-scale model) and GDL/MPL/CL, and f) Current density on MEA surface.

This location shows high H_2 and O_2 gradients, as shown in Figs. 5.6d and 5.6e, respectively. Interestingly, on the cathode side, the result shows a low mass fraction of O_2 in the MPL and CL. This shows the low performance in the ORR due to partial flooding. Water accumulates inside the CL, inhibiting the flow of reactants to the catalyst surface and thereby increasing the activation overpotential via the blocking of reaction sites. On the anode side, no flooding occurs because liquid water is not produced from the reaction and just has a small amount of liquid water cross from the cathode side through the membrane. The average current density was maintained at 1 A/cm^2 just as it was in other locations. Figure 5.6f shows the volumetric current density distribution of location 3. This location has the anode and cathode overpotential of 0.023 V and 0.293 V, respectively. The prediction shows a uniform current density distribution with a local potential of 0.532 V. From the overall results, it shows the continuous decrease of the potential from the inlet to the outlet. The potential drop occurs when the current moves through the passive elements or transport resistance, which is predicted to overcome the reduction of the current. This corresponds to the reduction in reactants that are continuously consumed.

The overall predictions of the H_2 and O_2 mass fraction, cathode temperature, and cathode liquid water saturation profiles across the thickness or length of the samples are shown in Fig. 5.7. At the anode side, the prediction of H_2 mass fraction across the thickness of the sample (i.e., GDL, MPL, and CL) for locations 1 to 3 are shown in Fig. 5.7a. When the H_2 flows from the channel to the GDL, the H_2 diffuses in the GDL before moving into the MPL and getting consumed in the CL. The result shows that the H_2 mass fraction decreases crossing the interface from the GDL to the MPL. This shows the effect of the reduced pore size or porosity in the MPL that causes this step decrease at the interface.

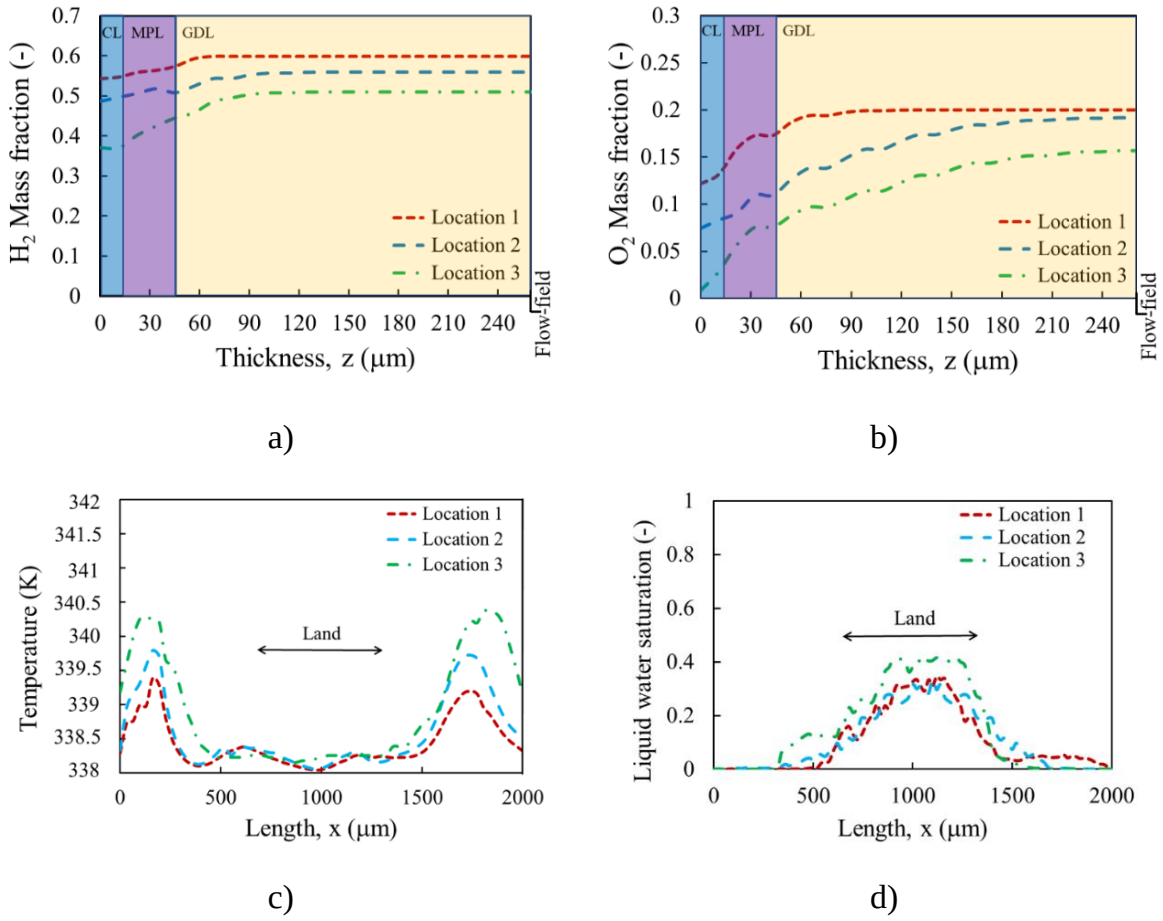

Figure 5.7 a) Hydrogen mass fraction profiles across the thickness (z-direction) of the sample, b) Oxygen mass fraction profiles across the thickness (z-direction) of the sample. c) Cathode temperature profiles across the length (x-direction) of the sample, and d) Cathode liquid saturation profiles across the length (x-direction) of the sample.

There is a high mass fraction at the location 1 (Inlet) and it is reduced toward the location 2 (Middle) and 3 (Outlet). At the interface between the CL and membrane (z = 0 μm), locations 1 to 3 have mass fractions of 0.55, 0.48, and 0.37, respectively. The percent consumption when compared to the non-reaction cases at these locations are 9%, 11%, and 25%, respectively. When comparing the H_2 profiles to the O_2 profiles, the results show that the H_2 has better diffusion than the O_2 because the H_2 mass fraction gradient is less than that of O_2, which can be attributed to the relatively high diffusivity of H_2. The O_2 mass fraction profiles across the thickness for all locations are shown in Fig. 5.7b. A low mass fraction of O_2 exists near the CL at the cathode due to the diffusion limitation. There may be local flooding that prevents the reactant diffusion to the catalyst sites at the cathode, which causes an additional voltage drop. The model agrees with known observations that transport to the cathode is the limiting factor of performance in PEMFCs. The prediction presents the mass fraction at the interface of the CL and membrane for locations 1 to 3 of 0.14, 0.08, and 0.03, respectively. The percentage of reactants consumed at these locations are about 32%, 58%, and 80%, respectively. At location 3, which was assigned to the outlet region, the simulation predicts a low mass fraction of O_2 at the CL. The O_2 mass fraction noticeably decreases from the bottom of GDL through the MPL due to the water production from the ORR. No limiting diffusion occurs at this location because the mass fraction of O_2 is sufficient for continued electrochemical consumption at this point. So, the transport of species at each location can be modeled for galvanostatic operation.

The through-plane cathode temperature profiles of these three locations are shown in Fig. 5.7c. The temperature under the channel is higher than under the land domain. This is because the land domain of the conductive bipolar plate allows heat to escape toward the

channel. It could also be that not as much heat is generated in the land domain because the reaction is favored in the channel domain, where reactants can easily flow from the channel to the CL. The average temperature is highest near the outlet and lowest near the inlet due to heat generation along the channel length. At the same average current density, higher heat generation should occur at a lower potential, and the results from the simulation agree. The temperature profiles of these three locations are similar in nature, but they differ due to the effect of the real structure compared with the macro-scale model from previous work (Shimpalee et al. 2019). The plots of liquid water saturation profiles are shown in Fig. 5.7d. This illustrates the liquid water saturation profiles along the length under difference three locations. The water production in the cathode depends upon the current density. In this study, the cell is operated at high current density (1 A/cm^2). So, more water was produced due to the water production from the ORR and the enhancement of proton conductivity. The prediction shows the average liquid water saturation of locations 1 to 3 are 0.09, 0.10, and 0.14, respectively. The overall results present that most of the liquid accumulation occurs at the center of the sample where the land is located. This is because of the low temperature in this region and low saturation pressure that makes the water vapor condense easily. There is low liquid water saturation under the channel because the high temperature in this area that makes the liquid water evaporate easily.

Figure 5.8 shows the model prediction of the O_2 mass fraction and liquid water saturation, in the difference computational models, multi-scale model and LBAM. The multi-scale model assumed the CL as a homogeneous porous continuum and LBAM used a detailed structure to represent the CL. The cathode side of location 3 is selected to investigate because this location is in the outlet region and has a partial flooding issue.

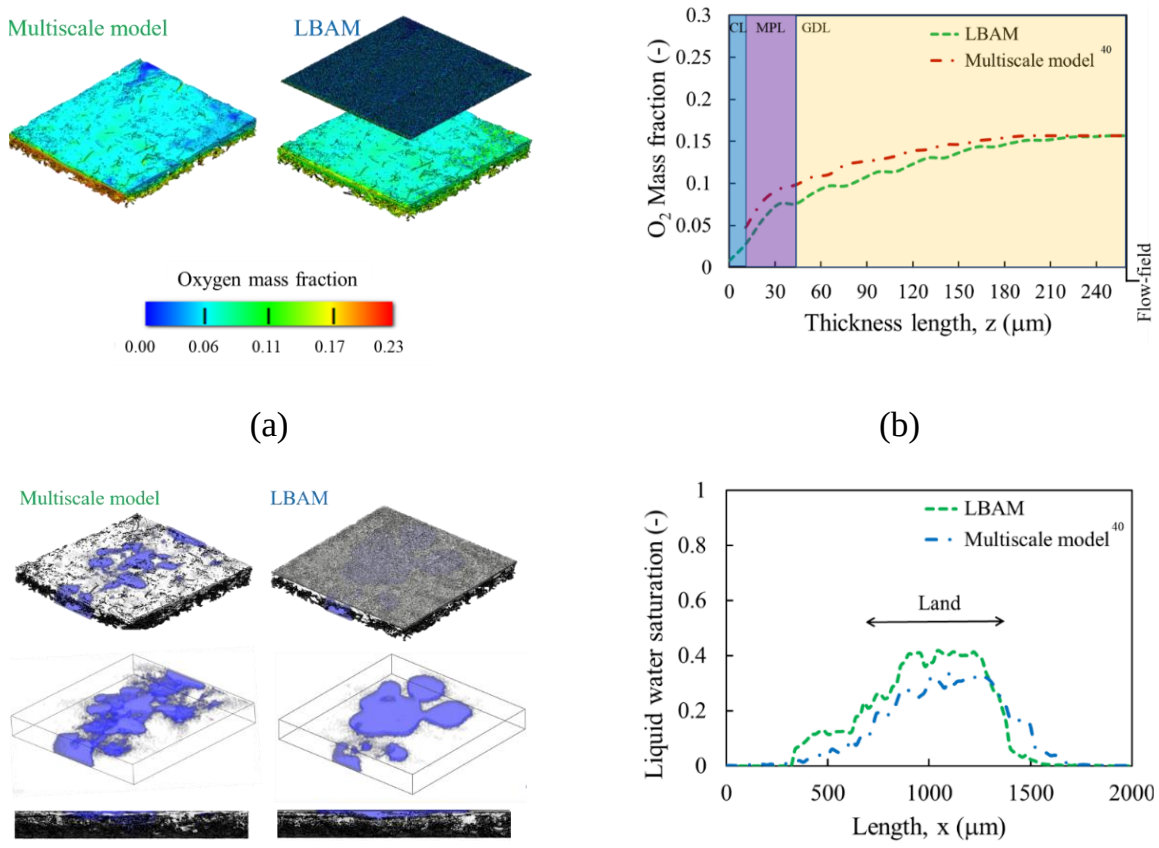

Figure 5.8 Model comparison between multi-scale model and LBAM at the cathode side of location 3. a) Oxygen mass fraction, b) Oxygen mass fraction profiles across the thickness (z-direction), c) Liquid water saturation, and d) Liquid saturation profiles across the length (x-direction).

Figure 5.8a presents the O_2 mass fraction in the difference models. The predictions show similar distribution of O_2 in the GDL and MPL. The multi-scale mode has a higher O_2 gradient than the LBAM. This can be confirmed by the through-plane O_2 mass fraction profiles, as shown in Fig. 5.8b. The multi-scale mode has a higher O_2 mass fraction along the thickness than the LBAM. The predictions show the mass fraction at the top of the CL surface ($z = 0$ μm) is around 0.010 when using the LBAM and is ($z = 10$ μm) about 0.050 for the multi-scale model. The percentages of O_2 consumption by LBAM and multi-scale model are approximately 80% and 63%, respectively. According to the previous publication (Shimpalee et al. 2019), which presents the polarization curve of the fuel cell using multi-scale model with homogeneous CL. The result shows a higher cell voltage than the experimental data at 1 A/cm^2. This is because the high O_2 mass fraction at the interface between the CL and MPL, which represent higher ORR and lower diffusion resistance than the LBAM. The liquid water saturation is another factor that affects the overall cell potential. The predictions show that the LBAM has a higher liquid water saturation than the multi-scale model, as shown in Figs. 5.8c and 5.8d. The prediction shows the average liquid water saturation by LBAM and multi-scale mode are about 0.14 and 0.12, respectively. The advantage of the LBAM is that one is able to observe the liquid water behavior in the CL. The multi-scale model shows that the liquid water has a non-uniform distribution, which is different from the LBAM. For the LBAM, it is observed that the liquid water generated from the CL flows through the MPL and GDL, then exits into the channel at the bottom of the GDL. This confirms that the computational domain with the detailed structure CL can more accurately predict cell performance.

5.4 SUMMARY

The Lattice Boltzmann Agglomeration Method (LBAM) has been used to study the electrochemical kinetics and mass transport inside the porous materials of PEMFCs. The predictions show that the local saturation of liquid water, kinetics, heat, and mass transport across the samples can be controlled by the regulation of operating conditions, especially under conditions that cause transport losses. This technique has been successfully demonstrated to predict the multi-physics/phase transport inside the porous media using the detailed structures from micro- and nano- X-ray computed tomography. This work also presents an advanced method for incorporating the lattice elements from LBM into an agglomerate structure. LBAM is a highly effective method of predicting local electrochemical variables and partial flooding within the detailed structures of porous layers and CLs. The homogeneous CL model is inherently limited because local transport within an agglomerate geometry is not considered. LBAM can predict and show distributions of electrochemical variables on the detailed structure of the CL, which is beneficial to the fuel cell design community. This method can expedite the development of porous components in PEMFCs in a cost-effective manner. The results from the LBAM simulation can assist the improvement of novel CL design, including catalyst structure, dispersion of precious and non-precious metal on the supports. The output of this work can be used to optimize not only the CL structure but also the operating conditions of a PEMFC.

CHAPTER 6

CONCLUSIONS AND RECOMMENDATIONS

6.1 CONCLUSIONS

Multi-scale modeling using direct modeling-based LBAM has been successfully demonstrated to explore the electrochemical kinetics and multi-scalar/multi-physics transport inside the porous and catalyst layers of PEMFCs using the detailed structures from micro- and nano- X-ray computed tomography. This shows the combination of two engineering disciplines, computed tomography and computational fluid dynamics. This work shows successful integration of the detailed structure from micro- and nano- X-ray computed tomography with LBM. The unique aspect of this work is to integrate the lattice elements into an agglomerate structure in the nano-scale geometry of the catalyst layer. Through this method, all transport variables from the micro-scale model can be transferred to the agglomerate structure, which is able to solve the kinetic expression and predict the electrochemical variables such as overpotential and current density in the catalyst layer. LBAM is an accurate method of predicting the partial flooding issue, understanding the transport resistance, and investigating transport inside the porous transport layer that affects the overall cell performance in the PEMFC.

With the aim of multi-scale modeling of multi-physics transport and distribution of electrochemical kinetics inside the porous and catalyst layers used in PEMFC. LBAM has been used to gain a better understanding of the behavior inside PEMFCs such as the transport of liquid water inside the GDLs. The predictions from LBAM show a good

agreement when compared and validated with the *ex-situ* (Satjaritanun et al. 2017) and *in-situ* flow visualization (Satjaritanun et al. 2018). The outcomes reveal that the liquid water saturation profiles inside the GDL and breakthrough pressures of the GDL are dependent on morphology of GDL, operating conditions, situations of cell assembly, and the flow-field plate design. This defines a problem for the design of fuel cell flow plates that can be handled with LBAM simulations. The predictions can be used to optimize the design of GDL structures and other related components, thereby improving the PEMFC's overall performance. After introducing the kinetic expressions into the model, LBAM can predict and show the distribution of electrochemical variables on the detailed catalyst layer. The predictions were compared with the experimental data and macro-kinetics model. LBAM presents better agreement with the experimental data than the macro-kinetics model, because it uses a detailed CL structure, while previous macro-kinetics models used a homogeneous CL structure. The LBAM can predict local water evaporation/condensation within the detailed structure of the sample. So, LBAM is a highly effective method of predicting the O_2 composition and partial flooding that affects the overall cell performance in the PEMFC.

Lastly, this work suggests enhancing the accuracy of the kinetics model by introducing the reaction mechanism at the surface of catalyst layer using the density functional theory (DFT) in the electrochemical kinetics model. Moreover, modeling scale-up is also of importance in order to gain an understanding of the effect of the flow channel and rib area at locations of interest inside the PEMFC. There are differences in transport mechanisms, specifically inside the GDL between the locations under the channel and the rib spacing. The multi-scale modeling approach shown in this work can enhance the

potential capability of a model-based investigation of mass and heat transports to determine designs and operational conditions in the PEMFC.

6.2 BROADER IMPACTS OF DISSERTATION

This dissertation shows the enhancement of direct modeling based LBAM, which incorporates the detailed structure of porous and catalyst layers from both micro- and nano-X-ray CT. LBAM consists of the kinetics model in the detailed structure of catalyst layer, which will involve coupling electrochemical kinetic to investigate the electrical potentials, electrical current, electron transfer, and exchange current density. This method can expedite the development of porous components in PEMFCs in a cost-effective manner, which is beneficial to the fuel cell design community. The LBAM simulation can assist the optimization of porous structure design and durability as well as improvement of water management, particularly in the catalyst layer. The LBAM shows ability to model other electrochemical systems as well, especially those with complex micro- or nano-structures such as other fuel cells, batteries, or electrolyzers.

REFERENCES

Ayers, K. E., Renner, J. N., Danilovic, N. J., Wang, X., Zhang, Y., Maric, R., and Yu, H. 2016. *Catalysis Today*. 262, 121-132.

Bazylak, A., Sinton, D., and Djilali, N. 2008. *Journal of Power Sources*. 176, 240-246.

Berg, P., Promislow, K. J., Pierre, St., Stumper, J., and Wetton, B. 2004. Journal of The Electrochemical Society. 151, A341-A353.

Bruno, M. M. and Viva, F. A. 2014. *in: H. R. Corti, and E.R. Gonzalez, Direct Alcohol Fuel Cell*. Amsterdam, Netherlands: Springer Netherlands.

Cetinbas, F. C., Advani, S. G., and Prasad, A. K. 2014. *Journal of Power Sources*. 250, 110-119.

Cetinbas, F. C., Ahluwalia, R. K., Shum, A. D., and Zenyuk, I. V. 2019. *Journal of The Electrochemical Society*. 166, F3001-F3008.

Chen, S. and Doolen, GD. 1998. *Annual Review of Fluid Mechanics*. 30, 329-364.

d'Humieres D. 2002. *Philosophical Transactions of the Royal Society of London. Series A: Mathematical, Physical and Engineering Sciences*. 360, 437-451.

Doube, M., Kłosowski, M. M., Arganda-Carreras, I., Cordelières, F. P., Dougherty, R. P., Jackson, J. S., Schmid, B., Hutchinson, J. R., and Shefelbine, S. J. 2010. *Bone*. 47, 1076-1079.

Eller, J., Roth J., Marone, F., Stampanoni, M., and Büchi, F. N. 2017. *Journal of The Electrochemical Society*, 164, F115-F126.

Epting, W., Lister, S. 2016. *Journal of Power Sources*. 306, 674-684.

García-Salaberri, P. A., Gostick, J. T., Hwang, G., Weber, A. Z., and Vera, M. 2015. *Journal of Power Sources*. 296, 440-453.

García-Salaberri, P. A., Hwang, G., Vera, M., Weber, A. Z., and Gostick, J. T. 2015. *International Journal of Heat and Mass Transfer*. 86, 319-333.

Gostick, J. T., Ioannidis, M. A., Fowler, M. W., and Pritzker, M. D. 2010. *in: CY. Wang, and U. Pasaogullari, Modeling and Diagnostics of Polymer Electrolyte Fuel Cells*. New York, NY: Springer New York.

Groso, A., Abela, R., and Stampanoni, M. 2006. *Optics Express*. 14, 8103-8110.

Hartnig, C., Menke, I., Kuhn, R., Kardjilov, N., Banhart, J., and Lehnert, W. 2008. *Applied Physics Letters*. 92, 134106-134109.

Harvey, D., Pharoah, J. G., and Karan, K. 2008. *Journal of Power Sources*. 179, 209-219.
Holman, D. M., Brionnaud, R., and Abiza, Z. 2012. *Proceeding in the European Congress on Computational Methods in Applied Sciences and Engineering (ECCOMAS)*. Vienna, Austria.

Holzer, L., Pecho, O., Schumacher, J., Marmet, Ph., Stenzel, O., Büchi, F. N., Lamibrac, A., and Munch, B. 2017. *Electrochimica Acta*. 227, 410-434.

Hong, BK., Mandal, P., Oh, JG., and Litster, S. 2016. *Journal of Power Sources*. 328, 280-288.

Ji, M. and Wei, Z. 2009. *Energies*. 2, 1057-1106.

Kandlikar, S. G. 2008. *Heat Transfer Engineering*. 29, 575-587.

Kandlikar, S. G., See, E. J., Koz, M., Gopalan, P., and Banerjee, R. 2014. *International Journal of Hydrogen Energy*. 39, 6620-6636.

Kumbur, C. and Mench, M. M. 2009. *Encyclopedia of Electrochemical Power Sources*. 828-847.

Liu, J., García-Salaberri, P. A., and Zenyuk, I. V. 2019. *Transport in Porous Media*. 128, 363-384.

Lu, Z., Daino, M. M., Rath, C., and Kandlikar, S. G. 2010. *International Journal of Hydrogen Energy*. 35, 4222-4233.

Manke, I., Hartnig, C., Grunerbel, M., Lehnert, W., Kardjilov, N., and Haibel, A., Banhart, J., and Riesemeier, H. 2007. *Applied Physics Letters*. 90, 174105-174107.

Manke, I., Hartnig, C., Kardjilov, N., Messerschmidt, N., Hilger, A., Strobl, M., Lehnert, W., and Banhart, J. 2008. *Applied Physics Letters*. 92, 244101-244103.

Moore, M., Wardlaw, P., Dobson, P., Boisvert, J. J., Putz, A., Spiteri, R. J., and Secanell, M. 2014. *Journal of The Electrochemical Society*. 161, E3125E-3137. Nam, J. H. and Kaviany, M. 2003. *International Journal of Heat and Mass Transfer*. 46, 4595-4611.

Nam, J. H., Lee, KJ., Hwang, GS., Kin, CJ., and Kaviany, M. 2009. *International Journal of Heat and Mass Transfer*. 52, 2779-2791.

Nguyen, TV., Ahosseini, A., Wang, X., Yarlagadda, V., Kwong, A., Weber, A. Z., Deevanhxay, P., Tsushima, S., and Hirai, S. 2015. *Journal of The Electrochemical Society*. 162, F1451-F1460.

Pasaogullari U. and Wang CY. 2004. *Journal of The Electrochemical Society*. 151, A399-A406.

Popov, B. N. 2015. *Corrosion Engineering 1st Edition*. Elsevier.

Premnath, K. and Banerjee, S. 2012. *Journal of Statistical Physics*. 143, 747-761.

Quesnel, C., Cao, R., Lehr, J., Kietzig, A-M., Weber, A. Z., and Gostick, J. T. 2015. *Journal of Physical Chemistry C*. 119, 22934-22944.

Raeini, A. Q., Bijeljic, B., and Blunt, M. J. 2015. *Advances in Water Resources*. 83, 102-110.

Raeini, A.Q., Blunt, M. J., and Bijeljic, B. 2014. *Advances in Water Resources*. 74, 116-126.

Santamaria, A. D., Das, P. K., MacDonald, J. C., and Weber, A. Z. 2014. *Journal of The Electrochemical Society*. 161, F1184-F1193.

Satjaritanun, P., Hirano, S., Shum, A. D., Zenyuk, I. V., Weber, A. Z., Weidner, J. W., and Shimpalee, S. 2018. *Journal of The Electrochemical Society*. 165, F1115-F1126.

Satjaritanun, P., Hirano, S., Zenyuk, I. V., Weidner, J. W., Tippayawong, N., Shimpalee, S. 2020. *Journal of The Electrochemical Society*. 167, 013516-013528.

Satjaritanun, P., Shimpalee, S., Weidner, J. W., Hirano, S., and Zenyuk, I. V. 2019. *ECS Transactions*. 92, 39-46.

Satjaritanun, P., Shimpalee, S., Weidner, J. W., Hirano, S., Lu, Z., Shum, A., Zenyuk, I. V., Ogawa, S., and Lister, S. 2017. *ECS Transactions*. 80, 187-195.

Satjaritanun, P., Weidner, J. W., Hirano, S., Lu, Z., Khunatorn, Y., Ogawa, S., Litster, S. E., Shum, A. D., Zenyuk, I. V., and Shimpalee, S. 2017. *Journal of The Electrochemical Society*. 164, E3359-E3371.

Schneider, C. A., Rasband, W. S., and Eliceiri, K. W. 2012. *Nat Meth*. 9, 671-675. Shan, X. and Chen, H. 2007. *International Journal of Modern Physics C*. 18, 635-643.

Shearing, P. R., Cai, Q., Golbert, J. I., Yufit, V., Adjiman, C. S., and Brandon, N. P. 2010. *Journal of Power Sources*. 195, 4804-4810.

Shearing, P. R., Gelb, J., and Brandon, N. P. 2010. *Journal of the European Ceramic Society*. 30, 1809-1814.

Shearing, P. R., Golbert, J., Chater, R. J., and Brandon, N. P. 2009. *Chemical Engineering Science*. 64, 3928-3933.

Shearing, P.R., Bradley, R. S., Gelb, J., Lee, S. N., Atkinson, A., Withers, P. J., and Brandon, N. P. 2011. *Electrochemical and Solid-State Letters*. 14, B117-120.

Shimpalee, S., Hirano, S., DeBolt, M., Lilavivat, V., Weidner, J. W., and Khunatorn, Y. 2017. *Journal of The Electrochemical Society*. 164, E3073-E3080.

Shimpalee, S., Lilavivat, V., Xu, H., Khunatorn, Y., and Mittlesteadt, C. K. 2016. *Electrochim. Acta*. 222, 1210-1219.

Shimpalee, S., Satjaritanun, P., Hirano, S., Tippayawong, N., and Weidner, J. W. 2019. *Journal of The Electrochemical Society*. 166, F534-F543.

Shimpalee, S., Satjaritanun, P., Weidner, J. W., Hirano, S., Lu, Z., Ogawa, S., and Litster, S. 2016. *230th Electrochemical Society Meeting*. Abstract # 2387, Honolulu, HI.

Shimpalee, S., Satjaritanun, P., Weidner, J. W., Hirano, S., Lu, Z., Shum, A., Zenyuk, I. V., Ogawa, S., and Litster, S. 2017. *232nd Electrochemical Society Meeting*. Abstract# MA2017-02 1418 National Harbor, Maryland (2017).

Shum, A. D., Parkinson, D. Y., Xiao, X., Weber, A. Z., Burheim, O S., and Zenyuk, I. V. 2017. *Electrochimica Acta*. 256, 279-290.

Steinbach, A. J., Allen, J. S., Borup, R. L., Hussey, D. S., Jacobson, D., Komlev, A., Kwong, A., MacDonald, J., Mukundan, R., Pejsa, M. J., Roos, M., Santamaria, A. D., Sieracki, J. M., Spernjak, D., Zenyuk, I. V., and Weber, A. Z. 2018. *Joule*. 2, 1297-1312.

Wang, CY. 2004. *Chemical Reviews*. 104, 4727.

Wang, Y. and Wang, CY. 2006. *Journal of The Electrochemical Society*. 153, A1193-1200.

Weber, A. Z. 2010. *Journal of Power Sources*. 195, 5292-5304.

Weber, A. Z. and Newman, J. 2006. *Journal of The Electrochemical Society*. 153, A2205-A2214. Weber, A. Z., Borup, R. L., Darling, M., Das, P. K., Dursch, T. J., Gu, W., Harvey, D., Kusoglu, A., Litster, S., Mench, M. M., Mukundan, R. J., Owejan, P., Pharoah, J. G., Secanell, M., and Zenyuk I. V. Zenyuk. 2014. *Journal of The Electrochemical Society*. 161, F1254-F1299.

Yablecki, J., Hinebaugh, J., and Bazylak, A. 2012. *Journal of The Electrochemical Society*. 159, F805-F809.

Yoon, W. and Weber, A. Z. 2011. *Journal of The Electrochemical Society*. 158, B1007-B1018.

Zaretskiy, Y., Geiger, S., Sorbie, K., and Förster, M. 2010. *Advances in Water Resources*. 33, 1508-1516.

Zenyuk, I. V., Das, P. K., and Weber, A. Z. 2016. *Journal of The Electrochemical Society*. 163, F691-F703.

Zenyuk, I. V., Lamibrac, A., Eller, J., Parkinson, D.Y., Marone, F., Büchi, F. N., and Weber, A. Z. 2016. *The Journal of Physical Chemistry C*. 120, 28701-28711.

Zenyuk, I. V., Parkinson, D. Y., Hwang, G., and Weber, A. Z. 2015. *Electrochemistry Communications*. 53, 24-28.

Zenyuk, I. V., Parkinson, D.Y., Connolly, L.G., and Weber, A. Z. 2016. *Journal of Power Sources*. 328, 364-376.

Zhang, D., Cai, Q., and Gu, S. 2018. *Electrochimica Acta*, 262, 282-296.

APPENDIX A

LIQUID WATER SATURATION PROFILE IN GDL WITH AND WITHOUT MPL

The appendix A presents the local saturation of liquid water under breakthrough dynamics across the GDLs with and without a MPL. The model geometries of GDLs and MPLs used in this study were obtained by 3D reconstructed micro-structure from Micro X-ray CT, as shown in Fig. A.1. The overall predictions of water breakthrough pressure agree with the data observed in the experiments. The main objective of this appendix is to understand the detailed water saturation during water break through the GDL with and without MPL (SGL 24BA and SGL 25BC). The effect of the wetting parameter also known as contact angle of liquid water on the solid structures is also taken into account. From 3D simulation, the liquid water evolution during the water breakthrough process are reported and discussed.

Figure A.2 shows the prediction of liquid water saturation profiles from LBM with different wettability of GDL structure SGL 24BA. These graphs show liquid water saturation profiles versus dimensionless time (tD) for different wettability of the GDL structure. This liquid water saturation profile was numerically measured by volume of liquid water at several locations between where the liquid water is fed into the outlet.

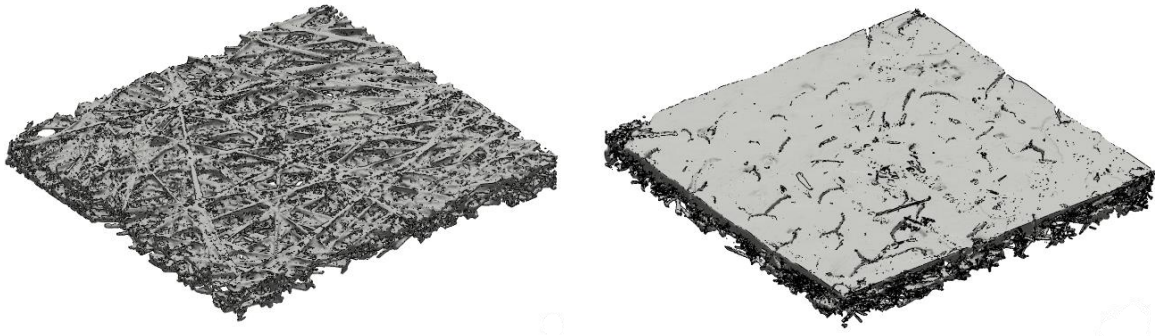

a) b)

Figure A.1 3D rendered image from Micro Computed Tomography. a) 3D rendered image of SGL 24BA, b) 3D rendered image of SGL 25BC.

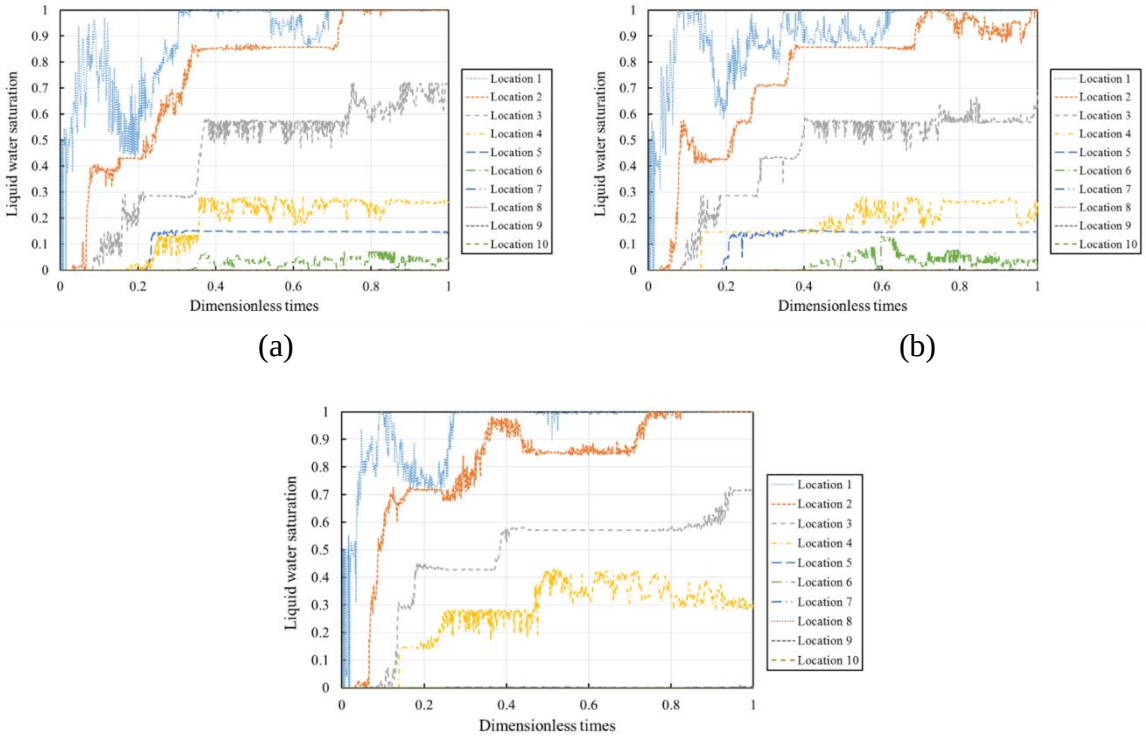

(a) (b)

(c)

Figure A.2 Liquid water saturation profiles with time at each section of GDL thickness for SGL 24BA. a) Liquid water saturation profiles for contact angle of 40°, b) Liquid water saturation profiles for contact angle of 90°, c) Liquid water saturation profiles for contact angle of 140°.

So, the liquid water saturation profile is the volume of liquid water occupying each location when the liquid water has passed through the GDL. In this work, dimensionless times is defined as the ratio of local time to the time approaching steady state.

For the case of high contact angle or non-wetting of the GDL structure gives the lowest liquid saturation profile. The liquid water saturation increases as the GDL structure changes to a more wetting material. Furthermore, the results show the relationship of breakthrough pressure and liquid water saturation. When the breakthrough pressure is increased, the liquid water saturation profile decreases. Thus, for the cases of contact angle of 90° shows slightly lower liquid water saturation profile than contact angle of 40°. The average liquid saturation when the liquid water pass through the GDL are given in Figure A.3.

Figure A.3 shows the prediction of average liquid saturation (left y-axis) and pressure (right y-axis) against dimensionless time for three different wettability of the GDL structure. The high hydrophilicity case (40° contact angle) or wetting of the GDL structure shows the highest average liquid saturation. Because the liquid water is moving through the GDL faster than the others (90° and 140° contact angle). This corresponds to the results of Satjaritanun et al. (2017), which showed the higher breakthrough pressure for the high hydrophobicity or non-wetting of the GDL structure which needs more energy to push the water through the GDL. So, for the non-wetting GDL structure it is difficult for water to pass through. The average liquid saturation increases as the GDL structure change to more wetting material. However, the case of 90° contact angle shows slightly higher average liquid saturation than contact angle of 140°.

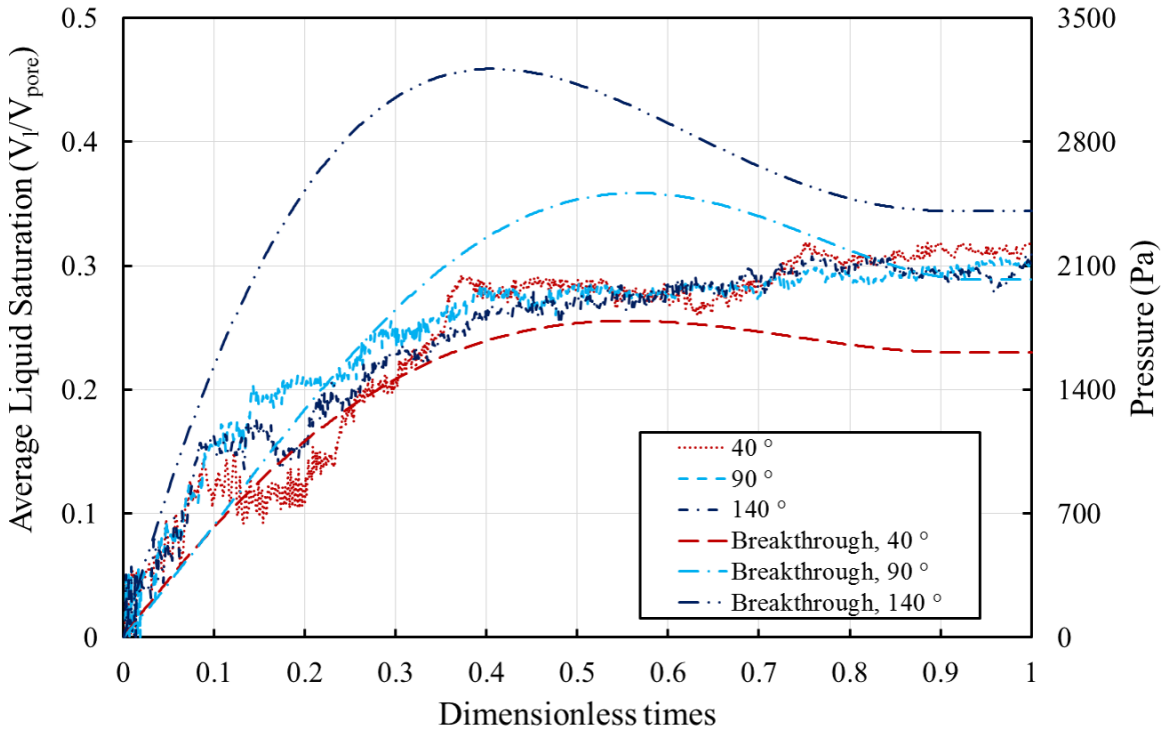

Figure A.3 The effect of contact angle (wettability) on average liquid saturation of SGL24BA.

The next simulation was computed using the different GDL sample with micro porous layer (i.e., SGL 25BC). In order to predict liquid water saturation profile of GDL with MPL. The structure of MPL needs to be included into the model. In this work, we can manually split the 3D rendering of SGL 25BC geometry into 2 solid part, GDL and MPL as shown in Figure A.4. According to the approach of our previous paper (Satjaritanun et al. 2017), the solid structured MPL was replaced by porous model and its properties were taken from the measurement in 3D reconstructed micro-structure of MPL of SGL 25BC from Nano X-ray CT as shown in Fig. 10a of Ref. (Satjaritanun et al. 2017). So, the porosity of the MPL is 52% and the permeability is around 1.0×10^{-15} m^2 for all directions.

The microstructure of SGL 25BC from Micro X-Ray CT geometry was used in the simulation. The liquid water saturation profile prediction was performed. In our previous work, Satjaritanun et al. (2017) reported the pressure profiles during water evolution starting from MPL to GDL. The simulation breakthrough pressure of SGL 25BC are 4,500, 6,000, and 7,800 Pa for contact angle of 40°, 90°, and 140°, respectively. The simulation breakthrough pressures are close to the value observed in the experiment.

Figure A.5 shows the prediction of liquid water saturation profiles with different wettability of the GDL and MPL structures for SGL 25BC. When the liquid water is pushed from MPL to GDL, liquid water spreads all over the MPL surface before moving toward the GDL because it is more difficult for liquid water to move through the MPL. So, the liquid water fully spreads out on top of the MPL and then gradually flows through the GDL. Because of this more gradual flow the overall profiles are different from the predictions of the GDL without MPL with the slower transport resulting in less noise in the saturation profiles than the predictions of GDL only.

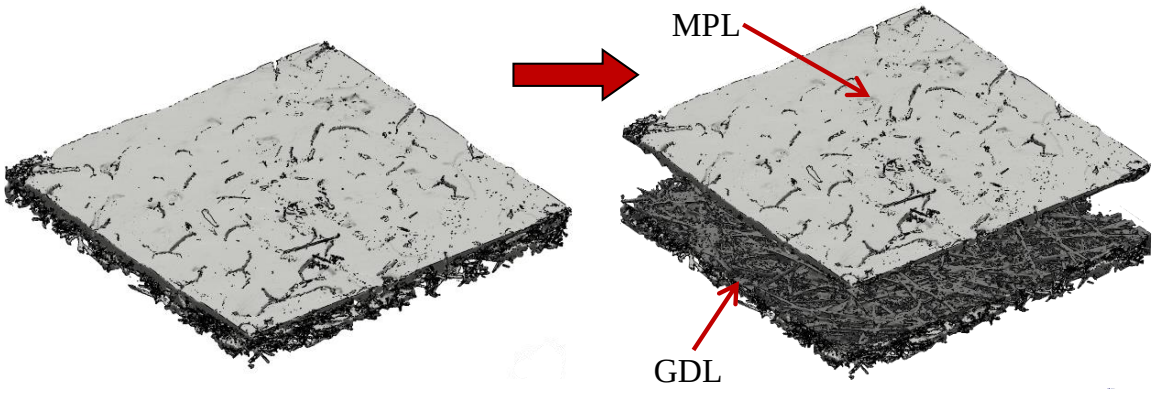

Figure A.4 The reconstructed micro-structure of GDL and MPL from micro X-Ray CT.

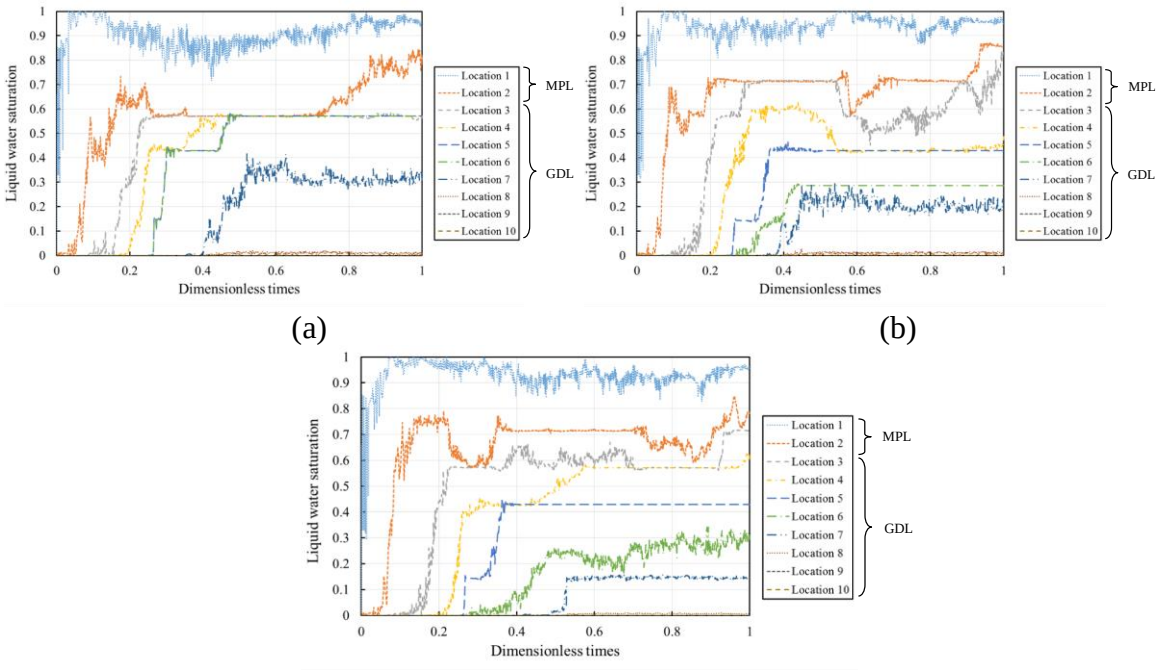

Figure A.5 Liquid water saturation profiles with time at each section of MPL to GDL thickness for SGL 25BC. a) Liquid water saturation profiles for contact angle of 40°, b) Liquid water saturation profiles for contact angle of 90°, c) Liquid water saturation profiles for contact angle of 140°.

Figure A.6 presents the average liquid saturation profiles during the movement of liquid water when it was pushed from MPL to GDL. The increase in average liquid saturation profiles with dimensionless time for 40°, 90°, and 140° contact angle values are similar as liquid water was pass through the MPL before it moves to the GDL then slightly reach to steady after tD = 0.5. Because the required pressure to push the liquid water completely through the MPL. After that, the liquid water pass through and occupy all pore networks in the GDL/MPL, the capillary pressure will no longer hold thus, reducing to static liquid water pressure.

In conclusion, three-dimensional numerical simulation using the Lattice Boltzmann Method has been used to study the water transport inside the porous material in polymer electrolyte membrane fuel cells. The local saturation of liquid water under breakthrough dynamics across the GDLs and the average liquid saturation inside the GDL samples are different with the changes of the wetting properties of the GDL. Because the pore space shape and size in porous material used in PEMFC are variable and irregular. The LBM technique can successfully simulate the two-phase transport inside the porous media using the geometries from X-ray CT depending on the purpose of the research.

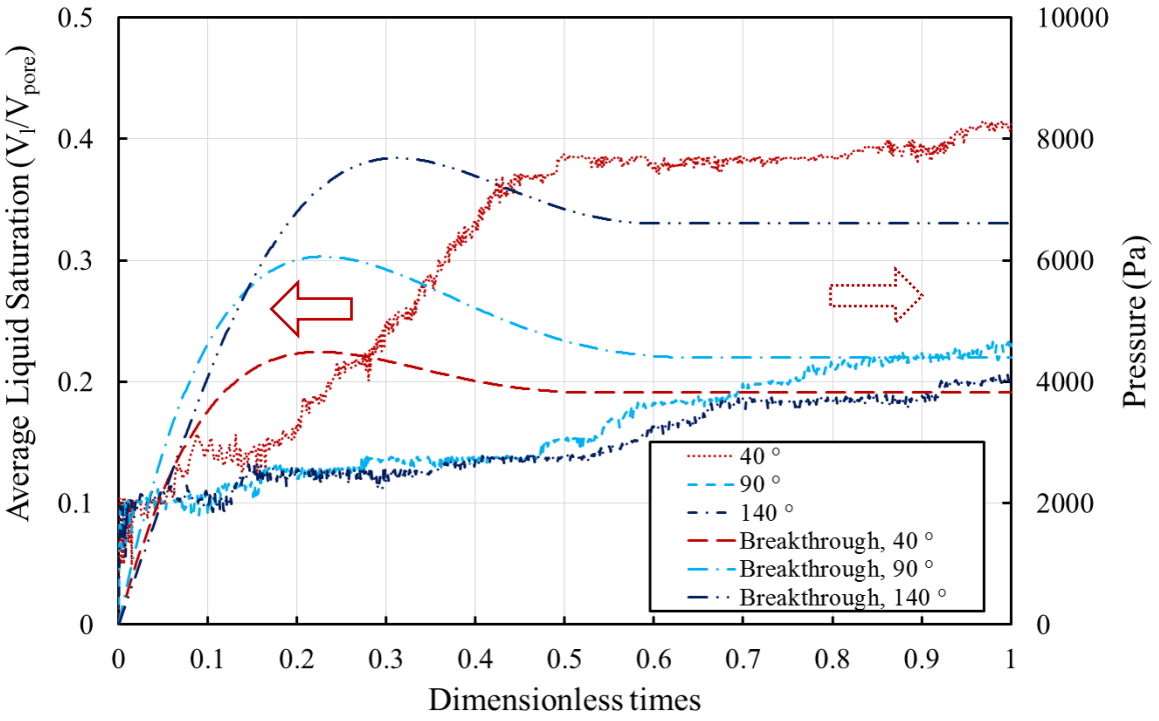

Figure A.6 The effect of contact angle (wettability) on average liquid saturation for SGL 25BC.